

TEL - AVIV UNIVERSITY
THE IBY AND ALDAR FLEISCHMAN FACULTY OF
ENGINEERING
Department of Physical Electronics

Subject

MICROWAVE EXCITED CO₂ LASERS

Thesis submitted towards the degree of
“Doctor of Philosophy”

by
Avi Shahadi

March 2001

TEL - AVIV UNIVERSITY
THE IBY AND ALDAR FLEISCHMAN FACULTY OF ENGINEERING
Department of Physical Electronics

Subject

MICROWAVE EXCITED CO₂ LASERS

Thesis submitted towards the degree of
“Doctor of Philosophy”

by
Avi Shahadi

Under the supervision of
Prof. Eli Jerby

Advisor: Dr. Yoav Sintov

March 2001

CONTENTS

Abstract	5
Acknowledgments	9
List of Symbols	10
1. Introduction	14
1.1. Laser Classification	15
1.2. The CO ₂ Laser	18
1.2.1. CO ₂ Laser Excitation Methods	20
1.2.2. Energy-Transitions Kinetics in CO ₂ Lasers	22
1.2.3. CO ₂ Slab-Lasers	26
1.2.3.1. Heat Flow Considerations	27
2. The Electrical Discharge in Slab Lasers	31
2.1. Gas Discharge Processes	31
2.2. RF and Microwave Discharges	34
2.2.1. Two Modes of Stable Discharges in an RF-Excited Slab Laser	36
2.2.1.1. The α Discharge	36
2.2.1.2. The γ Discharge	39
2.2.2. RF vs. Microwave Discharges	41
3. Thermal-Instability Considerations for Pulsed Microwave-Excited CO ₂ Slab-Lasers	45
3.1. Discharge Instability Characterization	44
3.2. Thermal Instabilities	46
3.2.1. Discharge Model	48
3.2.2. Evolvement of Thermal Instabilities	53
3.2.2.1. Effective Gap Thickness for Heat Flow in the Presence of a Dielectric Strip	54
3.2.3. Free Evolution of Thermal Instabilities	57
3.2.4. Evolution of Thermal Instabilities in the Presence of a Ballast Dielectric-Strip	60
3.2.5. Thermally Optimized Microwave Discharge	65

4. Microwave-Excited Lasers	67
4.1. The Cylindrical Parallel-Plate CO ₂ Laser (Scheme #1)	68
4.1.1. Experimental Setup	69
4.1.2. Microwave Design Considerations	72
4.1.3. Experimental Results (Scheme #1)	75
4.1.4. Discussion	78
4.2. The CO ₂ Slab-Laser (Scheme #2)	79
4.2.1. Experimental Setup	80
4.2.2. Microwave Setup and Design	83
4.2.3. Experimental Measurement Setup	85
4.2.4. Experimental Results (Scheme #2)	86
4.2.4.1. Longitudinal Discharge Homogeneity	86
4.2.4.2. A 2.0 mm Discharge-Width Laser	88
4.2.4.3. A 1.5 mm Discharge-Width Laser	99
4.2.4.4. Laser Output-Pulse Measurements	109
4.2.4.5. Small-Signal Gain Measurements	112
4.2.4.6. Output (Laser) Coupler Optimization	114
4.2.4.7. Beam Quality Measurements	116
4.2.5. Sealed CO ₂ Slab-Laser	117
4.2.5.1 Experimental Results	118
5. Analysis	119
5.1. Transient Temporal and Longitudinal Amplitude-Buildup	120
5.2. Slab-Laser Thermal Investigation	129
5.3. Slab-Laser Efficiency Assessment	138
6. Conclusion	142
Appendices	
A The Magnetron to Laser Head Coupling	145
B High Voltage Switching	148
C Rectangular Pyrex Tubes for Gas Confinement	151
References	156

Abstract

A slab laser-head configuration, as shown by Yatsiv and others, has been proved to be most suitable for RF or microwave excitation of slow-flow and sealed CO₂-lasers. This laser scheme is characterized by its high average and peak powers. When combined with microwave excitation these lasers dominate with respect to high peak-to-average power ratios, for pulsed regimes of tens of microsecond pulse-widths, and above 1 kHz pulse repetition-frequencies. In this regime the microwave-excited CO₂ slab-laser proves advantageous compared to RF excited lasers or to RF and DC combined schemes.

Two main mechanisms impairing the CO₂ slab-lasers operation, by limiting their efficiency and mode of operation, are investigated, namely:

- Thermal-instabilities development due to the relatively high-frequency excitation.
- A longitudinally inhomogeneous discharge electric-field resulting from a relatively short excitation-wavelength.

The research presents adequate solutions for improving the operation of CO₂ slab-lasers, regarding thermal-instabilities and the longitudinal homogeneity of the microwave-discharge. These solutions are supported by theory and by experimental verifications. The research is concluded by presenting preliminary results for a sealed microwave-excited CO₂ laser. It is based on the investigated designs, and retaining their advantageous features.

In this research, we investigate the microwave excitation of a CO₂ laser in two devices designed and constructed according to the requirements of (a) a magnetron as an energy source; (b) a longitudinally homogeneous microwave-discharge; and (c) a simple and compact design.

The first laser setup developed in this research is a cylindrical parallel-plate scheme yielding an average power of ~ 2 W together with a 40 W of peak laser-power. A longitudinally homogeneous microwave-discharge is observed, as explained by an analytical model. However, this device is characterized by a low efficiency of ~ 1 %. It results from the magnetron and plasma loaded microwave-resonator impedances mismatch. The parallel-plate CO₂ laser proves compact and extremely simple to construct. It serves for the investigation of the microwave power matching of the magnetron to the laser-head plasma, and for the monitoring of discharge

thermal-instabilities. It enables a study of the influence of the gas mixture, the gas pressure and flow rate, the pulsed microwave power and the duty cycle on the laser operation.

In a second device, we consider the limitations of the first scheme regarding the microwave power matching, together with mathematical analyses of a microwave-excited CO₂ slab-laser configuration. Two of the main microwave discharge disadvantages, namely, the (microwave-discharge) thermal instability and the microwave-discharge longitudinal non-uniformity are studied using analytical models for this laser. A thermal instability analysis for pulsed microwave excited CO₂ slab-lasers is performed. This analytical model optimizes the thickness of a ballast dielectric-strip inserted into the microwave-discharge zone regarding the formation of thermal instabilities. Hence, the heat flow from the discharge zone to the laser-head enclosing walls is optimized for a chosen pulse duty-cycle.

A second mathematical model is developed for demonstrating a longitudinally homogeneous microwave discharge in a CO₂ slab-laser. This model considers the plasma loading of a microwave resonator and accounts for the critical microwave coupling to the laser head, with and without the presence of the laser plasma. A 3D numerical software (Ansoft HFSS) is used to simulate the exact design of the slab laser considering ten degrees of freedom for the microwave matching. The results of the numerical model coincide with these of the analytical one. These results are verified experimentally by assessing the laser longitudinal microwave-power distribution, and the discharge longitudinal-luminescence.

The microwave design accounts for (a) a proper operation regime of the magnetron (resulting in a high magnetron-efficiency), and; (b) the formation of a longitudinally homogeneous microwave-discharge.

Two microwave resonators are attached in H-plane, where one resonator is axially shorter than the other one. The prime resonator serves for energy storage and the other serves as the laser head. Hence, a longitudinally homogeneous microwave-discharge is obtained. The constant cross-section of the laser head microwave-resonator leads to a simple design. Two discharge widths (2.0 and 1.5 mm) are analyzed, and a parametric investigation of the average and peak laser powers is carried out. The dependence of the laser parameters on the input microwave power and the gas pressure and flow-rate is examined. The efficiency of the different stages of the laser, namely DC to microwave, microwave to plasma, and plasma to laser

power, is assessed. A small-signal gain measurement, together with a beam-quality estimation, is performed for the two discharge widths.

A slab laser-head is matched to a 2 kW, 2.45 GHz low-cost oven magnetron by a rectangular waveguide. This slow gas-flow laser is operated optimally at a pressure of ~ 50 Torr, and generates a maximal peak laser-power of ~ 575 W with an overall efficiency of 6 % in a duty cycle of 2 %. The maximal average-laser-power is ~ 40 W, with a plasma to laser power efficiency of ~ 11 % in a duty cycle of 6 %. For this laser, the maximal overall efficiency is 9 % in a duty cycle of 5 %, corresponding to 22 % plasma-to-laser power efficiency.

A sealed laser structure based on the investigated CO₂ slab-laser design yields an average laser power of 13 W, which corresponds to a peak laser power of 210 W, with a microwave to laser-power efficiency of 4 %. A 5 % decrease in the peak laser power is observed after a two-hour operation.

The CO₂ slab-laser designed and constructed in this thesis presents solutions for two of the main difficulties of microwave excitation of slab lasers, namely, thermal instabilities, and the discharge longitudinal-homogeneity. An analytical procedure for determining the optimum thickness of the dielectric ballast-strip inserted into the microwave discharge zone is presented. By finding the thinnest dielectric strip required for sustaining a thermally stable discharge, the rate of heat removal from the discharge zone can be increased. Therefore, increased laser efficiency is possible. The proposed distributed microwave coupling of a magnetron to a laser head with a uniform cross-section forms a longitudinally homogeneous microwave-discharge. This feature can coincide with a proper setting of the magnetron operation regime regarding its power extraction capabilities. The laser head uniform cross-section allows the use of a standard rectangular Pyrex tube as the gas confinement chamber.

This versatile compact and simple design is optimized regarding microwave matching and heat removal considerations. It leads to the construction of a highly efficient device. It enables a high average and peak laser powers, and high peak to average laser power-ratios. Preliminary results show the feasibility of sealed operating. These features may prove favorable compared with other CO₂ lasers using similar parameters. The present microwave-excited CO₂ slab-laser proves practical in a growing and diverse field of applications.

This thesis is dedicated to my parents
Sara and Nathan Shahadi

Acknowledgments

The research presented would not have been possible without the scientific foundation laid down by Prof. Shaul Yatsiv to the world of CO₂ slab-lasers. We benefited immensely from his vast knowledge and creative council.

I would like to express my gratitude towards my supervisor Prof. Eli Jerby who encouraged and supported my pursuit of the chosen scientific-line of research presented in this thesis. His methodical, as well as intuitive knowledge, leading to simple yet extremely practical scientific solutions is admired. Having the opportunity to observe a true researcher aiming at overcoming scientific challenges by devoted work is appreciated.

I would like to thank Dr. Yoav Sintov who introduced me to the world of gas lasers, and helped me to achieve the goals of this research. His mastery of the world of laser physics, in both scientific and practical aspects, is a source of inspiration.

List of Symbols

Symbol	Description	Unit
α, γ	Stable modes of a glow discharge	
α_T	Plasma longitudinal attenuation	Neper/cm
α_w	Optical waveguide loss	Neper/cm
α_{OT}	Round-trip optical volume loss	Neper/cm
β	Recombination rate coefficient	cm ³ /s
β_e	Electron-ion recombination rate coefficient	cm ³ /s
β_{e3}	Three-body recombination rate coefficient	cm ³ /s
β_i	Ion-ion recombination rate coefficient	cm ³ /s
ϵ_p	Plasma relative dielectric-constant	
ϵ_r	Dielectric-slab relative dielectric constant	
ϵ_d	Dielectric-slab relative complex dielectric constant	
γ_0	Small signal gain (s.s.g)	%/cm
Γ_d	Diffraction losses	%
η	Squared ratio of the plasma and dielectric slab absolute voltages	
κ	Gas heat conductivity	W/cm ² K
κ_b	Dielectric slab heat conductivity	W/cm ² K
λ, λ_c	Signal wavelength, and a resonator cutoff-wavelength	cm
Λ	Effective discharge width	cm
μ_e	Electron mobility	cm ² /Vs
μ_w	Plasma power loss	m ⁻¹
ν_c	Effective collision frequency	s ⁻¹
ν_{1-3}	CO ₂ vibration type	
ν_{hf}	Discharge heat-removal-rate to the walls	s ⁻¹
ν_t^0	The ratio between the gas heating-rate and stored energy	s ⁻¹
$\hat{\nu}_t$	The change in the normalized electron density variation	

Symbol	Description	Unit
θ	Laser beam divergence	rad
σ	Plasma conductivity	$1/\Omega \text{ cm}$
τ	Thermal-instability characteristic evolution time	s
ω	Excitation angular frequency	rad/s
ω_c	Collision angular frequency	rad/s
ω_p	Plasma angular frequency	rad/s
Ω	Thermal-instability perturbation growth-rate	s^{-1}
Ω_m	Mean instability growth rate	s^{-1}
a, a_1	Rectangular and double-ridge waveguides' widths	cm
a_2	Double-ridge waveguide, ridge width	cm
b, b_1	Rectangular and double-ridge waveguides heights	cm
b_2	Double-ridge waveguide, ridges spacing	cm
C_d	Dielectric slab capacitance	F/cm^2
$\bar{C}_{d/p}$	Ratio of the optimal dielectric-slab and plasma capacitances	
C_p	Gas specific heat	$\frac{\text{Joule}}{\text{cm}^3 \text{ K}}$
C_{pl}	Plasma capacitance	F/cm^2
C_s	Space-charge layers equivalent capacitance	F/cm^2
d	Slab geometry spacing	cm
d_0	Space-charge layer amplitude	cm
$d_{1,2}$	Space-charge layer thickness	cm
d_b	Dielectric slab thickness	cm
d_p	Discharge plasma thickness	cm
D	Slab geometry width	cm
D_a	Ambipolar diffusion coefficient	cm^2/s
e	Electron charge	c
E	Discharge electric field	V/cm
E/N	Reduced field	Vcm^2
E_0	Discharge electric-field amplitude	V/cm

Symbol	Description	Unit
f	Excitation frequency	Hz
$f.l.$	Focal length	cm
I_{out}	Emitted laser power-density	W/cm^2
I_{sat}	Saturation laser power-density	W/cm^2
jE	Joule heat power density	W/cm^3
J	Heat flow	W/cm^2
J_1	Discharge conductance current	A
J_d	Plasma capacitive current	A
J_T	Discharge total current	A
ij^ℓ_k	CO ₂ molecule energy-level quanta	
k	Boltzman coefficient	Joule/°K
k_{12}	CO ₂ asymmetric to bending vibration level quenching rate	$Torr^{-1}cm^{-1}$
k_2	CO ₂ bending vibration level quenching rate	$Torr^{-1}cm^{-1}$
k_3	CO ₂ asymmetric vibration level quenching rate	$Torr^{-1}cm^{-1}$
k_a	Dissociative-attachment rate coefficient	cm^3/s
k_d	Dissociative-detachment rate coefficient	cm^3/s
k_i	Ionization rate coefficient	cm^3/s
k_z	Axial wave number	rad/cm
K	Coupling term	
$K.E.$	Kinetic energy	Joules
L	Laser head length	cm
m_e	Electron mass	kg
$M_{x,y}^2$	X and y-axis beam quality	
n_+, n_-, n_e	Positive ion, negative ion, and electron densities	cm^{-3}
\bar{n}_e	Normalized electron density	
n_g	Glass refractive index	
N	Gas density	cm^{-3}
p	Gas pressure	Atm, Torr, kPa
P	Discharge input-power per surface unit	W/cm^2
q	Linear heat flux	W/cm
Q	Accumulated heat per volume unit	$Joule/cm^3$

Symbol	Description	Unit
r	Radius	cm
$R_{\text{opt.}}$	Optimal output coupler reflection	%
R_p	Plasma resistance	$\Omega \text{ cm}^2$
R_s	Metal resistivity	Ω
S	Recombination-region thickness	cm
$\underline{\underline{S}}$	Microwave coupling-agent scattering matrix	
T	Temperature	$^{\circ}\text{K}$
T_0	Wall temperature	$^{\circ}\text{K}$
T_{max}, T_1	Maximal discharge temperature	$^{\circ}\text{K}$
T_2	Temperature at the gas and dielectric-slab grazing surfaces	$^{\circ}\text{K}$
T_e	Electron temperature	$^{\circ}\text{K}$
t_p	Maximal exciting pulse-width under gas-heating restrictions	s
t	Time	s
T	Output coupler transmission	%
v	N_2 vibration level	
v_0	Drift velocity amplitude	cm/s
v_d	Drift velocity	cm/s
v_g	Electromagnetic wave group-velocity	cm/s
$V^{+,-}$	Transmitted and reflected wave amplitudes	V
$V_1^{+,-}$	Port-1 transmitted and reflected wave amplitudes	V
$V_2^{+,-}$	Port-2 transmitted and reflected wave amplitudes	V
V_{in}	Input excitation-wave voltage-amplitude	V
V_s	Total discharge voltage	V
V_{s0}	Space-charge layer voltage amplitude	V
$V_{s1,2}$	Space-charge layer voltage	V
V_p	Plasma voltage	V
V_d	Dielectric-slab voltage	V
X_e	Electron transverse-movement amplitude	cm
z	Axial distance	cm
$Z_{+,-}$	Processes enhancing and depleting the electron density	s^{-1}
Z_{in}	Waveguide input impedance, seen by the magnetron	Ω

1. Introduction

The postulation of stimulated-emission by Einstein dates back to 1917 [1]. By 1940, there was enough information about optical materials and energy levels for fabricating a laser [2], yet, the first device demonstrating the stimulated emission was the maser developed by Townes and co-workers in 1954. In 1958, Townes and Schawlow [3] suggested that the principle of stimulated emission could be also implemented in the infrared and visible regions of the spectrum, but only in 1960, Maiman developed the first ruby laser. A unique device with outstanding physical characteristics, however, with no apparent use at that time.

The first gas laser, the helium-neon laser, was operated by Ali Javan in 1961 in the infrared regime, and in 1962 in the visible regime as the first continuous visible laser. In the same year a different type of laser was invented, the first semiconductor laser employing a small chip of gallium arsenide.

A considerable basic progress in laser research occurred during the period of 1962-1968. Most of the important types of lasers were developed, and were applied to metal welding, cutting, drilling, together with uses such as communications, data storage, sensing, spectroscopy, interferometry, and holography. Many other applications used today were recognized at that period. Yet, lasers were fragile laboratory devices. By the mid 1970s, lasers were used extensively in the industry.

By the end of the 1980s, another significant development in the use of lasers occurred when the semiconductor lasers were combined with optical fibers for long-distance communication. By the year 2000, the worldwide commercial sales of diode lasers exceeded 4.3 billion dollars, after the integration of lasers in consumer products such as compact optical-disks, laser printers, and barcode scanners [4].

Together with uses such as isotope separation of uranium suggested by Yishayahu Nevenzal, applications of high-power lasers are sought for nuclear fusion, military uses, and also x-rays. Thus, one may expect that laser technology and science will continue to grow rapidly [5].

In this study we investigate a new scheme of a CO₂ slab-laser excited by microwaves.

1.1. Lasers Classification

Lasers in practical uses or in advanced research can be divided into two main groups [1]. One group includes lasers that have matured and are widely used, such as gas lasers, solid-state lasers, semiconductor lasers, organic-dye lasers, and optical-parametric oscillators. A second group including chemical lasers, x-ray lasers, and free-electron lasers may find future applications.

Gaseous lasers can be classified into five groups. **Neutral-gas lasers** employ a glow discharge in a neutral-gas mixture such as helium and neon. The helium-neon laser is the most common example for this group. Using a current density of 100 mA/cm^2 , it emits laser radiation at a wavelength of 633 nm, with powers of 0.35-0.50 mW. About 400,000 commercial helium-neon lasers are being sold each year.

Gas ion lasers use a glow-discharge plasma at a high current-density. The most common example for such a laser is the argon ion laser emitting powers of up to 25 W at several spectral lines (524.5, 488.0, 476.5, 501.7, and 334.0-364.0 nm). Other examples are the krypton laser (16 W at 520-576 nm), and the helium-cadmium laser ($\sim 200 \text{ mW}$ at 442 and 325 nm). This type of gaseous laser is mainly used for test and measurement, entertainment, material processing and lithography.

Molecular gas lasers in the infrared use the vibrational and rotational energy transitions of molecules (instead of electronic transitions in the previously mentioned lasers). Therefore, they emit light at the infrared regime. The most important example for a molecular laser is the CO_2 laser, which will be discussed in detail. Regarding maximal power ratings of industrial devices, they can provide a continuous power of up to 45 kW, or energies of up to 100 J in a pulsed-mode operation. They are used for material processing, medical and scientific uses, remote sensing, and various military uses. Other noteworthy examples for molecular lasers are the nitrogen laser used as a relatively simple, high peak-power ultraviolet source (nanosecond MW pulses at $0.337 \mu\text{m}$), and the carbon-monoxide laser ($5\text{-}6 \mu\text{m}$), that has been used for material processing but has been found difficult to maintain.

Excimer lasers use diatomic molecules formed from noble gases under electric-excitation. A common example is the krypton fluoride excimer-laser (249 nm). Using high-energy electron beams for excitation, pulses with energies in the kilojoule regime have been formed for laser assisted thermonuclear fusion and military research. Commercial versions using electrical excitation yield pulsed

energies in the range of tens of joules with average powers of ~ 100 W. These lasers are mainly built for industrial uses.

Metal vapor lasers use a gas discharge that heats a substrate of copper or gold, for example, and maintain the metal in vapor form, as the active media. This is inherently a pulsed laser (up to 20 kHz repetition frequency) with up to 100 W of average power at a wavelength of 511 nm and 578 nm for copper, and 628 nm for gold. This laser is mainly used for high-speed photography and medical applications.

Solid state lasers use an active media composed of a host material containing a small percentage of impurities and are optically pumped. The first laser ever built – the ruby laser – is an example of a solid state laser still used for pulses of high peak-powers (hundred of megawatts by Q-switching), but the most common solid state laser today is the YAG (Nd-doped yttrium aluminum garnet). The neodymium-based lasers operate at wavelengths near 1.06 or 1.32 μm . Nonlinear effects of the crystal and optical parametric-amplifier schemes allow shorter or different wavelengths. The most common types of this laser are the neodymium-YAG laser, the neodymium-glass laser, the neodymium-YLF laser, and the holmium laser. A different class of solid-state lasers, which offer the quality of tunability, is the vibronic solid-state lasers. The main examples for these lasers are the alexandrite ($\text{Cr}:\text{BeAl}_2\text{O}_4$) laser which is tunable over a range of 710-820 nm, and the titanium-doped sapphire laser which is tunable over the large range of 670-1050 nm.

Semiconductor lasers emit a wavelength according to the lattices energy-level characteristics (compared to the impurity electronic-transitions in a solid-state laser). The main commercial diode lasers emit at wavelengths of 630-880 nm, 780-880 nm, 980 nm, and 1150-1650 nm (a few long wavelength examples exist as well). Their power ranges from several milliwatts to watts. While having poor beam-qualities (astigmatic beam-shape with a large divergence) they are small sized, efficient, low-power consuming, and simply driven by a low voltage. Tens of millions are manufactured each year and are found in compact disc players, printers, magneto-optical data storage, and optical-fiber communications. Another application of the semiconductor lasers is the pumping of solid-state lasers such as the YAG and the Ti-sapphire. Manufactured in stacks they are capable of emitting up to 5 kW.

Organic-dye lasers use a small amount of organic dye molecules dissolved in ethyl alcohol or other solvents for the active media. They have the property of large

tunability, and are therefore excellent for spectroscopy. Nevertheless, they need another laser as a pump, thus, they are large and expensive. Offering a tunability of 50-100 nm for each dye material, they cover the spectrum of 370-900 nm with powers of up to 6 W for continuous operation. For pulsed dye lasers (PRF < 1 kHz), peak powers of 20 MW are achieved with an average power of ~ 15 W. Today they are being slowly replaced by solid state lasers, even for spectroscopic applications.

Chemical lasers use chemical reactions to produce population inversion. In some cases an electrical discharge is combined. The most developed chemical lasers are the hydrogen fluoride and the deuterium fluoride, yielding wavelengths around 3 and 4 μm , respectively. Commercial versions of these lasers yield 60 W and 100 W respectively. The oxygen-iodine chemical-laser (1.32 μm) is of interest, having the feature of scalability. Chemical lasers can be scaled to yield up to 100 kW for large models, therefore, they can be used by the military or for material processing. The corrosive nature of the chemical used still poses a difficulty, which needs to be solved before this laser type will be widely used.

X-ray lasers have been explored as sources for coherent radiation-sources in the nanometer regime. Since the mid 1980s, the feasibility of such a laser has been proven several times in experiments with highly ionized plasma. Yet, technology is still far from producing a device that can be used in applications such as the imaging of living cells, lithography with extremely small feature size, and holography.

Free electron lasers are devices in which coherent radiation is attained by converting the energy of a tenuous relativistic electron-beam into electromagnetic radiation. The beneficial characteristics of such a device are its high power, and conceptually, unlimited tunability. Its disadvantages are its cost and large size. Such a device may have a potential use in large facilities such as national laboratories and medical centers.

In view of the laser technology and its uses today [4,5], two main categories can be distinguished, each one fulfilling its growing demand in various applications. For diode lasers, the two main uses are telecommunications and optical storage. An order of magnitude below in demand, one can find (in decreasing order) laser pumps, image recording, entertainment, medical therapeutic, basic research, barcode sensing, inspection measurement and control, and sensing. For non-diode lasers, the main need is for material processing, and in a second place - medical therapy. An order of

magnitude below in demand (in a decreasing order) one can find basic research, instrumentation, image recording, inspection measurement and control, entertainment, sensing, optical storage, telecommunications and barcode scanning.

1.2. The CO₂ Laser

This study is concerned with the CO₂ laser. Patel operated it for the first time in 1964 [6]. Using pure molecules CO₂ gas, it yielded several milliwatts at 10.6 μm . Mixing the CO₂ molecular gas with an RF-excited molecular nitrogen yielded 200 mW of continuous radiation at the same wavelength. An efficient excitation by the vibrationally-excited pure N₂ gas was possible since the first vibrational level of N₂ closely matches the vibrational level of the upper lasing level of CO₂ (a Vibration-Vibration energy transfer). A year later, 106 W of continuous power was achieved using a DC-excited laser mixture composed of CO₂, N₂, and He.

Today, commercial continuous CO₂ lasers reach power levels of tens of kilowatts [1,7,8], and pulsed CO₂-lasers for laser fusion reach the range of 100 J per pulse of less than one picosecond duration [9]. The main use of CO₂ lasers today is in material processing and fabrication. It can be applied to the following processes:

- Vaporizing: cutting, drilling, material removal, etching, inscribing, and trimming.
- Melting: welding, cladding, and alloying.
- Submelting: annealing, hardening, and other phase changes.

The category of therapeutic uses is also occupied to a large extent by CO₂ lasers mainly for [10]:

- Aesthetic treatments: skin rejuvenation, vascular lesions, tattoos, and pigmented lesions treatments.
- Plastic surgery, neurosurgery, oral and maxillofacial surgery, gastroenterology, and thoracic surgery.
- Dentistry, soft tissue and tooth treatment.

CO₂ lasers are slowly integrated into the field of dentistry, even though the first research of CO₂ lasers in this field took place in 1968 [11].

The scientific applications of CO₂ lasers are:

- Spectroscopy: high resolution, saturation, and multi-photon spectroscopy.

- Non-linear optics.
- Raman scattering.
- Pump for tunable lasers.
- Remote sensing and meteorology.

While vastly researched and used for variety of applications, it has been known since an early stage that the main constraints in high laser power-density extraction are associated with dimensions, weight, and price. These limitations are determined mainly by discharge instabilities and the gas temperature. Excessive bulk temperature limits the laser performance by populating the lower laser levels [12].

The quantum efficiency of the lasing process is limited to a maximum of 41 % for the CO₂ laser, yet, the maximal efficiency achieved is ~ 25 %. This stems from the following reasons:

- Only a part of the energy stored by the electrons is used for vibrational energy (80 % maximum).
- Collisions of the CO₂ molecule with other molecules cause non-radiative energy decay.
- The gas temperature rise causes an excess population of the lower laser level, the line width is widened and the rotational-levels population increases.

The above mentioned reasons reassert the importance of an efficient laser cooling which in turn has served as a drive for new laser schemes. The topic of the effective laser cooling will be expanded when the slab configuration is introduced.

1.2.1. CO₂ Laser Excitation Methods

The first generation of CO₂ lasers used DC excitation of the active media, usually cylindrical, by electrodes placed at its axial ends. This excitation method, described in Fig. 1.1, is still applied today in low to medium-power continuous lasers.

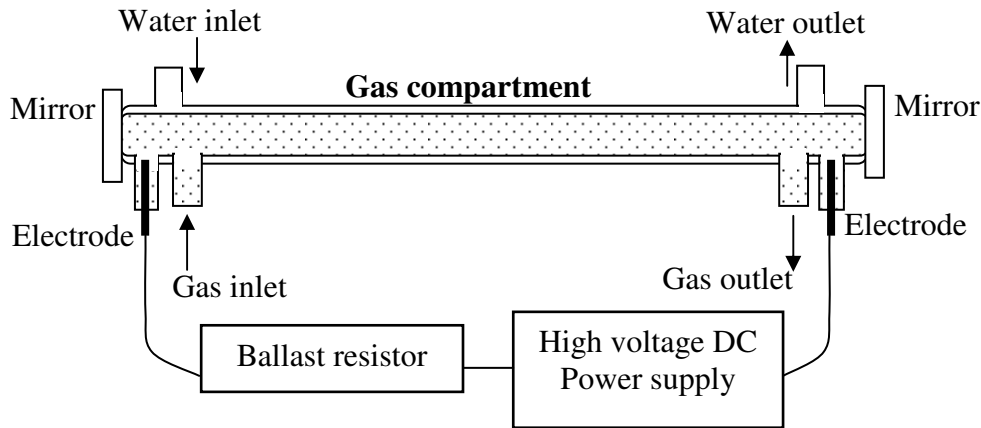


Fig. 1.1: DC excitation of a cylindrical CO₂-laser configuration by internal electrodes.

The main limitation of a cylindrical electrode-excited laser is that the input power cannot be raised by an increased tube diameter (as will be further explained). This results in a constant power per unit length for these lasers. Such sealed industrial lasers yield ~ 1 W/cm. Another limitation of these lasers is their inability to operate at high repetition-rates (PRF > 10 kilohertz), with tens of microsecond pulses, since arcs develop. This led to a different type of laser with a more stable discharge, namely, RF excited lasers [13,14]. When intermediate-power pulsed operation is needed in pulse rates in which arcs develop in an ordinary DC laser, combined DC and RF schemes can be used [15], but these devices are relatively complicated and rather expensive.

One way to overcome the gas-heating constraint is to cool the gas by circulating it through heat exchangers at fast flow-rates. The laser power-densities attained by this method are considerably higher, but the gas circulation and heat exchanging require massive and cumbersome equipment. The gas flow can be axial, or for a more efficient gas cooling - transverse, as demonstrated in the works of Yatsiv [16] and Tiffany [17].

In a gas dynamic laser, population inversion is produced by expansion of a gas, heated to a high temperature, through a supersonic nozzle. Population inversion occurs since

the molecules in the upper laser-state relax more slowly than the molecules in the lower laser-state. This laser type was firstly demonstrated by Kunyukov [18]. Even though output powers in excess of 100 kW are achieved in these schemes, they prove less efficient, larger and more expensive compared to electrical discharge lasers.

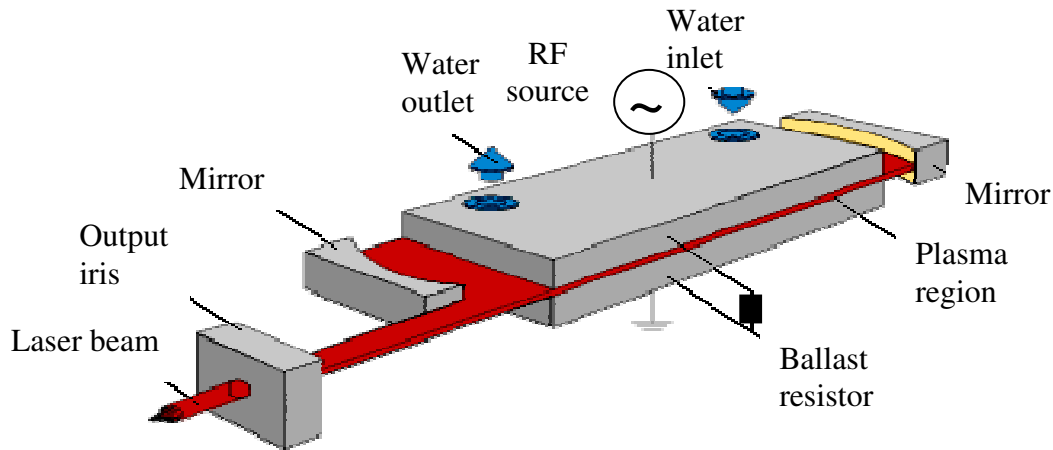


Fig. 1.2: A general scheme of an RF excited CO₂ slab-laser.

A different mechanism of gas cooling was suggested independently by Vaisfeld [20], Yatsenco [21], and Yatsiv [22]. They proposed to form a radio-frequency homogeneous discharge between two parallel cooled-electrodes. This configuration, called the stipline or slab configuration, allows the fabrication of compact medium-power lasers that do not require gas flow. Benefits such as electrodeless discharge, low operating voltages, and a stable discharge at high power densities, characterize this laser. Since the early 1990's the advantageous characteristics of the 2.45 GHz magnetron for laser excitation were explored in various schemes [25-32], and also the slab configuration. In several devices the slab configuration was scaled to form high-power laser arrays [34-36]. A basic scheme of a microwave-excited CO₂ slab-laser is shown in Fig. 1.3. In the present research, the slab-configuration microwave discharge is investigated using a magnetron radiation source. A comparison between RF and microwave CO₂-laser excitation is outlined in the next Chapter.

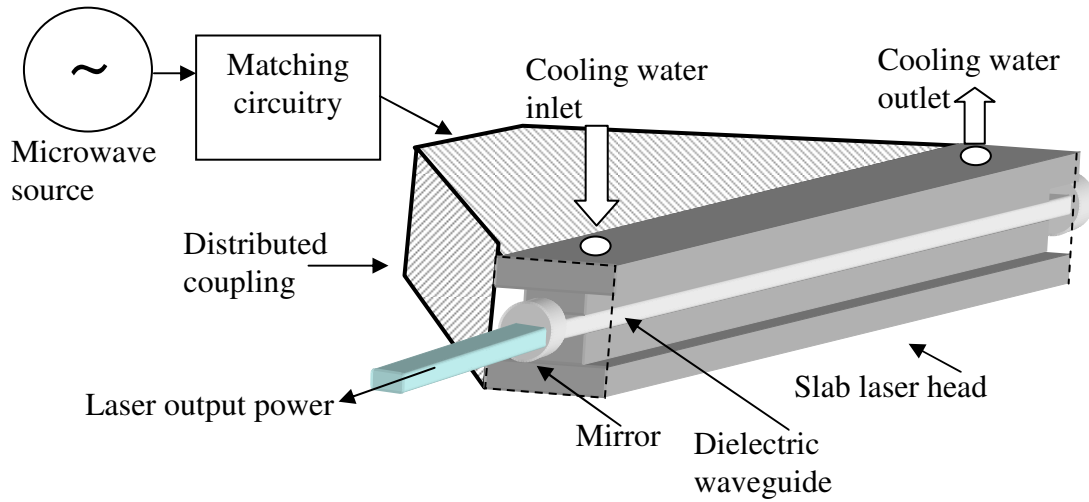


Fig. 1.3: A general scheme of a microwave-excited CO₂ slab-laser.

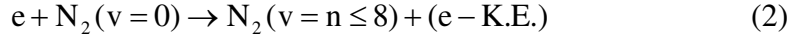
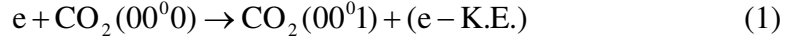
Lasers in which high peak energy-pulses are attained in relatively compact devices are the TEA (Transversely Excited, Atmospheric pressure) lasers [37]. These inherently pulsed devices operate at a gas pressure of ~ 1 Atm, which allows the extraction of large amounts of energy per pulse. The high operating gas-pressure limits the laser pulse to a regime in which arcs do not develop (several microsecond pulses at a frequency less than 1 kHz). Operated first in the early 1970's, it is now an important tool for material processing.

In the next paragraph, the energy-transition kinetics of CO₂ lasers is outlined.

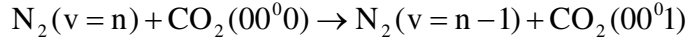
1.2.2. Energy-Transitions Kinetics in CO₂ Lasers

A common CO₂ laser gas-mixture for which much of the existing CO₂-laser data pertains is CO₂:N₂:He = 1:1:8. Fig. 1.4 (Page 24) presents an energy level diagram for such a mixture. The CO₂ symmetric molecule maintains three types of vibration denoted by ν_{1-3} . Four integer numbers ($ij^\ell k$) denote a specific energy level. i , j , and k denote the degree of excitation of the symmetric, bending and asymmetric vibration, respectively, and the integer $\ell = 0, 1$ specifies different degenerate perpendicular bending vibration levels.

The excitation of the upper laser level occurs by two processes described by Eqs. 1-2 [12]



followed by



where K.E. stands for the kinetic energy in joules, and v represents one of the first eight N_2 vibration levels. It is assumed that the CO_2 molecule excitation cross-section decays significantly beyond the N_2 eighth vibration-level, since higher-levels population is negligible. Moreover, the harmonic approximation for the energy gaps is no longer valid. This significantly reduces the efficiency of the N_2 and CO_2 molecules vibration-vibration energy transfer.

The effectiveness of the excitation by electrons (Eq. (1)) is determined by the electron energy [38,39], set by the reduced field E/N . E and N denote the discharge electric field, and the gas density, respectively. When the reduced field fits the value appropriate for effective electron-excitation of the upper laser-level (00^01), the lower laser levels (10^00 , 02^00) are excited with a lower efficiency. Thus, population inversion is possible by direct electron excitation, as expressed in Eq. (1).

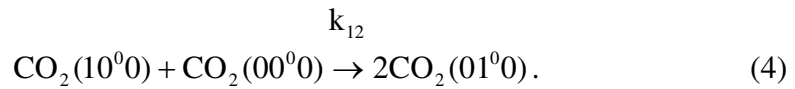
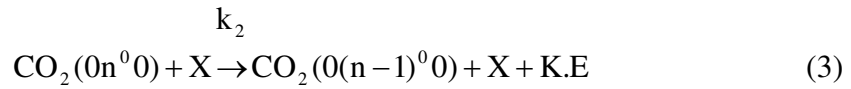
Eq. (2) describes the second excitation channel in which a vibration-vibration energy transfer occurs between the excited N_2 and the CO_2 molecules. As evident from Fig. 1.4, the vibrational level of the upper laser level (00^01) matches the first vibration level of the N_2 (18 cm^{-1} energy difference) [40]. Thus, a vibration-vibration energy transfer from N_2 molecules also excites the CO_2 molecules (Eq. (2)). The N_2 molecule, being metastable, loses its energy only by collisions with the other gas components. One can assume that the energy difference between successive vibration levels in an N_2 molecule is negligible (harmonic approximation), therefore, a fast energy transfer occurs between $\text{N}(v = n)$ and $\text{CO}_2(00^00)$ [12].

The He molecule's first quantum state lies 24 eV above the ground level, which is 67.7 times the spacing of $v = 1$ to $v = 0$ in the N_2 molecule. While the effective electron energy for CO_2 asymmetric-excitation is about 1 eV, the probability of inelastic collisions of the He molecule is low. Thus, the He molecules improve the

heat conductivity of the laser mixture, and increase the quenching rate of the lower laser levels, as evident from Table 1.1. k_2 and k_3 in Table 1.1 are the quenching rates for the bending and asymmetric vibration branches, respectively. For the He molecules $k_2 \gg k_3$, therefore, the quenching rate of the lower laser levels is faster in a laser gas-mixture containing a large percentage of He. Eqs. (3), and (4) describe the depletion of the bending and the symmetric branches, respectively where X is one of the gas components (i.e. CO₂, N₂, or He).

Gas type	Quenching rate k_2 [Torr ⁻¹ s ⁻¹]	Quenching rate k_3 [Torr ⁻¹ s ⁻¹]
CO ₂	194	350
N ₂	650	106
He	3270	85

Table 1.1: Quenching rate of gas components for the bending vibration branch (02⁰0), k_2 , and for the asymmetric vibration branch (00⁰1), k_3 .



k_{12} in Eq. (4) is the quenching rate of the asymmetric to bending vibration-vibration energy transfer. In practice $k_{12} \gg k_2$, therefore the process described by Eq. (3) (the depletion of the bending vibration levels) poses a more stringent limitation over the lower levels depletion-time.

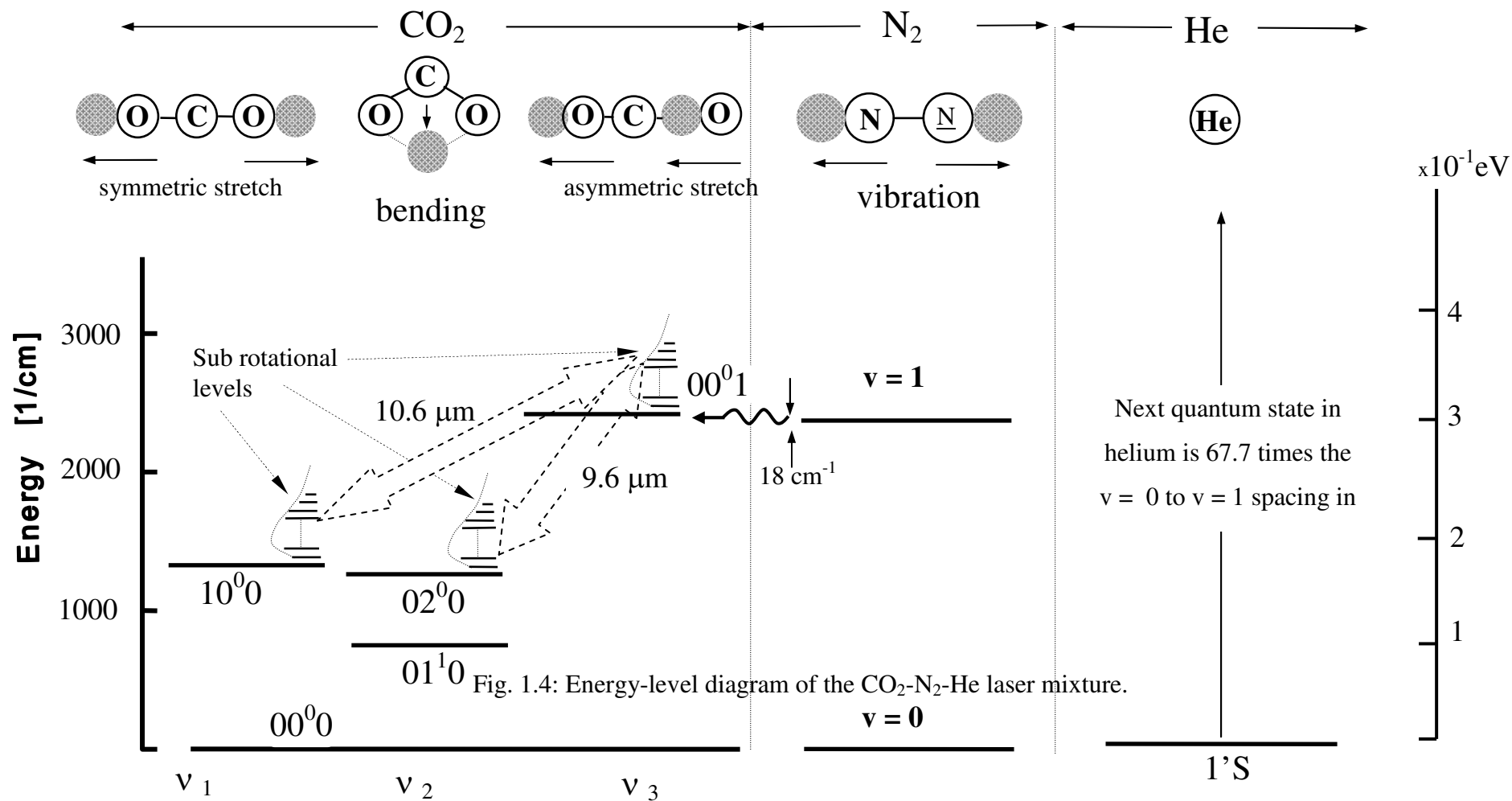


Fig. 1.4: Energy level diagram for a common CO_2 laser gas-mixture for which much of the existing CO_2 -laser data pertains is $\text{CO}_2:\text{N}_2:\text{He} = 1:1:8$. Fig. 1.4.

The addition of xenon (Xe) to laser mixtures, especially in sealed-off schemes, was investigated in several works [42,43]. It was found that an addition of up to 5 % of Xe to the mixture, improves the laser performance. By lowering the dissociation rate of the CO₂ molecules, and by lowering the electrons' temperature to match the effective excitation of the upper laser-level, the laser's efficiency is increased.

1.2.3. CO₂ Slab-Lasers

In a CO₂-laser discharge, the energy of the laser emission at optimal conditions is relatively small compared to the energy transfer to translation and rotation. This is the reason for assuming that most of the discharge energy is converted into heat. As asserted previously, three separate mechanisms dominate the degradation of the gas-laser performance as a result of a temperature increase. Due to the strong coupling of the translation energy of the molecules to the lower laser-levels (10⁰0, and 02⁰0), an increase in their population follows a temperature increase. Thus, a direct decrease in the population inversion occurs [12].

The CO₂-laser line-width broadening is affected mainly by two factors. In pressures less than 50 Torr, the Doppler broadening dominates [12]. A temperature increase changes the kinetic energy of the molecules, which in turn, results in a lowered laser-gain due to the line broadening. At pressures between 50-100 Torr, the line broadening is a convolution between the Doppler broadening and a pressure broadening. At higher pressures the pressure-broadening dominates.

The energy spacing between the low rotational levels of a given vibration is of the order of $\sim 10^{-4}$ eV. This is lower than the average translation energy of the gas ($kT \cong 0.03\text{eV}$, where k is the Boltzman constant). As a result, the temperature characterizing the rotational-levels population distribution is approximately the translation temperature. Therefore, an increase in the gas temperature opposes a selective population of the molecules rotational energy levels. As a result, the density of population inversion between the lasing energy-levels will eventually decrease, according to quantum selection rules.

By considering the above-mentioned mechanisms, the importance of an efficient laser cooling is understood. In the next paragraph we outline the cooling

characteristics of two laser configurations, namely, a cylindrical and a stripline structure.

1.2.3.1. Heat Flow Considerations

A cross-section of the cylindrical CO₂-laser is presented in Fig. 1.2. An inner cylindrical tube with radius r , is placed inside a cooling jacket in which a cooling liquid is flowing.

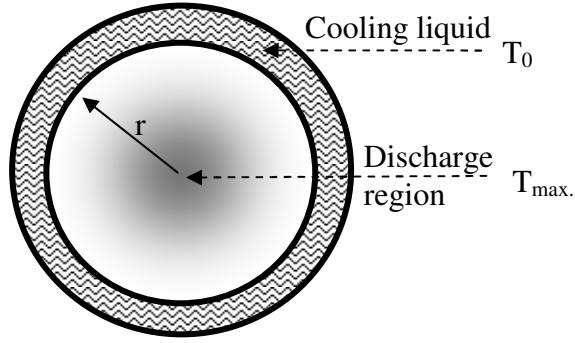


Fig. 1.2: A cylindrical CO₂-laser cross-section.

The maximal discharge temperature ($T_{\max.}$) develops at the center of the cylinder, whereas the cooling jacket maintains the tube envelope temperature (T_0) at the cooling-liquid temperature. The heat flow from the tube center to its envelope is determined by the temperature gradient as

$$J = -\kappa \nabla T \quad (5)$$

where $\kappa \left[\frac{\text{W}}{\text{cm}^\circ\text{K}} \right]$ is the heat conductivity of the gas. The linear heat-flux per unit length (q) is therefore

$$q = J 2\pi r \cong \kappa \frac{\Delta T}{r} 2\pi r = 2\pi \kappa \Delta T \quad (6)$$

where ΔT denotes the temperature difference between the enclosing wall and the tube center ($\Delta T = T_{\max.} - T_0$). The result shows that the linear heat-flux does not depend on radius. In other words, enlarging the tube diameter for a given input power does not change the gas temperature, when the gas is mainly cooled by conduction.

Even though Eq. (6) is written assuming a linear temperature-variation, the results also apply for an exact analytical calculation [44].

Following the works of Yatsiv [22], Abramski *et al.* [23], and Nowak *et al.* [24], the diffusion-cooled slab configuration was explored. In this configuration, the heat-removal limitation of the cylindrical configuration is annulled. The slab configuration is shown in Fig. 1.3.

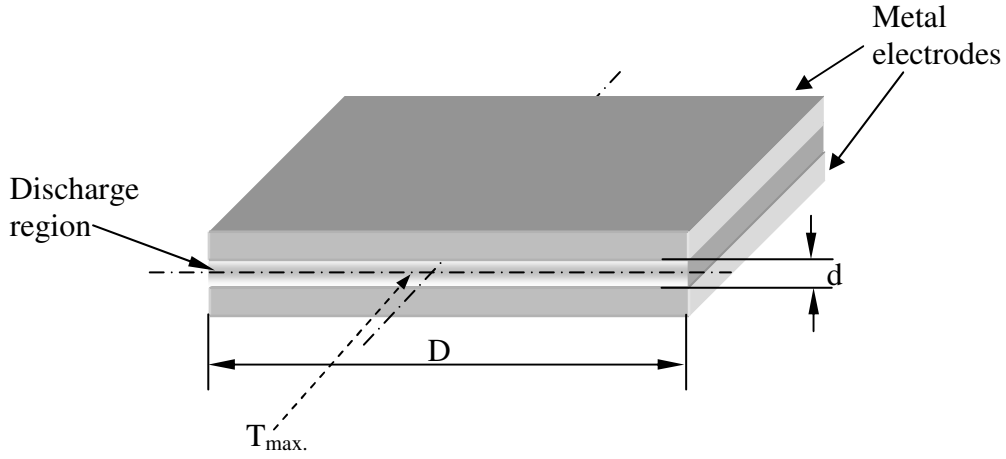


Fig. 1.3: The slab-laser electrodes' configuration.

Conducting the same calculation performed for the cylindrical configuration, for a linear temperature-variation approximation, the heat flux for the slab configuration is found to be

$$J = -\kappa \nabla T \cong \kappa \frac{\Delta T}{d/2} \quad (7)$$

where d is the discharge width. The linear heat-flux to the electrodes per unit length is therefore

$$q = JD = 2\kappa \frac{\Delta T}{d} D, \quad (8)$$

where ΔT is the temperature difference between the maximal, at the center of the discharge gap, and that of the cooled electrodes. It is evident that the rate of heat removal is inversely proportional to the discharge width. The heat transfer equation, under an assumption of a linear temperature variation is

$$\frac{\partial Q}{\partial t} = -\nabla \cdot \mathbf{J} + \frac{P}{d} \cong -\kappa \frac{\Delta T}{(d/2)^2} + \frac{P}{d} \quad (9)$$

where Q is the accumulated heat per volume unit, and P is the input power into the discharge per surface area. Assuming steady-state conditions, the relation of P and ΔT is found to be

$$P \cong \kappa \frac{4\Delta T}{d}. \quad (10)$$

The benefits of the slab configuration regarding the heat removal are evident. One can raise the input power into the discharge region and simultaneously decrease the discharge width to maintain a constant temperature difference. The maximal allowed temperature for efficient CO_2 laser operation is about 500°K , enabling a steady state temperature difference of $\Delta T \cong 200^\circ\text{K}$. Increasing the input power and decreasing the discharge width, both raise the discharge electric field. Thus, in order to maintain an optimal laser operation, the gas pressure should be raised to maintain the appropriate reduced field (E/N).

A second basic difference between the slab configuration and the cylindrical one is that the input power is proportional to the electrode surface (and not to the axial length only). By scaling the laser surface, compact industrial lasers have reached continuous powers of 1 kW, with power densities of above 1 W/cm^2 . While exhibiting an excellent performance at continuous-operation medium to high powers, the slab configuration cannot yield high peak power bursts comparable to TEA lasers. The reason is that for high peak powers, the gas volume and pressure should be increased

while maintaining the optimal reduced field. In such a situation, a stable discharge cannot be sustained in a slab configuration. A solution to this difficulty is to apply a different mode of pulsed operation. A pulse duty cycle is determined in the following way: the excitation pulse raises the gas temperature momentarily to the maximal value for efficient lasing for a period of time in which discharge instabilities do not develop. At the time interval between pulses, gas cooling by conduction or convection takes place. In such a mode of operation, the average gas temperature does not exceed the maximal allowed for efficient lasing. Combining this method of operation with the high peak to average power-yield of microwave sources proves highly beneficial. It may yield compact lasers with high peak and average powers, characterized by a high peak to average laser-powers ratios, in tens of microsecond pulses, in the kilohertz regime. The device presented in this work proves the feasibility of a compact, slow gas-flow or sealed microwave-excited laser, which is easily optimized regarding the heat removal, and the microwave matching considerations.

The outline of the thesis is as follows: The subject of microwave discharges and a summary of the research motivation are given in Chapter 2. Next, we focus on two of the main microwave excitation limitations, namely, thermal instabilities and a longitudinally homogeneous discharge formation. Chapter 3 discusses in detail the subject of microwave discharges thermal-instabilities, and presents a thermal optimization method for pulsed microwave-excited slab lasers. The experimental setups designed and built in the framework of this thesis are presented in Chapter 4, showing the feature of a longitudinally homogeneous microwave-discharge. The presentation of an experimental device is succeeded by a description of its experimental results. Chapter 5 discusses in detail the results of the main experimental device investigated in this thesis, namely, the microwave-excited CO₂ slab-laser.

2. The Electrical Discharge in Slab Lasers

This chapter describes the main gas-discharge processes taking place in a CO₂ laser. Understanding these phenomena assists in the characterization of the microwave discharge. A comparison between the three main CO₂ laser excitation methods, namely, DC excitation, RF excitation (up to 300 MHz), and microwave excitation (above a frequency of 300 MHz), is provided. This chapter presents the beneficial characteristics and operational advantages of a microwave-excited CO₂ slab-laser. The construction considerations of this laser are derived in the following chapters according to the gas-discharge phenomena described in the succeeding sections

2.1. Gas Discharge Processes

A general chain of events can be outlined for a molecular-gas laser discharge [45]. An external power source (DC, RF or microwave) ionizes the gas, thereby generating free electrons. The free-electron energy contributes to four dependable processes, namely

1. Molecular ionization and electron-ion recombination
2. Excitation of electronic molecular states
3. Excitation of molecular vibration states
4. Molecular rotation and molecular translation.

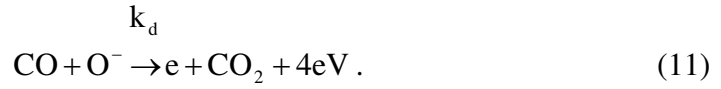
Lasing occurs due to vibrational-rotational transitions of the CO₂ molecule. An additional independent process related to the free electrons and the molecules as well, is the heat conduction to the discharge walls. The main plasma processes taking place in a CO₂-laser discharge [46-51], can be divided into three groups

1. Processes by which free electrons are generated
2. Processes by which free electrons are lost
3. Vibrational excitation of CO₂ and N₂ molecules.

Processes that raise the free-electron density are: ionization, and dissociative-detachment described by Eq. (11). k_d is the dissociative-detachment rate coefficient. Carbon monoxide molecules and oxygen negative-ions form a neutral carbon-dioxide molecule by attachment, releasing an electron with a residual kinetic energy. Table 2.1 outlines the ionization threshold energies for typical laser mixture components.

Gas component	Ionization energy [eV]
Xe	12.1
CO ₂	13.8
N ₂	15.5
He	24.5

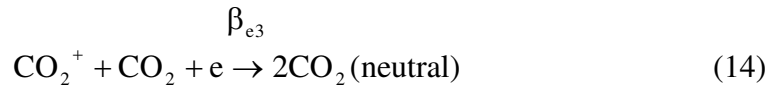
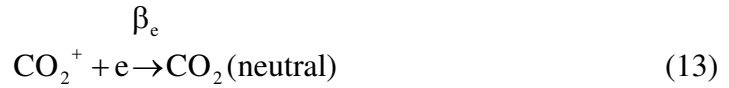
Table 2.1: The ionization energies for common laser-mixture gas types.



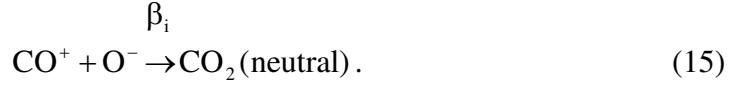
Free-electrons are lost by dissociative-attachment, electron-ion recombination, and by drifting or diffusing to the walls. The dissociative-attachment process, which is complementary to the one described by Eq. (11), is given by



where k_a is the dissociative-detachment rate coefficient. An electron with the appropriate kinetic energy causes the CO₂ molecule to split to a CO molecule and an oxygen negative ion. Equations (13) and (14) describe the electron-ion two-body recombination and the three-body recombination, respectively,



where β_e and β_{e3} are the two and three body recombination-rate coefficients. Another important recombination process is the ion-ion two-body recombination described by



The time required for an electron to pass from the cathode to the anode, under DC excitation, determines the electron drift-loss. This loss mechanism in conventional DC-excited lasers is negligible compared to other loss processes due to the long electron drift space. However, this is the dominant loss mechanism in DC excitation of a slab configuration because of the short discharge length (a few millimeters). Offsetting the electron density in such a scheme is achieved by raising the electric field for increased ionization rate. The resulting reduced field (E/N) which determines the excitation efficiency for the upper laser level is consequently much higher than the optimal value. An application of a cross magnetic field [52] was suggested for stabilizing such a discharge, and for extending the effective electrons' free path before diffusing to the walls.

In RF excitation of a slab laser, electron density optimization can be achieved [53-56]. The electrode polarity in such a configuration alternates every half cycle, so a proper frequency can be set (which changes the direction of the electron before it reaches an electrode). The drift losses in such a configuration are small, and are negligible compared to other loss processes.

The process of vibrational excitation is dependent on the excitation cross-section of the N_2 first eight vibration-levels, which peaks at ~ 2.5 eV, and the excitation cross-section of the upper laser-levels, which peaks at ~ 1 eV [49]. The electron energy is ultimately dependent upon the reduced field. The addition of Xe enhances the vibrational excitation [42,43]. As stated in Table 2.1, the ionization potential of Xe is 12.1 eV. The molecules that are primarily ionized in the laser mixture are the N_2 and CO_2 (with 15.5 eV, and 13.8 eV ionization potentials). Therefore, most free electrons ionizing the Xe have energies higher than 12.1 eV. After ionizing the Xe, these electrons remain with lower kinetic energy, which is more suitable for efficient vibrational excitation.

2.2. RF and Microwave Discharges

The discharge type in which the electrons have the proper energies for efficient laser operation is the glow discharge [47]. In a typical glow discharge, eight discharge regions can be distinguished, as a result of the ion and electron densities and drift velocities. In the RF-excited slab configuration, the two parallel metallic-strips form a capacitively-coupled discharge. Such a discharge is distinguished by two main regions, namely, electrode space-charge sheaths, and a natural-plasma region in between, as presented in Fig. 2.1. The applied field, initiating the discharge, causes the formation of free electrons, which are alternately drifted to the electrodes leaving a sheath depleted of electrons (considering the mass ratio between electrons and ions) [47,56]. The electron motion equation is

$$m_e \frac{dv_d}{dt} = -eE - m_e v_d v_c \quad (16)$$

where e , m_e , and v_d are the electron charge, mass, and drift velocity, respectively, and v_c is the molecules' collision frequency approximated by $v_c = 1.75 \cdot 10^{12} \text{ p[Atm]}$. The solution of Eq. (16) for a discharge field of the form $E = E_0 \exp(i\omega t)$, where ω is the field radial-frequency, is

$$V_d(t) = v_0 \exp(i(\omega t - \Phi)). \quad (17)$$

The drift-velocity amplitude is $v_0 = \frac{e/m_e}{\sqrt{v_c^2 + \omega^2}} E_0$. The velocity phase determined by

the excitation and collision frequencies is $\Phi = \tan^{-1}(\omega/v_c)$. The amplitude of the electron transverse movement (X_e) is found by integration over the drift velocity as

$$X_e = \frac{e/m_e}{\omega \sqrt{v_c^2 + \omega^2}} \text{Re}\{E_0\}. \quad (18)$$

The gas pressures in which we operate our lasers dictate $v_c \gg \omega$, therefore we get

$$v_d(t) = \frac{e}{m_e v_c} E(t) = \mu_e E(t) \quad (19)$$

$$X_e = \frac{e}{m_e \omega v_c} \text{Re}\{E_0\}. \quad (20)$$

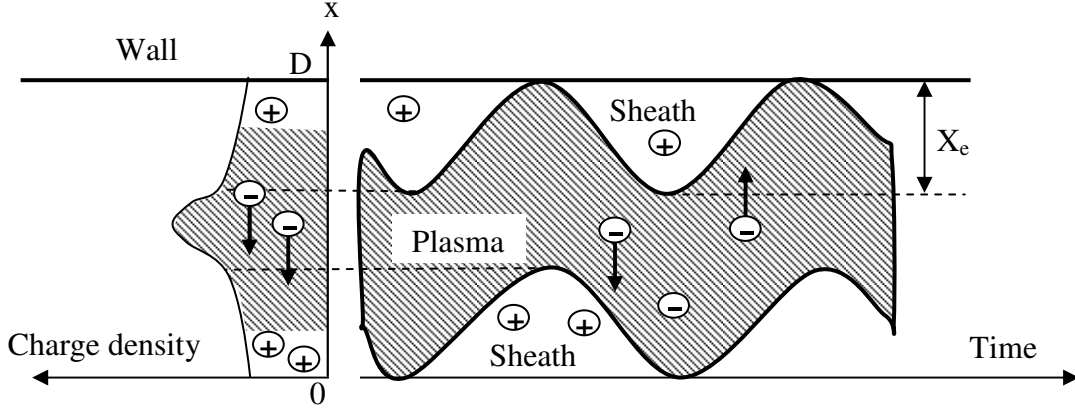


Fig 2.1: The space-charge structure of the capacitively-coupled RF discharge.

Figure 2.1. shows the two regions formed in the discharge zone, namely, the electron drift zone, and the depletion layers which are almost free of electrons. The relation between these layer thicknesses, as discussed in the next sections, is mainly determined by the excitation frequencies. For an RF excitation frequency of ~ 100 MHz, the thickness of a depletion layer is in the order of 0.5 mm, and for a microwave excitation frequency of ~ 1 GHz it is an order of magnitude thinner.

2.2.1. Two Modes of Stable Discharges in an RF-Excited Slab Laser

The glow discharge in an RF-excited slab-laser device is characterized by two separate but stable forms of discharge [56]. These two discharges are labeled α and γ after the two Townsend discharge constants, pertaining to volumetric ionization and secondary emission of electrons. In the following sections we formulate the basic characteristics of these discharge modes, and discuss their importance for an efficient laser operation.

2.2.1.1. The α Discharge

This form of stable discharge is characterized by the formation of electrons due to volumetric ionization only. The two main regions observed in this discharge are the plasma region and the electrode space-charge sheaths (Fig. 2.1). The plasma region occupies most of the discharge region, and it is electrically neutral (with equal electron and positive-ion densities). The electrode sheaths are found between the plasma region and the discharge walls. They are populated with positive ions, with a density similar to that of the electrons in the plasma region. The electric field and luminescence of the α discharge are presented in Fig. 2.2, together with an experimental demonstration (a detailed presentation of the experimental setups will follow in the next chapters).

The charge separation between the two discharge regions creates a strong electric field. At the electrode surface, there is a dark strip (Aston dark space) due to the low electron energy. Close to the electrodes, the electron's charge density is low due to their diffusion to the walls. Therefore, the luminescence is weak and grows along the sheath. The luminescence decreases at the grazing surfaces between the two discharge regions due to (a) the electric field at the plasma region decreases relative to the depletion sheath, (b) the electrons lose energy by ionizing molecules. The low electron energy at the plasma region in the α discharge is suitable for efficient vibrational laser-excitation.

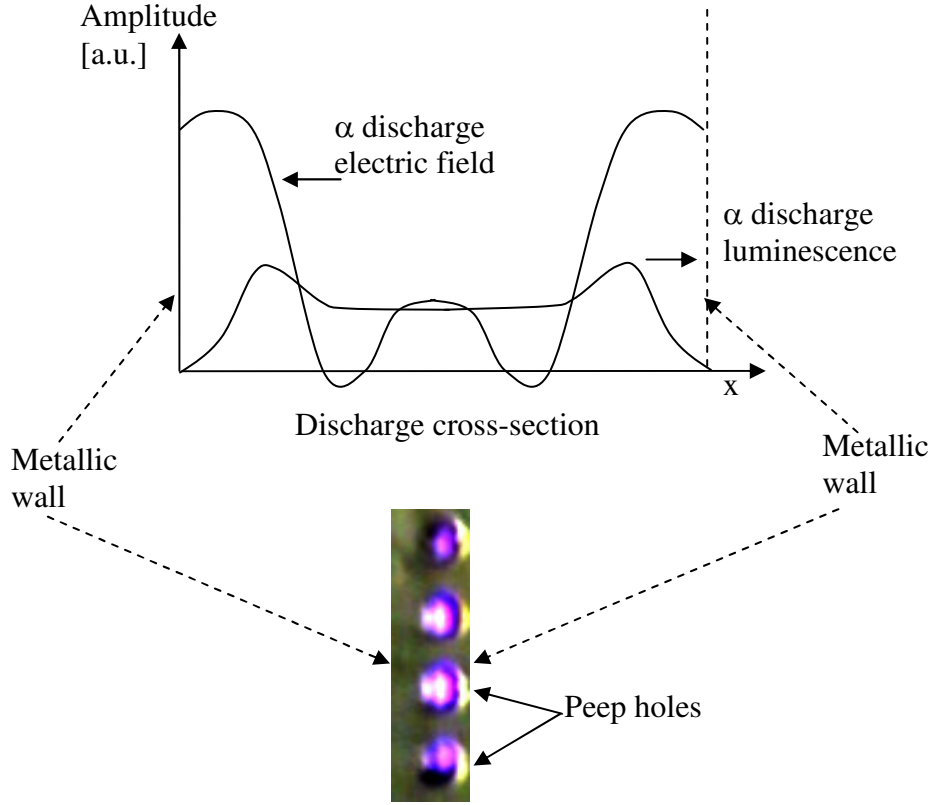


Fig. 2.2: The α discharge electric-field, and its luminescence observed through peep holes located along the laser discharge.

The width of the space-charge sheaths varies with time, as depicted in Fig. 2.1, between X_e , and S , where S is the recombination-region thickness (the dark layer close to the electrode). S is estimated by [56]

$$S = \frac{\pi}{2} \sqrt{\frac{D_a}{k_i N}} \quad (21)$$

where k_i is the ionization-rate coefficient, D_a is the ambipolar (charge separation) diffusion coefficient, and N is the molecular density of the gas. Unlike X_e , S does not depend on the frequency. It can be approximated in common laser mixtures by $S \text{ [mm]} \cong 6/p \text{ [Torr]}$, which is negligible for RF frequencies, but not for microwave discharges. The thickness of the space charge layers, at a given time, is found to be

$$d_1(t) = \frac{d_0}{2} [1 - \cos(\omega t)] \quad (22)$$

$$d_2(t) = \frac{d_0}{2} [1 + \cos(\omega t)], \quad (23)$$

for the first and the second sheaths, respectively. The maximal width of the sheaths d_0 is

$$d_0 = X_e + S. \quad (24)$$

The electrode-sheaths voltages, found by solving the Poisson equation, are

$$V_{s1}(t) = \frac{V_{s0}}{4} [1 - \cos(\omega t)]^2 \quad (25)$$

$$V_{s2}(t) = \frac{V_{s0}}{4} [1 + \cos(\omega t)]^2 \quad (26)$$

for the first and the second sheaths, respectively. The sheath's maximal voltage amplitude V_{s0} is

$$V_{s0} = 2\pi e n_+ d_0^2 \quad (27)$$

where n_+ is the positive ion density in the layer. The equivalent capacitance per unit length, formed by the charge separation of the two layers is

$$C_s = (4\pi d_0)^{-1} \quad [\text{cm}^{-1}]. \quad (28)$$

The plasma-region voltage as a function of the input-power remains unchanged during a discharge current increase. However, the sheaths voltage increases, following the ion density rise (Eq. (27)). The plasma reduced-field (E/N) does not change as a consequence when the input power-density is raised. Thus, one of the main advantages of an RF capacitively-coupled discharge is that while increasing the input power-density, the effective laser-excitation parameters remain unchanged. The capacitive

nature of the sheaths allows them to act as a discharge ballast, compensating for the changes in the plasma region voltage and current [56].

When the excitation frequency is raised, the sheath width decreases (Eqs. (20), (24)). As a result, a microwave α -discharge does not benefit the sheaths stabilization and must be stabilized by other means, as will be outlined in the next chapter.

2.2.1.2. The γ Discharge

Increasing the power density in an RF discharge beyond a certain level gives rise to a different stable mode of a discharge, namely, the γ discharge [57]. As discussed previously, the space-charge sheath voltage increases with the input-power rise, and at a certain stage (Paschen breakdown point) a breakdown will occur in the sheath. The breakdown structure of the inter-electrode spacing will now resemble a common DC glow discharge in which the sheath serves now as the main electron source. It is characterized by a high current density for which the reduced field (E/N) is not suitable for efficient vibrational-excitation. Following the discharge-area decrease, it is no longer capacitive as for the α discharge. Figs. 2.3a, and 2.3b demonstrate the transition between the two stable discharge-modes [21,56,62].

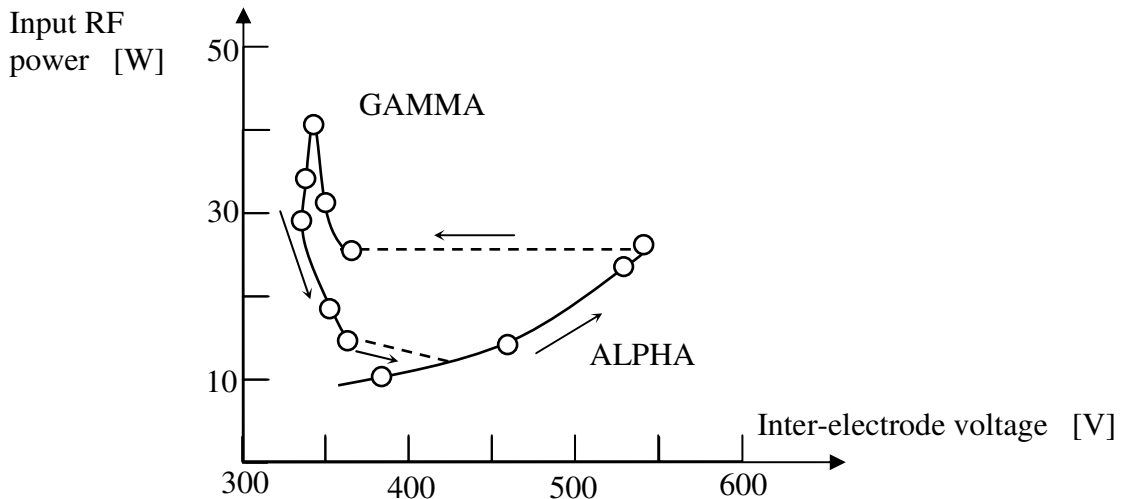


Fig. 2.3a: The $\alpha \rightarrow \gamma$ discharge transition in a 15 MHz RF-discharge in a $\text{CO}_2:\text{N}_2:\text{He} = 1:1:3$ mixture at a pressure of 55 Torr, and electrode spacing of 6 mm [62].

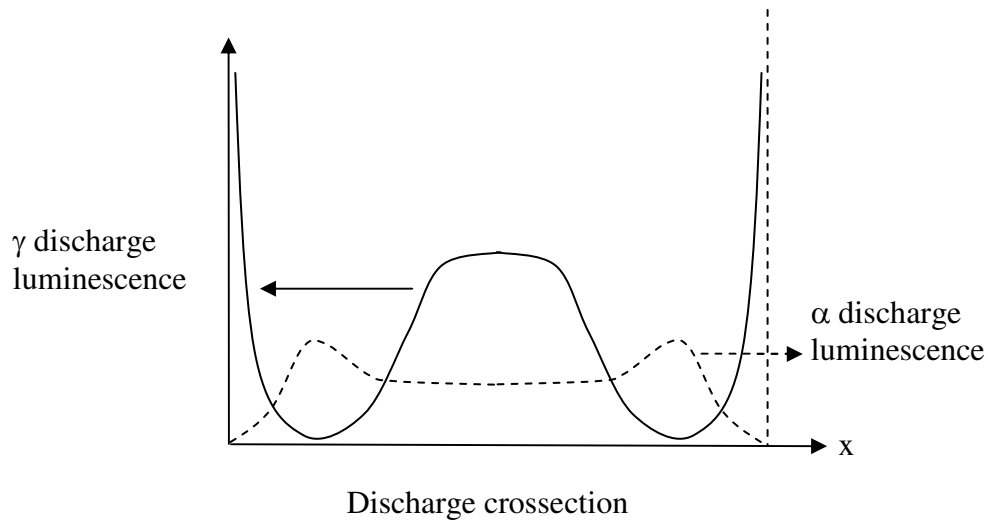


Fig. 2.3b: The γ and α discharge luminescence [21,56].

The $\alpha \rightarrow \gamma$, and $\gamma \rightarrow \alpha$ transitions are presented on an input-power versus the inter-electrode voltage chart in Fig. 2.3a. Fig 2.3b depicts the luminescence of the γ discharge compared to the α discharge.

It was found that when the source frequency is increased, the $\alpha \rightarrow \gamma$ transition occurs at a higher voltage [58,59]. For example, in a $\text{CO}_2:\text{N}_2:\text{He} = 1:1:3$ mixture at a pressure of 55 Torr, a variation of the source frequency from 27 MHz to 125 MHz results in doubling the transition-point voltage [60]. This occurs as explained previously because of the sheaths narrowing, resulting in a Paschen breakdown-point change. This result presents one of the beneficial characteristics of the high-frequency microwave discharge. A microwave frequency will cause a depletion-sheath width of a few tenths of a millimeter. At medium gas pressures (up to ~ 150 Torr) the breakdown voltage of the depletion layer will be extremely high, much higher than the characteristic glow-discharge voltage. Thus, the probability that the $\gamma \rightarrow \alpha$ discharge transition will take place in a CO_2 slab-laser microwave discharge is considerably lower, compared to an RF discharge.

2.2.2. RF vs. Microwave Discharges

The RF discharge in a slab configuration presents the following benefits when compared to DC excitation [60]:

1. The possibility of electrodes external to the gas, which is most important for sealed device-operation.
2. Low voltage operation which is technically safer.
3. Stable discharge at pressures and input power-densities higher than the typical ones for DC excitation.
4. The absence of the DC discharge cathode region, characterized by a large electron-density with high energies (which are not suitable for efficient α discharge vibrational-excitation).
5. The discharge frequency adds as a variable parameter determining efficient lasing.
6. The electron effective path length is extremely larger than for DC excitation.

Nevertheless, the main disadvantage of the RF excitation for high-pressure pulsed operation, is the high price of RF generators producing peak powers of above 10 kW, and average powers above 1 kW. Besides their high cost and usually large-dimensions, their efficiency often does not exceed 40 %. Another limitation that stems from the physical mechanism of operation of these sources, is their inability to supply a large peak to average RF power ratio. In most schemes the peak pulsed-power of an RF source equals its maximal average-power. The previous section outlined a different restriction over the peak to average laser power ratio. As described, high input power-densities in an RF-excited slab configuration might cause the undesirable $\alpha \rightarrow \gamma$ transition, followed by a significant deterioration of the laser performance.

The microwave excitation of a slab laser offers solutions for the RF discharge limitations, but presents new difficulties to be considered. The main microwave excitation source is the magnetron. This rugged microwave tube has an efficiency of ~ 70 %. It is capable of producing large peak to average power ratios. Following the extensive use of magnetrons in domestic, as well as industrial applications, their price is minor compared to the other laser-system components. Several works have demonstrated the implementation of an industrial magnetron in cylindrical fast-flow

lasers as well as slab lasers. A fast-flow cylindrical configuration devised by Freisinger *et al.* [25] used an active media 30 cm long and 5 cm in diameter, yielded an average laser-power of 700 W with a 20 % conversion efficiency. Nishimae [29] produced 110 W of average laser power (peak to average power ratio of ~ 10) with a conversion efficiency of ~ 18 %, in a slab configuration with dimensions of $400 \times 20 \times 2 \text{ mm}^3$.

Another beneficial characteristic of the microwave excitation is the cancellation of the $\alpha \rightarrow \gamma$ transition. As explained in previous sections, the discharge space-charge sheath width narrows when the frequency is raised (for a 2.45 GHz of a commercial magnetron, the sheath width is $d_0 \cong 0.03 \text{ mm}$). The decrease in the sheaths width - significantly increases the sheath breakdown voltage. This results in the cancellation of the $\alpha \rightarrow \gamma$ transition, and allows the insertion of high power-densities.

Even though the microwave excitation offers beneficial conditions for CO_2 laser excitation, it also presents several major difficulties. The RF excitation of a slab-configuration discharge-gap maintains electrons in the discharge region as long as the frequency is large enough. By changing the electrode polarity, the electron swings from side to side (transversally), without diffusing to the walls. If the excitation frequency is too large, the electron-movement amplitude will be negligible, thus, decreasing the efficient volumetric-excitation of the laser. Vitruk [61] has found a new scaling factor for RF excited lasers which is $fd = \text{constant}$, where f is the excitation frequency and d is the discharge width. This condition sets a frequency allowing the electron to move across the whole plasma region and remain there. For the common frequency of 2.45 GHz, the effective discharge-width is on the order of $\sim 0.1 \text{ mm}$. Such electrode spacing is not favorable for a CO_2 laser due to increased optical losses in the electrodes [63-65].

Another difficulty presented by the microwave excitation is the short free-space wavelength of the source (12 cm for 2.45 GHz). When constructing a laser, physically much longer than half the free-space wavelength, two difficulties arise:

1. Matching - The microwave matching of the source to the laser head is more difficult than for the RF matching, due to distributed-circuit considerations.

2. Homogeneity - The discharge field is not inherently longitudinally homogeneous, as in the long-wavelength RF excitation.

Both of these difficulties demand a careful microwave design. A design method for slab lasers longitudinally-homogeneous discharge-formation was not published. The device presented in this thesis offers the characteristics of a simple method for longitudinally-homogeneous microwave-discharge formation in a slab laser with a uniform cross-section. The method, supported by analytical and numerical mathematical models, will be described in succeeding chapters together with experimental verifications.

The electrode space-charge sheaths, serve as a discharge stabilizing agent for the RF discharges. The narrowing of the sheaths makes them inappropriate for stabilization of laser thermal-instabilities. Therefore, every microwave-excited slab configuration contains the means to stabilize the discharge in the form of dielectric slab or slabs attached to one of the electrodes or both. These dielectric slabs replace the RF electrode-sheaths. Nevertheless, they are characterized by a low heat conductance, limiting the heat flow from the discharge to the cooled electrodes. Two opposing demands arise from the use of the dielectric slabs: a thick slab is required for better suppression of thermal instabilities, and a minimal thickness of the slab is required for efficient heat removal from the discharge volume. The existing literature does not present an optimization design tool regarding these two requirements.

The next chapter introduces the subject of high-frequency laser instabilities, and in particular presents an optimization method for dielectric slabs overcoming thermal-instabilities in pulsed microwave-excited CO₂ slab-lasers.

3. Thermal-Instability Considerations for Pulsed Microwave-Excited CO₂ Slab-Lasers

The previous chapter outlined the advantages of using a microwave-excited slab-configured CO₂ laser, considering the inherent operation-limitations of DC and RF laser-excitations. Nevertheless, thermal instabilities in microwave discharges are constraining the efficient operation of these devices. In this chapter [69], the design of a microwave-excited CO₂ slab-laser is optimized, regarding the development of thermal instabilities. A simple discharge model is used to find an optimal dielectric-strip loading, for the prevention of thermal-instabilities development.

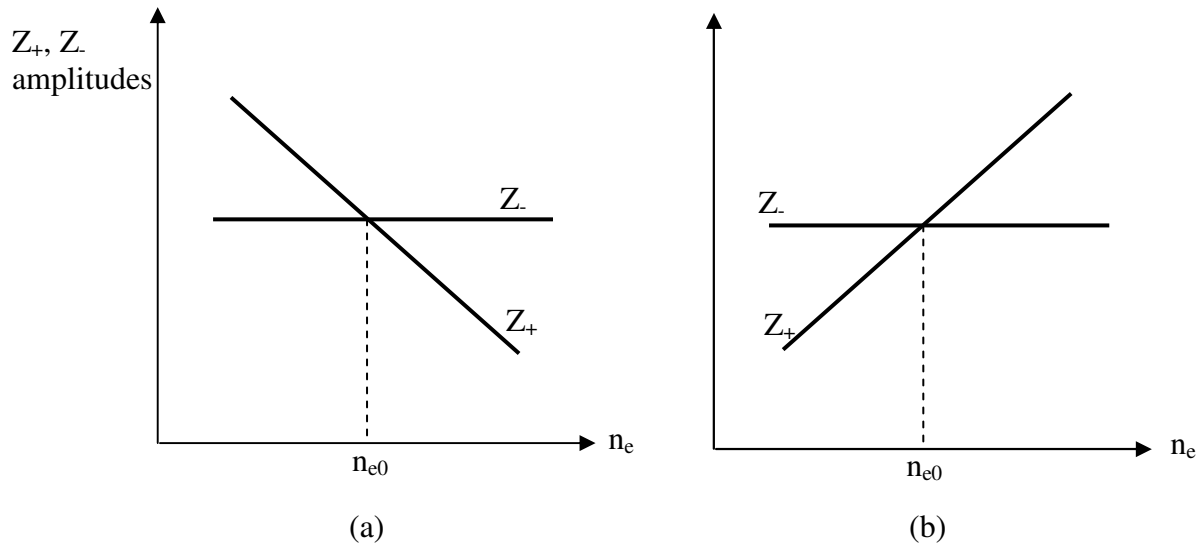
The energy of the electrons in a glow discharge positive-column makes it appropriate for CO₂ laser excitation. The effectiveness of the excitation, however, is determined by the discharge reduced-field. These two parameters, namely, the electron energy and the reduced field, are interconnected through the gas and electron temperatures and densities. Thus, a change in one of these parameters will directly affect the laser performance. A homogeneous positive-column is therefore essential for an efficient operation of a CO₂ laser. The homogeneity of the glow discharge is often impaired at high gas-pressures and high power densities. A perturbation in one of the discharge parameters might grow rapidly, leading to a volumetrically inhomogeneous plasma-state. These states are often observed as striations or current filaments in the gas. In this chapter we concentrate on one of the main discharge instabilities in microwave-excited CO₂ lasers, namely, the thermal instability.

3.1. Discharge Instability Characterization

Instabilities in plasma discharges are often interconnected with processes dominating the density of free electrons in the discharge. A symbolic rate equation for the discharge electron-density (n_e) is

$$\frac{dn_e}{dt} = Z_+ - Z_- \quad (29)$$

where, Z_+ and Z_- denote processes enhancing and depleting the electron density, respectively, as outlined in the previous chapter. The relation between Z_+ , Z_- , and n_e therefore determines the nature of the steady-state condition. Figs. 3.1a, and 3.1b depict two optional cases for the dependence of the electron density on Z_+ and Z_- . In Fig. 3.1a, Z_- (electron depleting processes) is constant for changes in n_e , while Z_+ (electron enhancing processes) decreases for a rise in n_e . This figure demonstrates the dynamics of a stable discharge. A positive perturbation in n_e ($n_e > n_{e0}$) is followed by a decrease in the production of electrons, which in turn, decreases the electron density. Fig. 3.1b shows the opposite situation in which Z_+ increases for a positive rise of n_e . In this situation, a slight increase of the electron density, with respect to the steady state, will further grow reaching saturation.



Figs. 3.1: The discharge electron density versus the processes enhancing and depleting electrons, for a stable (a) and unstable (b) cases.

The instability type is determined according to the perturbation development direction, relative to the electric-field polarization. A perturbation developing along the electric-field lines (like TEA-lasers arcs) is termed longitudinal-instability. It is characterized by a large electron-density, low electron-temperature, and a high gas-temperature. In a transverse instability, the perturbation develops perpendicularly to the electric-field lines. It is characterized by discharge constrictions, and by current filaments with large current densities and high electron temperatures.

One method of canceling a longitudinal instability in TEA lasers is by a minor ionization of the gas before the discharge pulse. Thus, the maximal electric field needed to sustain the discharge is lower, and the temporal electron-density gradient is low enough to prevent the development of the instability. In pulsed slab-lasers, longitudinal instabilities develop only at considerably large power densities, far beyond what is customary for efficient operation. The thermal transverse-instability, however, is one of the main microwave-excitation disadvantages.

In the next section we present in detail the subject of thermal instabilities in microwave-excited CO₂ slab-lasers. By using a simple discharge model, we present a method of optimizing the laser design regarding thermal instabilities.

3.2. Thermal Instabilities

An important mechanism that deteriorates the uniformity of low-pressure laser discharges is the thermal instability, which causes changes in the gas composition. It increases the electron temperature from the optimal for efficient excitation, causes local gas overheating, and discharge constriction. Pioneering works on thermal instabilities in diffusive DC-discharges by Hass [45] and Ecker *et al.* [46] were followed by works of Raizer and Shapiro [51], and Kuteev and Smirnov [66], who studied the different instability criteria for DC and radio frequency discharges.

The influence of the excitation frequency on the evolution of thermal instabilities in diffusive CO₂-laser gas-discharges was investigated by Wester [59]. Yet, the influence of negative ions and the stabilizing effect of the capacitive ion sheaths near the electrodes [47], were not considered [50]. Works of Myshenkov and Yatsenco [53], and Kolesnychenko *et al.* [67], succeeded by Wester *et al.* [68], demonstrated that the thermal-instability threshold depends on macro structural characteristics such as the electrodes formation, and the use of dielectric materials in the discharge region. Vitruk *et al.* [60] demonstrated the stabilizing effect of ion sheaths in medium-pressure attachment-dominated α RF-discharges. This work shows that the α - γ transition voltage can be significantly raised by increasing the excitation frequency. Nevertheless, the ion depletion-sheaths narrowing at high discharge frequencies, limits the pressure range and the power-density that can be deposited in the plasma, due to thermal instabilities. However, in a later work, Vitruk *et al.* [61]

showed that by maintaining the scale factor fd constant (f and d are the RF frequency and the electrode gap, respectively), the discharge characteristics do not change for a constant reduced field (E/N). The inter-electrode gap reduction in microwave discharges is beneficial for slab lasers, due to the enhanced heat flow rate to the enclosing walls, as discussed in the previous chapter.

In several works [29,30] demonstrating the microwave-excitation capabilities of CO₂ slab-lasers, the stability degradation, due to the ballast ion-sheaths narrowing in the microwave-excited plasma, was reduced by placing a dielectric ballast-strip in series with the plasma column. Using a ballast dielectric-strip at high repetition-rate microwave pulses (10 - 40 kHz) enabled a quasi-CW laser operation at low pressures (~10 kPa). However, a small heat conductivity of the gas ballast strip compared with that of the metal electrodes, obstructed the heat flow to the enclosing walls. The gas overheating, as a consequence, expresses one of the principal disadvantages of the microwave excitation regime. Moreover, in high-pressure microwave-discharges, the positive-column is often thermally unstable, even in the presence of a dielectric ballast strip. This instability initiates current filaments, in which both the ionization degree and the gas-temperature increase significantly, as compared to commonly used laser glow-discharge parameters.

In the following sections we present the dependence of the thermal-instability formation-time on the microwave-discharges parameters. These include the gas pressure, the reduced field (E/N), the electron density, the discharge width, and the ballast dielectric-strip characteristics. Two types of gas mixtures are considered in this analysis:

Type 1: CO₂:N₂:He = 1:2:3.

Type 2: CO₂:N₂:He = 1:1:8.

Since our aim is to optimize the heat dissipation rate, in the presence of a dielectric-strip, the thinnest ballast-strip is required. This goal is attained by equating the plasma instability evolution time to the time required for reaching the maximal gas temperature for efficient laser performance.

Our work [69] formulates the optimal dependence of the ballast-strip capacitance on the reduced field. We derive the plasma thermal-instability evolution-time, and the optimal dielectric-slab required for suppressing the instability, ensuring a minimal obstruction of the discharge heat flow. This has a considerable technological significance for pulsed microwave-excited CO₂ slab-lasers.

3.2.1. Discharge Model

The microwave-excited discharge in a typical CO₂ slab-laser occurs between two ridge electrodes at the middle of a microwave waveguide, where the electric field is the strongest (see Fig. 3.2). At the ridge section, the electric field is polarized in the y-axis direction, perpendicular to the dielectric slab. The dielectric slab is attached to one of the metal electrodes or to both of them. The structure presented in Fig. 3.2 is used in our analysis. We assume a uniform electric field profile across the double-ridge section.

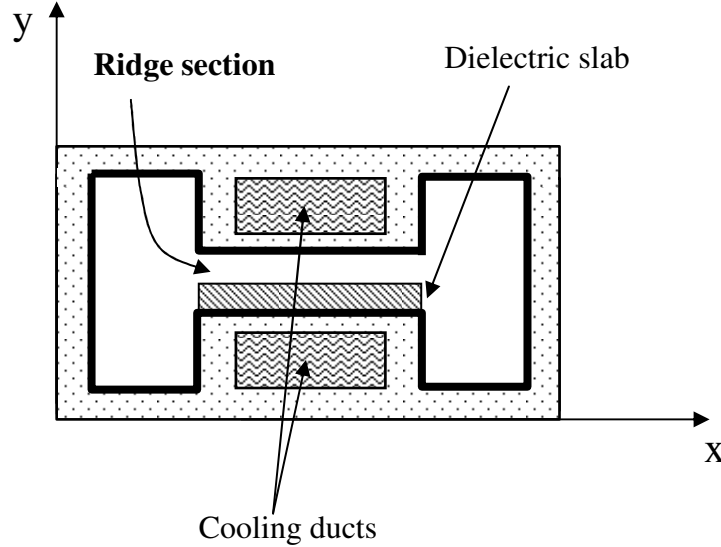


Fig. 3.2: A typical double ridge waveguide used in microwave-excited CO₂ slab-lasers.

The main discharge processes determine electron and ion densities. Assuming a quasi-neutral plasma, free electrons are generated mainly by ionization and negative ion detachment processes, and are lost mostly by attachment and electron-ion recombination processes. The electrode spacing is in the order of a few millimeters, so, the ambipolar diffusion is negligible compared to other bulk electron-loss

mechanisms. Considering these main discharge-processes, the rate equations for electron and negative-ion densities [47] are

$$\frac{\partial n_e}{\partial t} = k_i \left(\frac{E}{N} \right) N n_e - k_a \left(\frac{E}{N} \right) N n_e + k_d N n_- - \beta_e n_e n_+ \quad (30a)$$

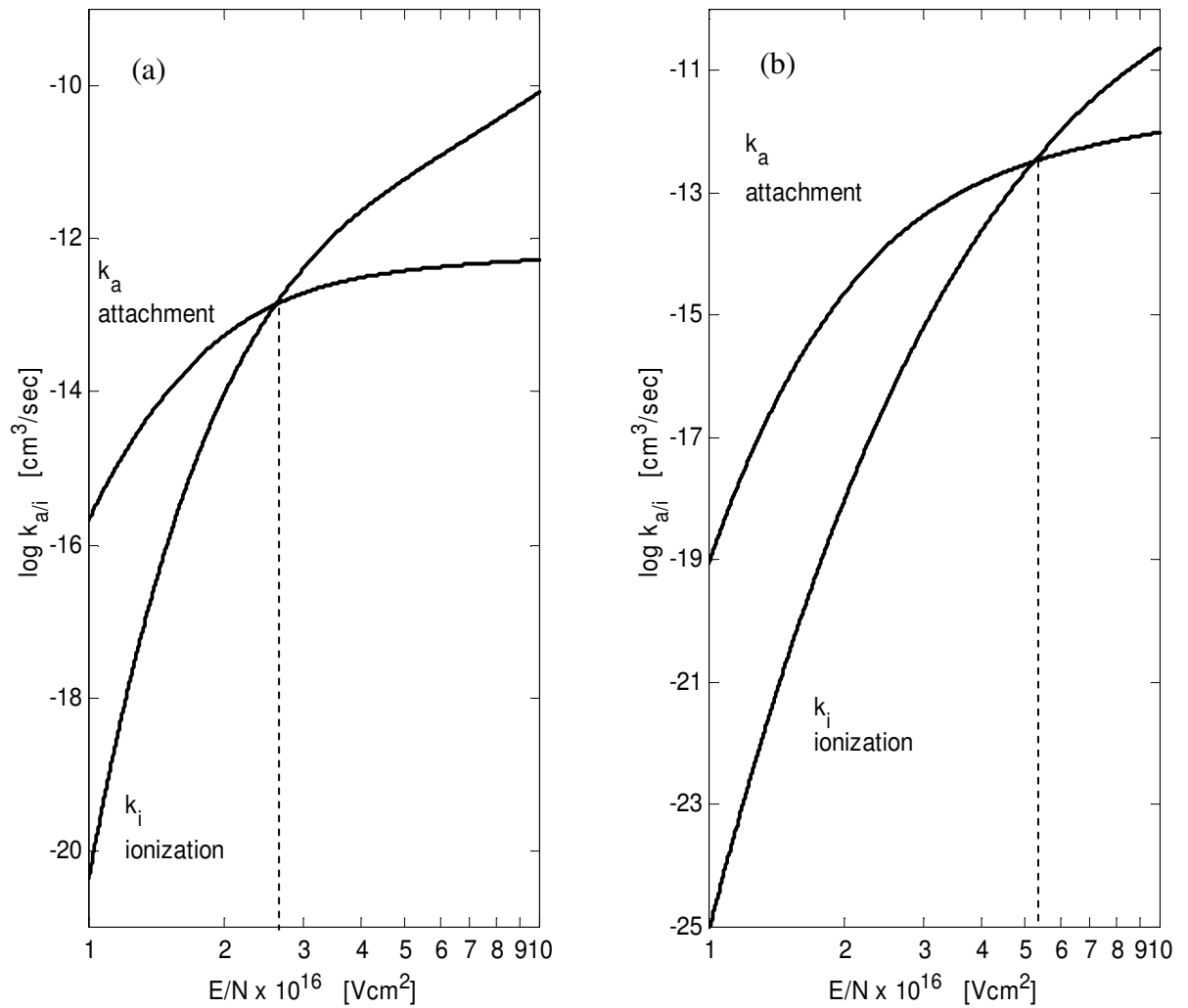


Fig. 3.3: The dependence of the ionization and attachment rate coefficients on the reduced field (E/N) in; (a) a rich helium mixture ($\text{CO}_2:\text{N}_2:\text{He} = 1:1:8$), and; (b) a poor helium mixture ($\text{CO}_2:\text{N}_2:\text{He} = 1:2:3$).

$$\frac{\partial n_-}{\partial t} = k_a \left(\frac{E}{N} \right) N n_e - k_d N n_- - \beta_- n_- n_+, \quad (30b)$$

where the positive ion density n_+ , is derivable by the electroneutrality condition

$$n_+ = n_e + n_- . \quad (30c)$$

n_e , n_- , and n_+ are the densities of the electrons, negative ions, and positive ions, respectively, k_i , k_a and k_d are the rate coefficients of the ionization, attachment, and detachment processes, respectively. N is the gas density, E is the electric field amplitude, and E/N is termed the reduced field. β_e and β_- are the electron-ion and ion-ion recombination coefficients, respectively. The dependence of k_i and k_a on the reduced field, for rich and poor helium mixtures, is illustrated in Figs. 3.3a, and 3.3b, respectively [71]. The factor k_d , was found by Raizer [47,51] as $k_d = 1.12 \cdot 10^{-14} \text{ cm}^3/\text{s}$, and $k_d = 4.5 \cdot 10^{-15} \text{ cm}^3/\text{s}$, for poor and rich helium mixtures, respectively (where k_d is independent of E/N). Approximate values for the recombination coefficients obtained by Lowke *et al.* [71], are $\beta_- \cong \beta_e \cong 10^{-7} \text{ cm}^3/\text{s} \equiv \beta$.

In steady-state conditions (i.e. $\frac{\partial}{\partial t} = 0$), the dependence of the normalized electron and negative-ion densities, \bar{n}_e , \bar{n}_- on the reduced field can be derived from (30a,b,c) as

$$\bar{n}_e \left(\frac{E}{N} \right) = \frac{n_e}{N} = \frac{1}{4k_i\beta} (A+B)^2 \quad (31a)$$

$$\bar{n}_- \left(\frac{E}{N} \right) = \frac{n_-}{N} = \frac{1}{2\beta} \left[A+B - \frac{1}{2k_i} (A+B)^2 \right] \quad (31b)$$

where

$$A = k_i - k_d - k_a \quad (31c)$$

$$B = \sqrt{A^2 + 4k_i k_d} . \quad (31d)$$

k_i and k_a in Eqs. (31a-d) depend on the reduced field as discussed above.

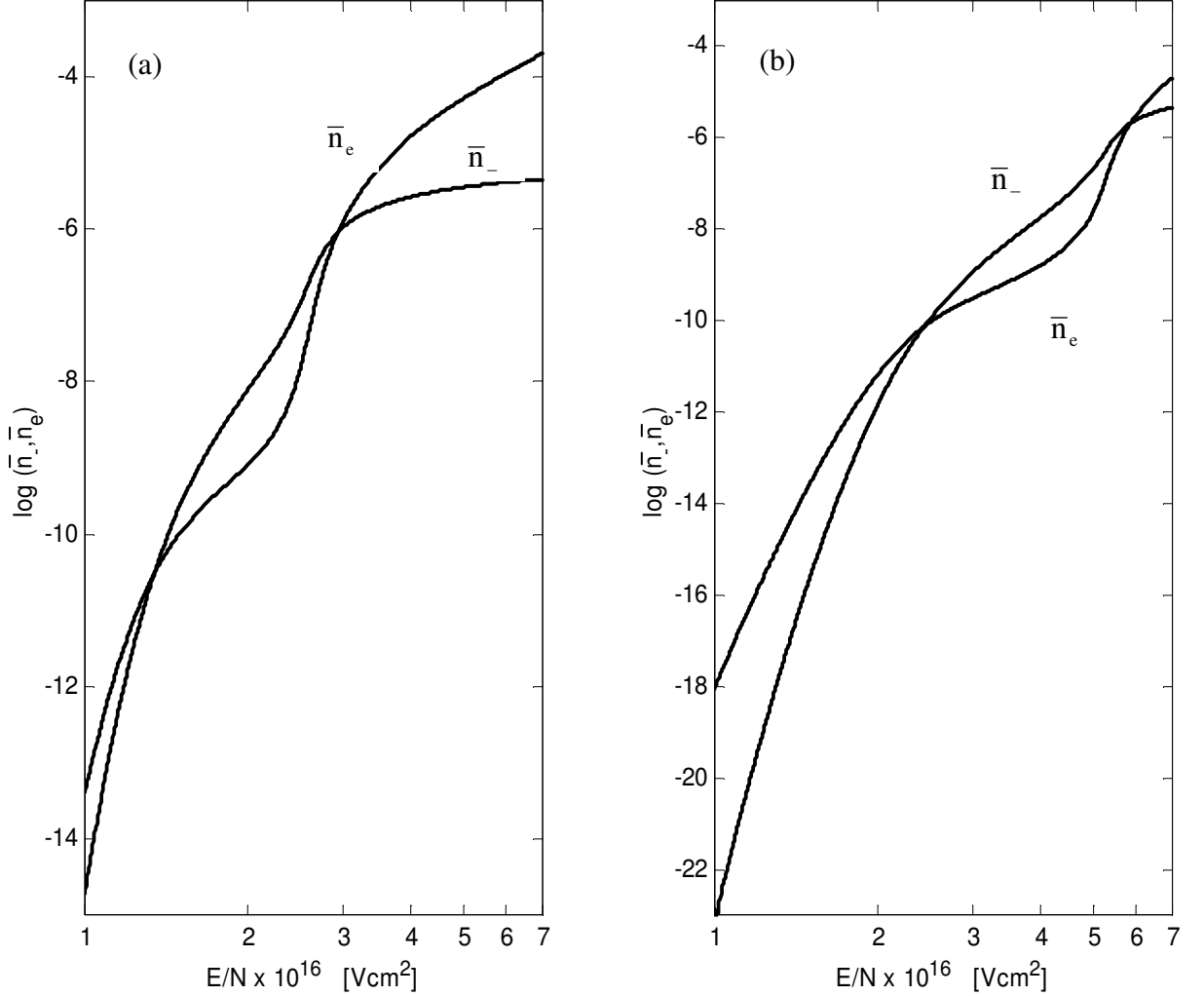


Fig. 3.4: Normalized steady-state electron and negative-ion densities (\bar{n}_e, \bar{n}_-) results of Eqs. (31a,b), with respect to the reduced field (E/N) for; (a) a rich helium mixture ($\text{CO}_2:\text{N}_2:\text{He} = 1:1:8$), and; (b) a poor helium mixture ($\text{CO}_2:\text{N}_2:\text{He} = 1:2:3$).

The dependence of the electron and negative ion normalized densities on the reduced field (Eqs. (31a-d)), for rich and poor helium mixtures, is shown in Figs. 3.4a and 3.4b, respectively. It is noted that the negative ions affect the discharge characteristics when $E/N \leq (E/N)_{i=a}$, where $(E/N)_{i=a}$ is the reduced field in which the ionization and attachment rates are equal [50]. This is typical for weakly ionized electronegative gas discharges, in which bulk processes, involving negative ions,

determine the electron density and the mixture conductivity. At high reduced-fields, the recombination processes counter the high production-rate of electrons, due to the large ionization coefficient, as shown in Figs. 3.3a, b.

The plasma conductivity $\sigma(\omega)$ and its relative dielectric constant $\varepsilon_p(\omega)$ are given by [47]

$$\sigma(\omega) = \frac{2\pi e^2 n_e \omega_c}{m_e (\omega^2 + \omega_c^2)} \quad (32a)$$

$$\varepsilon_p(\omega) = 1 - \frac{\omega_p^2}{\omega^2 + \omega_c^2} + i \frac{\omega_c}{\omega} \frac{\omega_p^2}{(\omega^2 + \omega_c^2)} = 1 - \frac{\omega_p^2}{\omega(\omega + i\omega_c)} \quad (32b)$$

where ω_c is the collision angular frequency, ω and $\omega_p = \sqrt{e^2 n_e / \varepsilon_0 m_e}$ are the angular frequencies of the RF excitation and of the plasma, respectively.

When the RF excitation frequency is of the same order as the plasma frequency, but much smaller than the collision frequency (i.e., $\omega_p \approx \omega \ll \omega_c$), the plasma conductivity and dielectric constants become

$$\sigma \cong \frac{e^2 n_e}{m_e \nu_c} \quad (33a)$$

$$\varepsilon_p(\omega) \cong 1 - \frac{\omega_p^2}{\omega_c^2}, \quad (33b)$$

where ν_c is the collision frequency. For example, the plasma and collision frequencies for a rich helium-mixture optimal reduced field ($E/N \cong 2.5 \cdot 10^{16} \text{ Vcm}^2$) at a pressure of 100 Torr are ~ 5 and 230 GHz, respectively. A common microwave excitation source operates at a frequency of 2.45 GHz.

In the next sections we describe the mechanism for thermal-instability evolvment, and find an optimized dielectric-strip thickness in a microwave-excited CO₂ slab-laser.

3.2.2. Evolvement of Thermal Instabilities

Deviations from homogeneity that take place at high pressures and currents in plasma discharges are mainly attributed to thermal instabilities. The following chain of events can initiate a thermal instability [47]

$$\delta n_e \uparrow \rightarrow \delta(jE) \uparrow \rightarrow \delta T \uparrow \rightarrow \delta N \downarrow \rightarrow \delta(E/N) \uparrow \rightarrow \delta T_e \uparrow \rightarrow \delta n_e \uparrow. \quad (34)$$

Here, jE is the Joule heat power-density, T and T_e are the gas and electron temperatures, respectively. The upward and downward arrows denote an increase and a decrease of a parameter, respectively.

It is difficult to follow the exact evolvement of the thermal instability. Therefore, an exponential-growth of the perturbation is assumed near the instability threshold (i.e., $\exp(\Omega t)$, where Ω is positive for an unrestrained instability growth). The unrestrained-instability characteristic evolution time is $\tau = \Omega^{-1}$. Our goal in the following sections is to evaluate τ for microwave-excited slab CO₂-lasers employing a ballast dielectric-strip. An optimal dielectric strip thickness will be derived for different gas mixtures and reduced fields.

The heat balance equation in this discharge model, assuming a linear temperature change in the discharge gap, yields

$$\frac{dQ}{dt} = NC_p \frac{dT}{dt} = \sigma E^2 - NC_p (T - T_0) v_{hf} \quad (35a)$$

where Q is the heat energy density, C_p is the gas specific-heat at a constant pressure per unit particle, σE^2 is the microwave power density coupled to the discharge, and T_0 is the enclosing wall temperature. The rate of heat-removal to the enclosing walls due to heat conduction is

$$v_{hf} = \frac{\kappa}{NC_p (\Lambda / \pi)^2} = \frac{\pi^2 \kappa}{NC_p \Lambda^2} \quad (35b)$$

where κ is the gas heat-conduction constant. An effective gap thickness Λ (Fig. 3.2) represents an equivalent discharge width, free from a dielectric material. It is affected by the presence of the dielectric slab and given by

$$\Lambda = \frac{d_p (d/\kappa + d_b/\kappa_b)}{2(d/\kappa + d_b/2\kappa_b)} \quad (35c)$$

as derived in the next subsection. d_b and κ_b are the dielectric-slab thickness, and heat-conduction constant, respectively. d_p and d are the discharge width and the total width respectively.

Since the rate of heat-removal is inversely proportional to the effective gap thickness squared ($v_{hf} \propto 1/\Lambda^2$), our goal is to reduce Λ as much as possible. This is done by finding (for a given dielectric-strip) the minimal slab-thickness required for a stable discharge.

3.2.2.1. Effective Gap Thickness for Heat Flow in the Presence of a Dielectric Strip

When a ballast dielectric-strip is introduced in series with the plasma column, it obstructs the heat flow from the discharge region to the cooled electrodes. This is due to a low heat-conduction of the dielectric-strip compared with the metal electrodes. In a microwave-discharge excited CO_2 slab-laser, a dielectric strip is attached to one of the metal electrodes or both, enabling a heat flow from it to the water-cooled electrode. Fig. 3.5 illustrates a cross section of a slab configuration including a ballast dielectric-strip. T_0 is the cooled electrode temperature. T_1 is the maximal gas temperature at a point located Λ away from the bare electrode. The heat flow-rates from this point in both directions are equal. T_2 is the dielectric strip temperature at the interface with the gas. d_p is the discharge width, and d_b is the dielectric strip thickness. We find the effective slab thickness, Λ , with respect to the original discharge width and the dielectric strip characteristics.

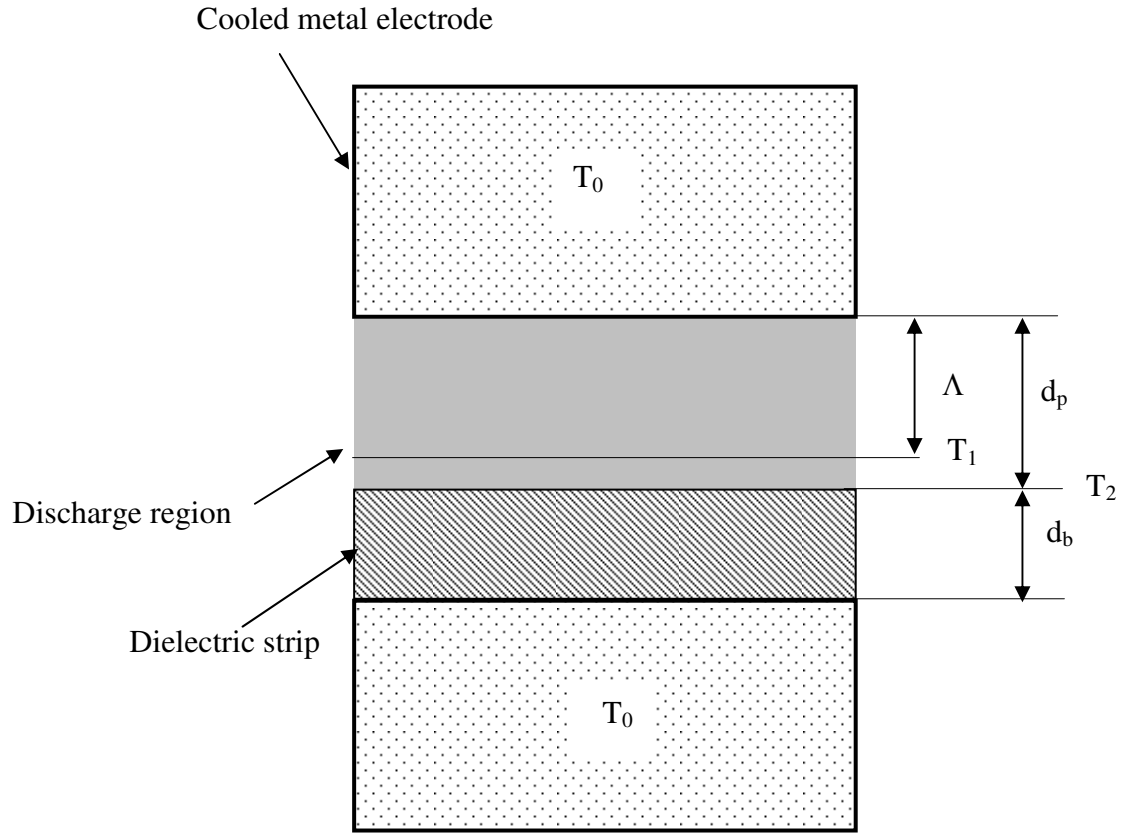


Fig. 3.5: A CO₂ slab-laser cross-section including a dielectric ballast-strip.

When the discharge-pulse ends, the equations relating the different parameters, for a linear temperature-variation approximation between the slab surfaces, are

$$NC_p \frac{\partial T_1}{\partial t} = -\kappa \frac{T_1 - T_2}{(2d_p - \Lambda)^2} \pi^2 \quad (36a)$$

$$NC_p \frac{\partial T_1}{\partial t} = -\kappa \frac{T_1 - T_0}{\Lambda^2} \pi^2 \quad (36b)$$

$$\kappa \frac{T_1 - T_2}{(d_p - \Lambda/2)} = \kappa_b \frac{T_2 - T_0}{d_b}. \quad (36c)$$

C_p is the unit particle specific-heat at a constant gas pressure. κ and κ_b are the gas and dielectric-strip heat-conduction constants, respectively. N is the gas density. Eqs. (36a) and (36b) represent the heat balance of the gas at the regions bound by temperatures T_1 and T_2 , and by temperatures T_1 and T_0 , respectively. Eq. (36c) expresses the rate of heat flow from T_1 to T_2 , and from T_2 to the metal electrode. The time dependant temperatures, T_1 and T_2 are derived from (36a) and (36b) as

$$T_1(t) = [T_1(t=0) - T_0] \exp\left(-\frac{\kappa \pi^2 t}{C_p (2\Lambda)^2}\right) + T_0 \quad (37a)$$

$$T_2(t) = [T_1(t=0) - T_0] \exp\left(-\frac{\kappa \pi^2 t}{C_p (2\Lambda)^2}\right) \cdot \left(1 - \frac{(d_p - \Lambda)^2}{\Lambda^2}\right) + T_0. \quad (37b)$$

Λ is found by substituting Eqs. (37a, b) into Eq. (36c) as

$$\Lambda = \frac{d_p (d/\kappa + d_b/\kappa_b)}{2(d/\kappa + d_b/2\kappa_b)} \quad (\text{as presented in Eq. (35c)}),$$

and is termed – the effective gap width in the presence of a dielectric slab.

3.2.3. Free Evolution of Thermal Instabilities

When an initial thermal perturbation (δT^0) occurs, the temperature (T) in Eq. (35a) is expressed by $T + \delta T$, where the perturbation growth is exponential ($\delta T = \delta T^0 \exp(\Omega t)$). When the ballast strip is excluded, the instability growth rate derived from the perturbed heat balance equation (35a) [47, 60] is

$$\Omega = v_t^0 (\hat{v}_t + 1) - v_{hf}, \quad (38a)$$

where v_t^0 is the ratio between the heating rate and the heat energy stored in the gas given by

$$v_t^0 = \frac{\sigma E^2}{N C_p T_0}. \quad (38b)$$

\hat{v}_t represents the change in the normalized electron density due to variations in the reduced field, and is expressed by

$$\hat{v}_t = \frac{d(\ln(\bar{n}_e))}{d(\ln(E/N))}. \quad (38c)$$

The single-particle specific-heat and heat conduction constants are $C_p = 2.7k_b$ and

$\kappa = 1.3 \cdot 10^{-3} \frac{\text{Joule}}{\text{cm sec}^\circ \text{K}}$, respectively, for a rich helium mixture, and $C_p = 3k_b$, and

$\kappa = 9 \cdot 10^{-4} \frac{\text{Joule}}{\text{cm} \cdot \text{sec}^\circ \text{K}}$ for the poor helium mixture, where k_b is the Boltzmann

constant. The heat removal (v_{hf}) stabilizes the discharge as long as the instability growth rate (Ω) is negative ($v_t^0 (\hat{v}_t + 1) \leq v_{hf}$). When $v_t^0 (\hat{v}_t + 1) \gg v_{hf}$, the growth rate of the instability is approximately given by $\Omega \cong v_t^0 (\hat{v}_t + 1)$. Assuming that the electron distribution stabilization rate is much higher than Ω , the normalized change in the electron density with the reduced field (\hat{v}_t) is given by Eq. (31a). The

dependence of \hat{v}_t on the reduced field is illustrated in Fig. 3.6 for rich and poor helium mixtures.

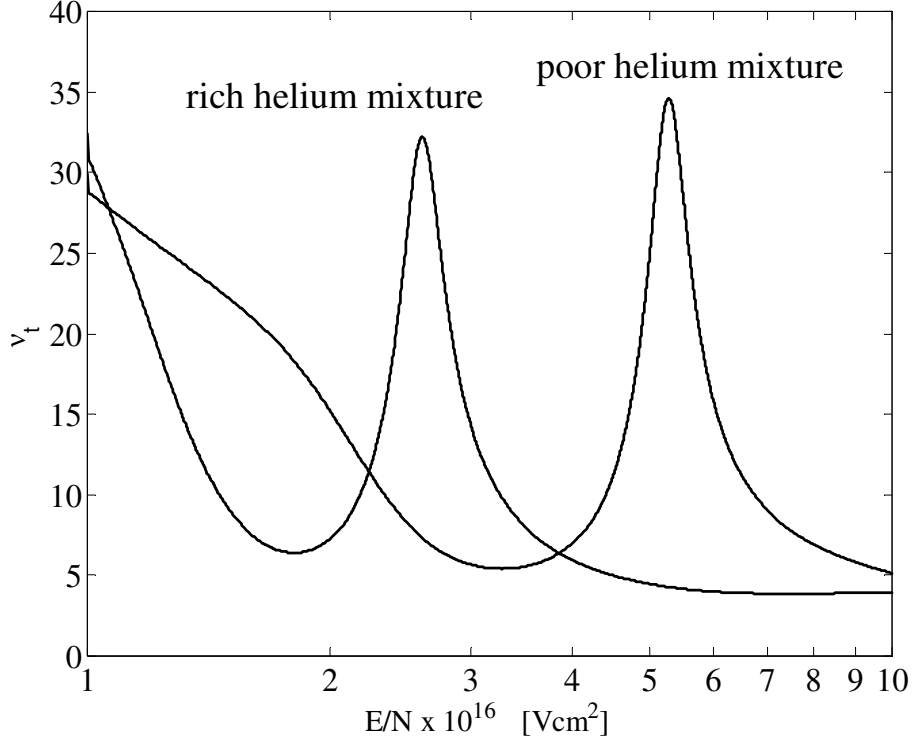


Fig. 3.6: The dependence of the normalized variation in the electron-density (\hat{v}_t) on the reduced field (Eq. (38c)) for rich ($\text{CO}_2:\text{N}_2:\text{He} = 1:1:8$) and poor ($\text{CO}_2:\text{N}_2:\text{He} = 1:2:3$) helium mixtures.

By solving Eq. (38a), the thermal instability growth-rate (Ω) is derived as a function of the reduced field. Figs. 3.7a and 3.7b illustrate Ω for several currently used gas pressures in slab-lasers for rich and poor helium mixtures. The calculation is performed for a gas temperature (T) of 400°K, and a plasma width (d_p) of 1.5 mm. The thermal instability growth-rate variation due to the pressure increase (when $E/N=(E/N)_{i=a}$) is $\sim 6 \cdot 10^3 \text{ kPa}^{-1}\text{s}^{-1}$ for the rich helium mixture, and $\sim 4 \cdot 10^7 \text{ kPa}^{-1}\text{s}^{-1}$ for the poor helium mixture.

A thermal instability analysis of a discharge in the presence of a dielectric slab is given in the next section.

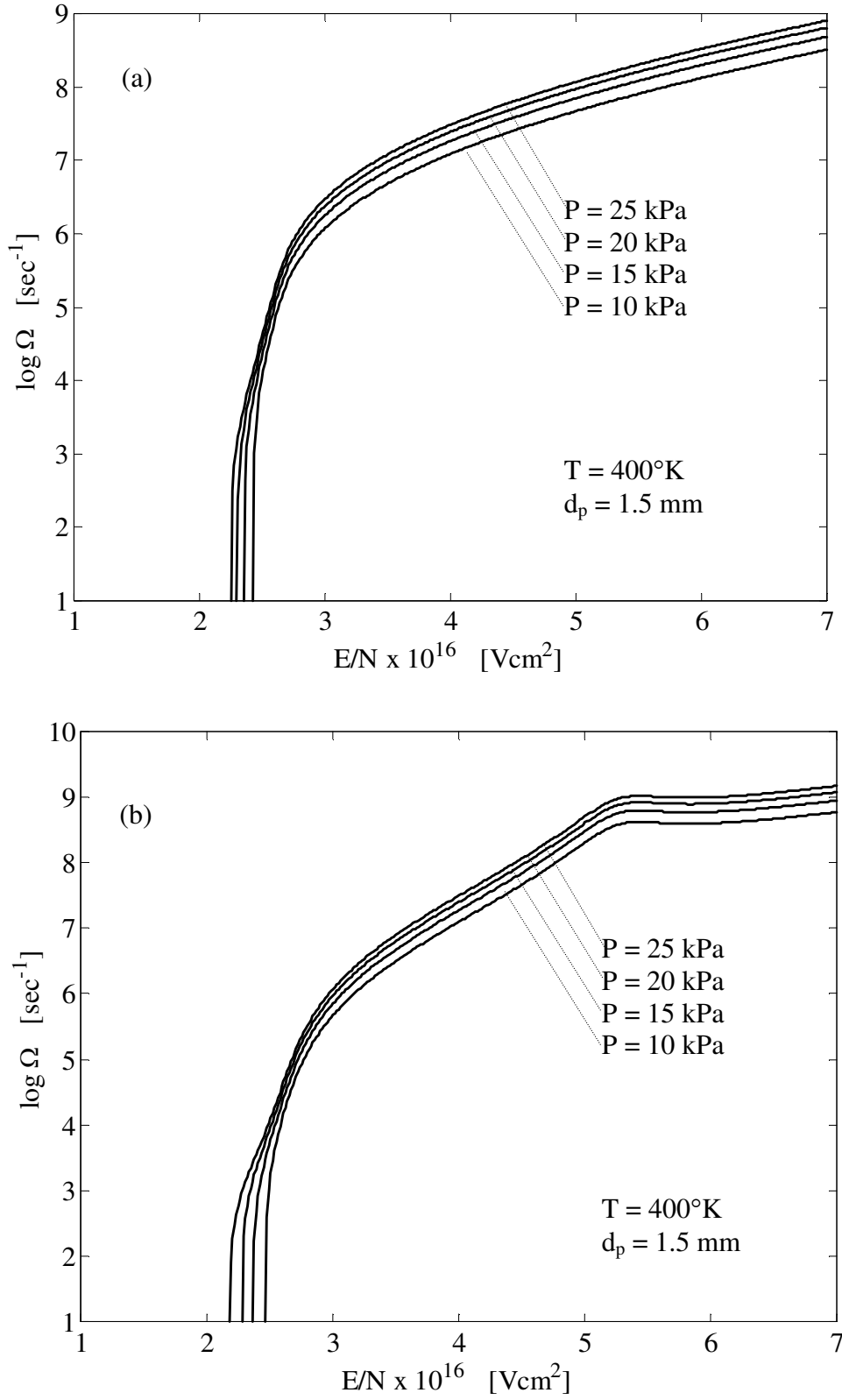


Fig. 3.7: The thermal instability growth-rate vs. the reduced field in various gas pressures for; (a) a rich helium mixture ($\text{CO}_2:\text{N}_2:\text{He} = 1:1:8$), and; (b) a poor helium mixture ($\text{CO}_2:\text{N}_2:\text{He} = 1:2:3$). In both cases $T = 400^\circ\text{K}$, $d_p = 1.5$ mm, and the ballast strip is excluded.

3.2.4. Evolution of Thermal Instabilities in the Presence of a Ballast Dielectric-Strip

A microwave-excited plasma column, characterized by a negative voltage-current relation [60], can be stabilized by placing in series a dielectric strip. Increasing the thickness of the dielectric strip reduces its capacitance and therefore, enlarges its impedance. Consequently, the plasma becomes more stable. However, the dielectric strip obstructs the heat flow from the gas to the enclosing walls. Therefore, it is necessary to find the thinnest dielectric strip for sustaining a stable discharge. The gas ignition temperature is 300°K, but it should not exceed 500°K at the end of the pulse ($\Delta T = 200^\circ\text{K}$). Above this temperature, the laser efficiency is markedly decreased due to a poor gain coefficient. This is due to a thermal population of the lower laser level, a gain profile broadening, and an increasing number of populated sub rotational levels, as discussed in Section 1.2.3. Moreover, The upper laser level quenching-rate at 500°K is twice as high than in 300°K [12]. This stringent demand on the gas temperature in conjunction with the heating rate expression (Eq. (38b)) dictates a limit for the maximal pulse-duration of

$$t_p = \left(\frac{NC_p \Delta T}{\sigma E^2} \right). \quad (39)$$

In this derivation (Eq. (39)), we neglect the heat conduction losses during the discharge pulse. An efficient laser operation will be reached when the instability growth rate does not exceed t_p .

Fig. 3.8 illustrates a simplified equivalent circuit for the discharge region, including a dielectric slab, which compensates for the negligible effect of the ion depletion-layers in a microwave discharge. C_{pl} and C_d are the plasma-region capacitance, and the ballast-strip capacitance, respectively. R_p is the discharge resistivity. The total current passing through the system, J , equals the sum of the conduction and displacement currents, J_1 and J_d respectively. V_p and V_d are the plasma and dielectric-slab voltages, respectively, and V_s is the total voltage. When the

plasma capacitive-currents are ignored, these voltages satisfy the following relation

$$|V_s|^2 = |V_p|^2 + |V_d|^2. \quad (40)$$

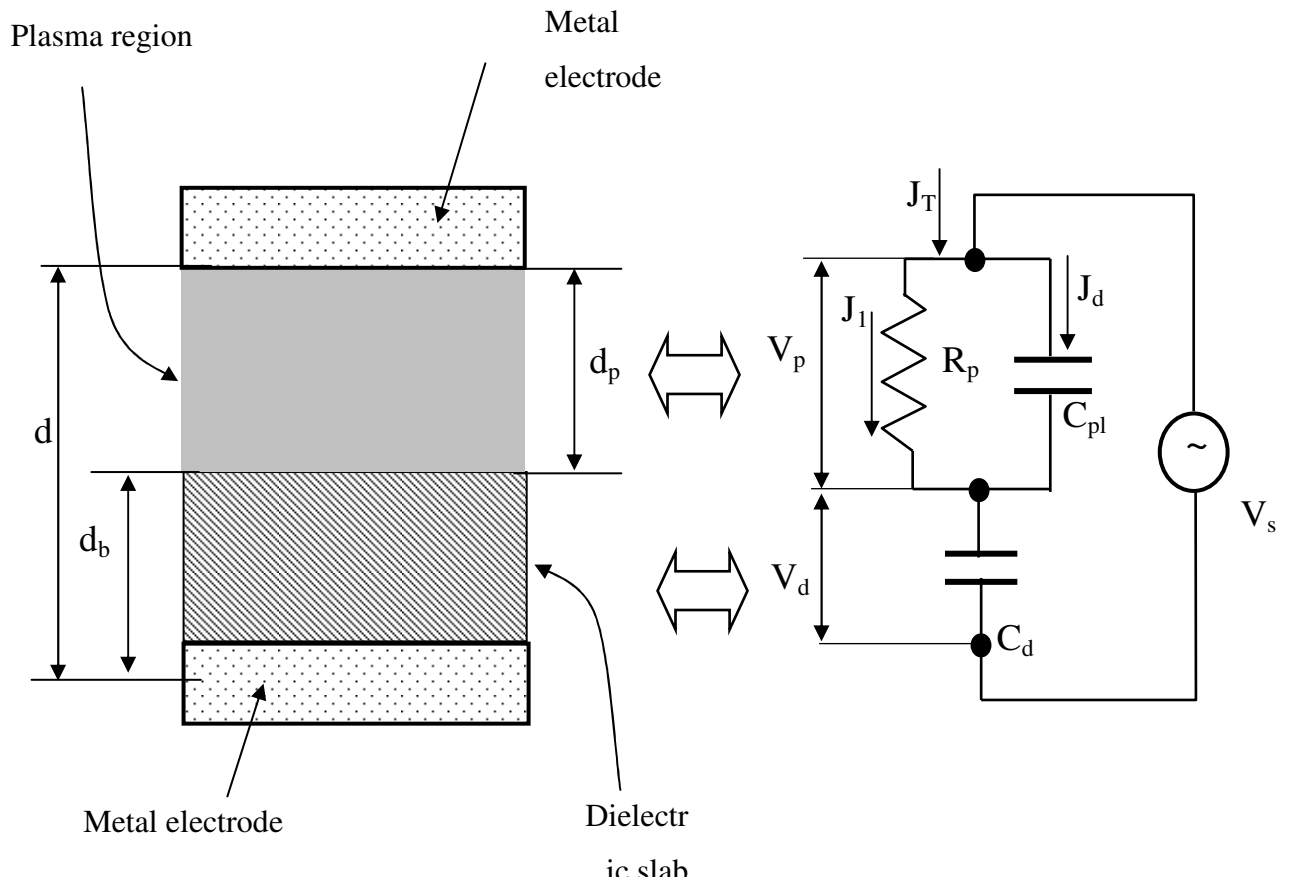


Fig. 3.8: An equivalent circuit for a discharge plasma-region including a ballast dielectric-strip.

Vitruk *et al.* [60] have found that the thermal-instability growth rate for RF discharges stabilized by their ion depletion-layers is

$$\Omega = v_t^0 \left(\frac{1 + \eta + \eta \hat{v}_t}{1 + \eta + \hat{v}_t} \right) - v_{hf} \quad (41a)$$

where

$$\eta = \frac{|V_p|^2}{|V_d|^2} \quad (41b)$$

(note that for $V_d = 0$, Eq. (41a) is reduced to Eq. (38a)). Originally [60], V_d and V_p were the voltages across the ion depletion layers and the plasma, respectively. Here, V_d is the voltage drop across the dielectric slab. The relation between the discharge-region voltage V_p , and the dielectric strip voltage V_d is given by

$$\eta = \frac{|V_p|^2}{|V_d|^2} = \frac{C_d^2}{(C_{pl} + C_d)^2 + (\omega R_p)^{-2} - C_d^2} \quad (42a)$$

for

$$C_d = \frac{\epsilon_r \epsilon_0}{d_b} \quad \left[\frac{\text{Farad}}{\text{cm}^2} \right] \quad (42b)$$

$$C_{pl} = \frac{\epsilon_0}{d_p} \quad \left[\frac{\text{Farad}}{\text{cm}^2} \right] \quad (42c)$$

$$R_p = \frac{d_p}{\sigma} \quad [\Omega \text{cm}^2] \quad (42d)$$

where d_b and ϵ_r are the ballast-strip thickness and relative dielectric constant, respectively. ω is the excitation source angular frequency, d_p is the discharge width, and $\epsilon_0 = 8.85 \cdot 10^{-14}$ Farad/cm is the free space dielectric constant (we assume $\epsilon(\omega) \cong 1$ in Eq. (33b)).

In most of the microwave pulsed discharges, the stabilizing effect of the heat removal (v_{hf}) during the discharge pulse is negligible. Nevertheless, the heat

conduction is one of the main gas cooling-mechanisms during the time difference between consecutive discharge pulses in a repetitive mode operation.

Since v_t^0 (in Eq. (41a)) depends on the gas temperature (Eq. (38b)), the instability growth-rate varies during the pulse. The mean instability growth rate (Ω_m) is found as

$$\Omega_m = \frac{\int_{300^\circ \text{K}}^{500^\circ \text{K}} \Omega(T) dT}{200^\circ \text{K}} . \quad (43)$$

By equating Ω_m and t_p^{-1} , where t_p is the efficiency-limited pulse duration, (Eq. (39)), the ratio, $\bar{C}_{d/p}$, between the optimal dielectric-strip capacitance and the plasma capacitance is found as

$$\bar{C}_{d/p} = \frac{C_d}{C_p} = \frac{d_p \epsilon_r}{d_b} \cong \frac{|\epsilon_p|^2}{\sqrt{1 + \frac{\hat{v}_t - 1}{2\hat{v}_t + 1} |\epsilon_p|^2} - 1} \quad (44)$$

where the effective plasma complex-dielectric-constant, $\epsilon_p = 1 + i \frac{\sigma}{\omega \epsilon_0}$ is used, as derived in Eq. (32b).

Due to optical-waveguide laser losses considerations [63-65, 70], the minimal allowed discharge-width in a CO₂ slab-laser is $d_p = 1.5$ mm. For this plasma width, the dependence of the optimal ballast-strip width, d_b , on the reduced field, both for rich and poor helium mixtures can be derived.

The analysis results are illustrated in Fig. 3.9a for a fused Quartz strip ($\epsilon_r = 3.8$), and in Fig. 3.9b for an Alumina strip ($\epsilon_r = 9$).

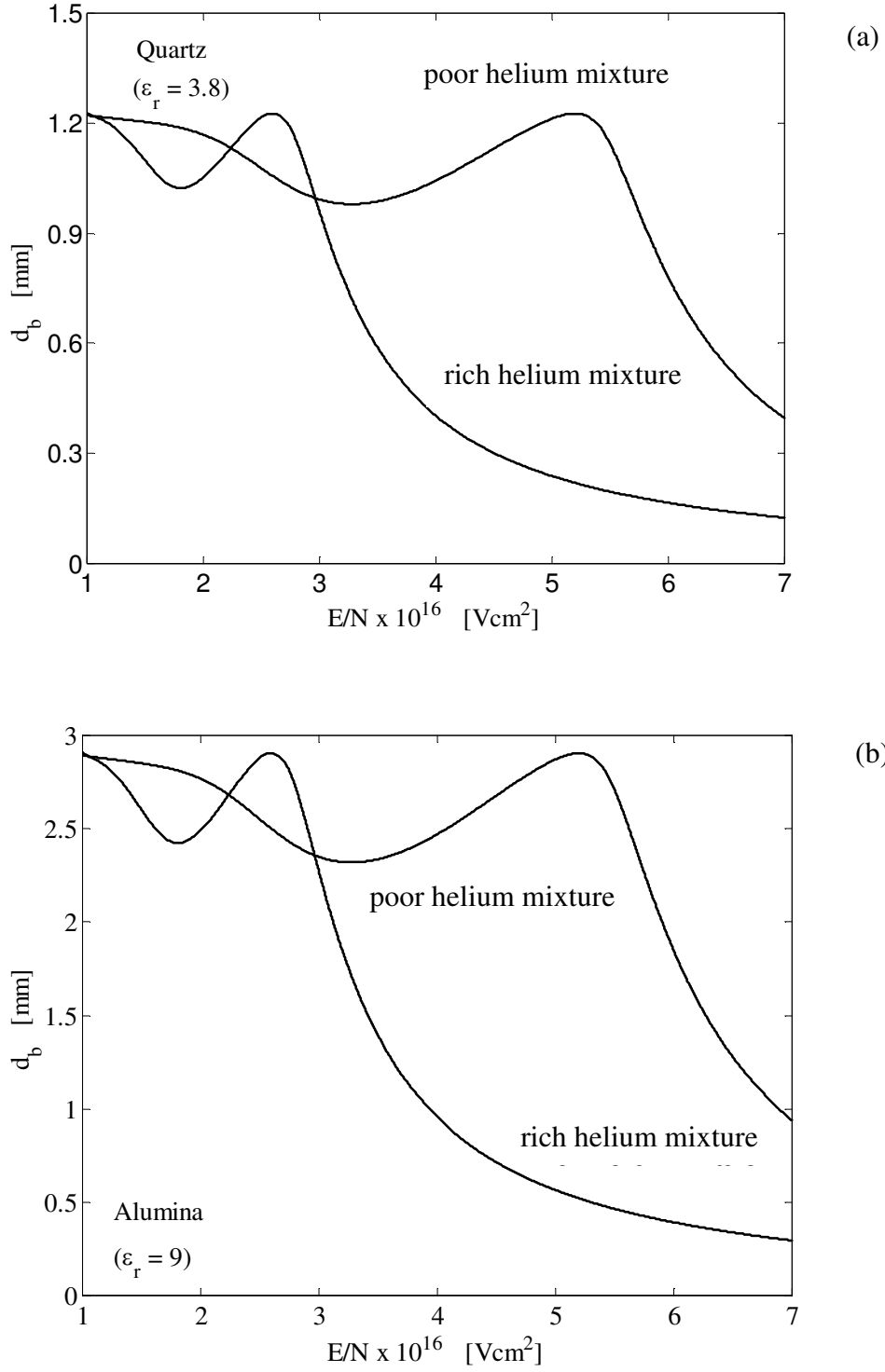


Fig. 3.9: The optimal ballast-strip thickness dependence on the reduced field in both rich and poor helium mixtures for; (a) a fused Quartz strip, and; (b) an Alumina strip.

The plasma width (d_p) is 1.5 mm in both cases.

The minimal dielectric-strip thickness required for pulsed-discharge stabilization is found at a reduced field in which the ionization and attachment rates are equal ($E/N=E/N_{i=a}$), for rich and poor helium mixtures. The normalized capacitance is then approximately given by

$$\overline{C}_{d/p} = \frac{C_d}{C_p} = \frac{d_p \epsilon_r}{d_b} \approx 4.7 . \quad (45)$$

As evident in Figs. 3.9a and 3.9b, it is negligibly dependent on the gas mixture type.

3.2.5. Thermally Optimized Microwave Discharge

A microwave-excited CO₂ slab-laser performance is improved by increasing the gas cooling-rate between discharge pulses, and by minimizing the gas re-heating, due to heat accumulation in the ballast strip during the microwave pulse. This is achieved by introducing the thinnest ballast strip required for a sustained stable discharge. Thus, a maximal cooling rate is found in the last sections for a stable microwave-discharge.

The thermal-instability growth-rate analysis given previously was performed for a microwave-excited CO₂ slab-laser at different reduced-fields and gas pressures, considering two basically different gas mixtures. The stabilizing effect of a dielectric strip placed in series with the plasma column was simulated by using an equivalent circuit for the discharge ridge section (Fig. 3.8). The plasma was assumed to be in steady state conditions.

The thermal instability for both mixtures considered is increased in the attachment-dominated regime ($E/N = (E/N)_{i=a}$), as shown in Fig. 3.6. In this region, the electron normalized-density-variation (\hat{v}_t) gradient is the largest. This maximal increase stems from the change from a negative-ion-dominated discharge to an electron-dominated one. The dependence of \hat{v}_t on the pressure is $\sim 6 \cdot 10^3 \text{ kPa}^{-1} \text{ sec}^{-1}$ and $\sim 4 \cdot 10^7 \text{ kPa}^{-1} \text{ sec}^{-1}$ (Figs. 3.7a, b), for the helium rich and poor mixtures respectively. At all other reduced-fields, the thermal-instability evolution-rates decrease. Therefore, the minimal dielectric strip required to stabilize the discharge is determined in the attachment-dominated region.

The optimized dielectric-strip capacitance value, normalized with respect to the discharge region capacitance, is found to be $\bar{C}_{d/p} = 4.7$. This result is independent of the gas mixture type, in the vicinity of the optimal reduced field, as shown in Fig. 3.9.

The model presented is valid as long as the ion depletion layers make a negligible contribution to the discharge characteristics. When the discharge width becomes less than 0.1 mm, the dielectric slab is dispensable due to the stabilizing effect of the ion depletion layers. However, due to high laser optical-losses, and increased electron diffusion losses, this thin discharge geometry is impractical in a CO₂ slab-laser design.

After analyzing and optimizing a solution for one of the main slab-laser design constraints in the previous sections, we present an investigation of the microwave excitation of CO₂ lasers in two experimental setups described in the next chapter.

4. Microwave-Excited Lasers

Microwave excitation of gaseous lasers is favorable due to (a) the availability of 2.45 GHz magnetrons, and (b) the advantageous physical characteristics of microwave discharges, as outlined in the previous chapters. Following the increased usage of magnetrons in domestic applications, they have become greatly obtainable and extremely low-cost power sources. Supplying high peak to average power ratios, electronic tubes are advantageous for pulsed microwave discharges in which the α to γ discharge transitions are cancelled. Those qualities make the magnetron a favorable excitation source for high power gaseous lasers with large peak to average power ratios. However, the short free-space wavelength of the microwave radiation demands specific considerations regarding the power source coupling and matching to the plasma-loaded microwave resonator. A longitudinally homogeneous microwave-discharge required for a high laser-efficiency is not as easy to form as in the low frequency RF discharge.

Microwave excitation of gaseous lasers has been explored in schemes such as waveguide fast-flow and sealed lasers, in cylindrical, coaxial, and slab-configured schemes. Several methods were suggested for a longitudinally homogeneous discharge formation. Freisinger *et al.* [25] used a T shaped rectangular resonator to which a cylindrical laser-tube was inserted. The resonator was operated slightly above cut off. For a symmetric microwave feeding, a cosine electric-field distribution was observed. Ikeda *et al.* [27] employed a TM_{010} mode cylindrical resonant cavity yielding a longitudinally-homogeneous microwave discharge. März and Oestreicher [31] designed a traveling wave microwave circuit for a homogeneous microwave-discharge formation, using a variable microwave load. In another scheme, they have used a tapered slab-configuration to improve the laser head matching, and to compensate for the microwave power decrease along the laser head [30]. A slab waveguide laser employing the characteristic of a longitudinally homogeneous microwave-discharge in a constant cross-section has not been demonstrated.

Two conceptually different microwave-excited laser setups are investigated in this thesis for overcoming the inhomogeneous microwave-excitation difficulty, namely:

Scheme #1. Parallel-plate matching of a magnetron to a cylindrical laser head.

Scheme #2. Distributed coupling of a magnetron to a slab laser-head by a rectangular waveguide.

The microwave electric-field distribution in the first laser is simulated, and the discharge axial-luminescence is presented. A simple model describing the transient axial and temporal electric-field amplitude-buildup in an arbitrary resonator is developed. The critical power-source coupling to the resonator is considered for an empty resonator and for a plasma-loaded resonator. Using the model, a simple distributed coupling method is demonstrated for a CO₂ slab-laser with a constant cross-section. Experimental results verifying the microwave longitudinal homogeneous-discharge are presented. A 3D numerical microwave design-tool (ANSOFT HFSS software) is used for the simulation of the complete microwave structure of the slab laser. The results of the presented model are reinforced by experiments. The feasibility of constructing a microwave-excited slab-laser, employing an easily optimized, longitudinally-homogeneous discharge is demonstrated.

This chapter provides the experimental setup detailed description for both investigated lasers. The experimental results for both devices are presented and discussed.

4.1. The Cylindrical Parallel-Plate CO₂ Laser (Scheme #1)

The construction of the cylindrical parallel-plate laser follows several design considerations. This laser is designed for magnetron excitation, exploring the microwave discharge in a simple and compact cylindrical-configuration. In this scheme, the direct loading of a magnetron by a resonator including laser-plasma is studied. The next sections outline the experimental setup components and also the microwave-setup design considerations. After presenting the device experimental-results, the benefits and limitation of this laser configuration are discussed.

4.1.1. Experimental Setup

Fig. 4.1 presents the first experimental device. A lens-like parallel-plate resonator fed by a magnetron antenna couples the microwave energy to two water-cooled strips.

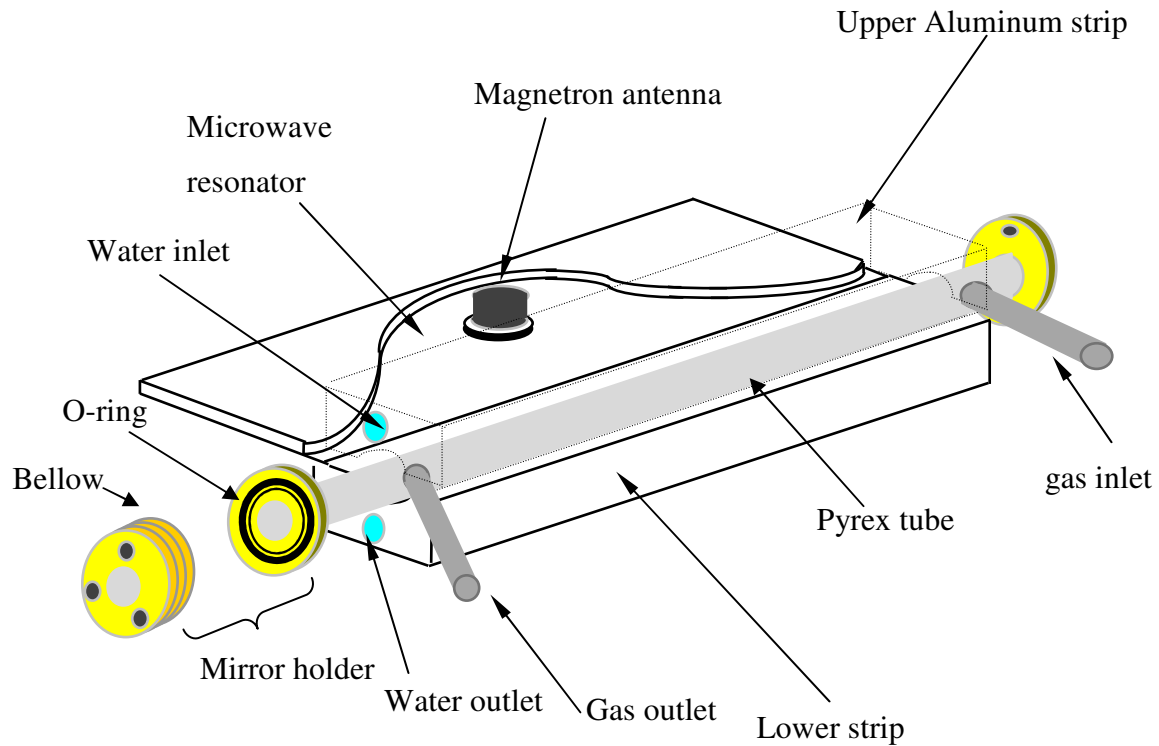


Fig. 4.1: The parallel-plate cylindrical-laser first experimental-arrangement.

The strips are shaped with a curvature of a 12 mm external-diameter Pyrex tube. In this configuration, the design complexity of a Pyrex cooling-jacket is avoided. The parallel-plate spacing is 8 mm, and the length of the Pyrex tube within the resonator is 300 mm. A slit surface of $8 \times 300 \text{ mm}^2$ irradiates the laser gas. Side Pyrex nipples are welded to the main Pyrex tube externally to the microwave resonator. Mirror holders are attached to the laser head in two ways. In one scheme, a covar-to-Pyrex section is welded to the main Pyrex-tube ends (Fig. 4.1), and attached to the mirror-holders by short bellow sections. This optical resonator arrangement proves unsteady. It is practically impossible to align the optical resonator for the principal laser mode, and only high-order modes are observed. A different optical resonator configuration is presented in Fig 4.2. The Pyrex tube is attached to the rims of the microwave resonator by application of Torr-seal. Mirror holders are attached to the resonator's

outside-wall by O-rings. This configuration increases the stability of the optical resonator alignment, and allows the calibration of the resonator the four fundamental laser modes. Holes are drilled in the aluminum mirror-holders and serve as the gas inlet and outlet (Fig. 4.2). Thus, no changes are made in the cylindrical Pyrex tube and the design is simplified. The mirrors are aligned by moving them on O-rings by three micrometer-heads for each mirror.

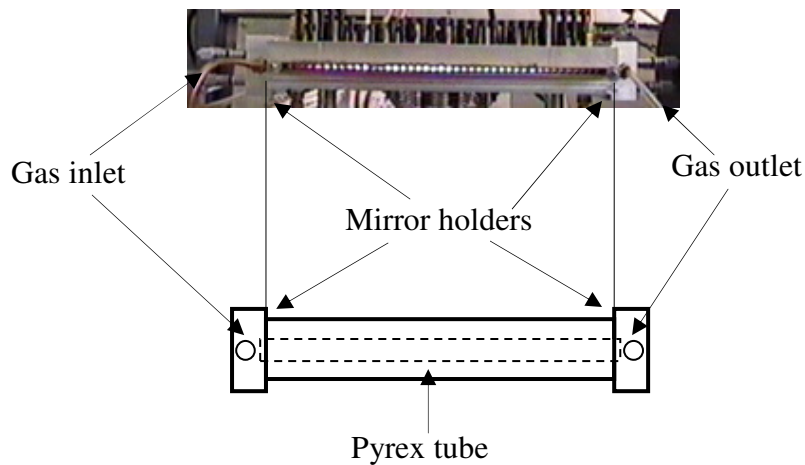


Fig. 4.2: The parallel-plate cylindrical-laser second experimental-arrangement.

The experimental setup is shown in Fig. 4.3. A 5 kV DC power-supply feeds the magnetron through a solid-state high-voltage switch (Behlke HTS 81). An external function generator (HP 33120A) sets the pulse frequency and duty cycle. A high-voltage probe (Textronix P6015A) measures the high voltage across the magnetron, and the magnetron current is measured by a Rogowski coil (Pearson Inc. Model No. 110). A standard He:CO₂:N₂ = 8:1:1 gas mixture is used. A diaphragm pressure-meter (Edwards CG 16K) monitors the gas pressure, and the pressure is set by a bellows-sealed valve (Hoke 4100 316SS). The average laser-power is measured by a thermal detector (Scientech 360 0203), and the peak laser-power is measured by a Pyroelectric detector (Molelectron P4-40). The magnetron high-voltage and current relative measurements are displayed on a digital oscilloscope (Textronix TDS 210). An external antenna connected to a microwave detector (Fig. 4.3) is used to measure the microwave signal.

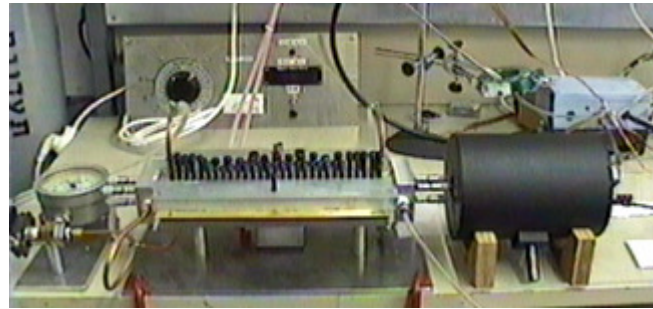
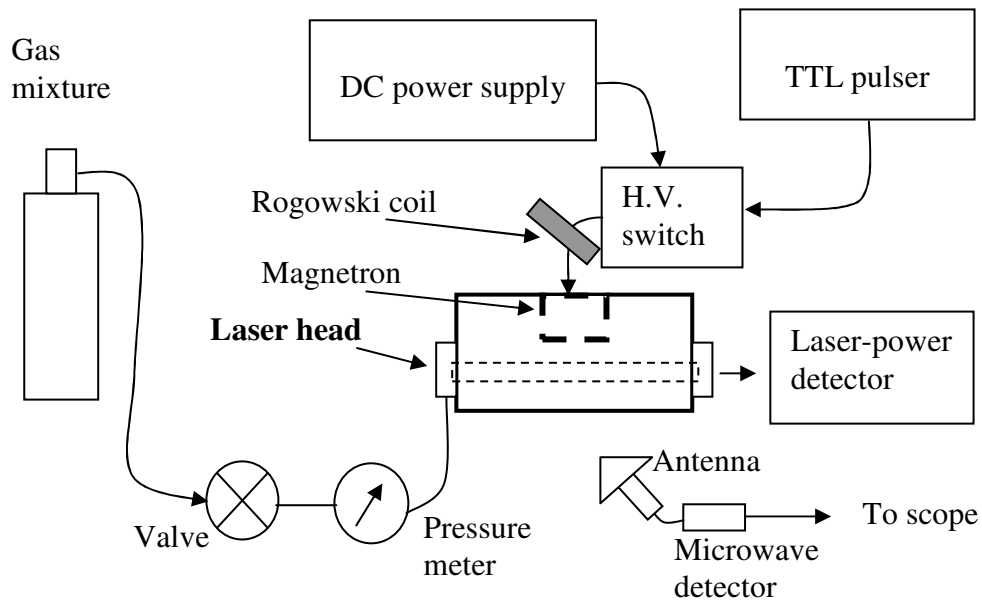


Fig. 4.3: The parallel-plate cylindrical laser experimental setup.

The DC high-voltage power supply is connected to the 220 V line through a power meter (YEW 2042). Comparing the average laser-power to the total average consumed-power yields the setup efficiency.

The next section presents the parallel-plate cylindrical-laser microwave design considerations.

4.1.2. Microwave Design Considerations

The parallel-plate laser cross-section is depicted in Fig. 4.4. A magnetron feeds a parallel-plate resonator [72,77], which is matched to a cylindrical laser head.

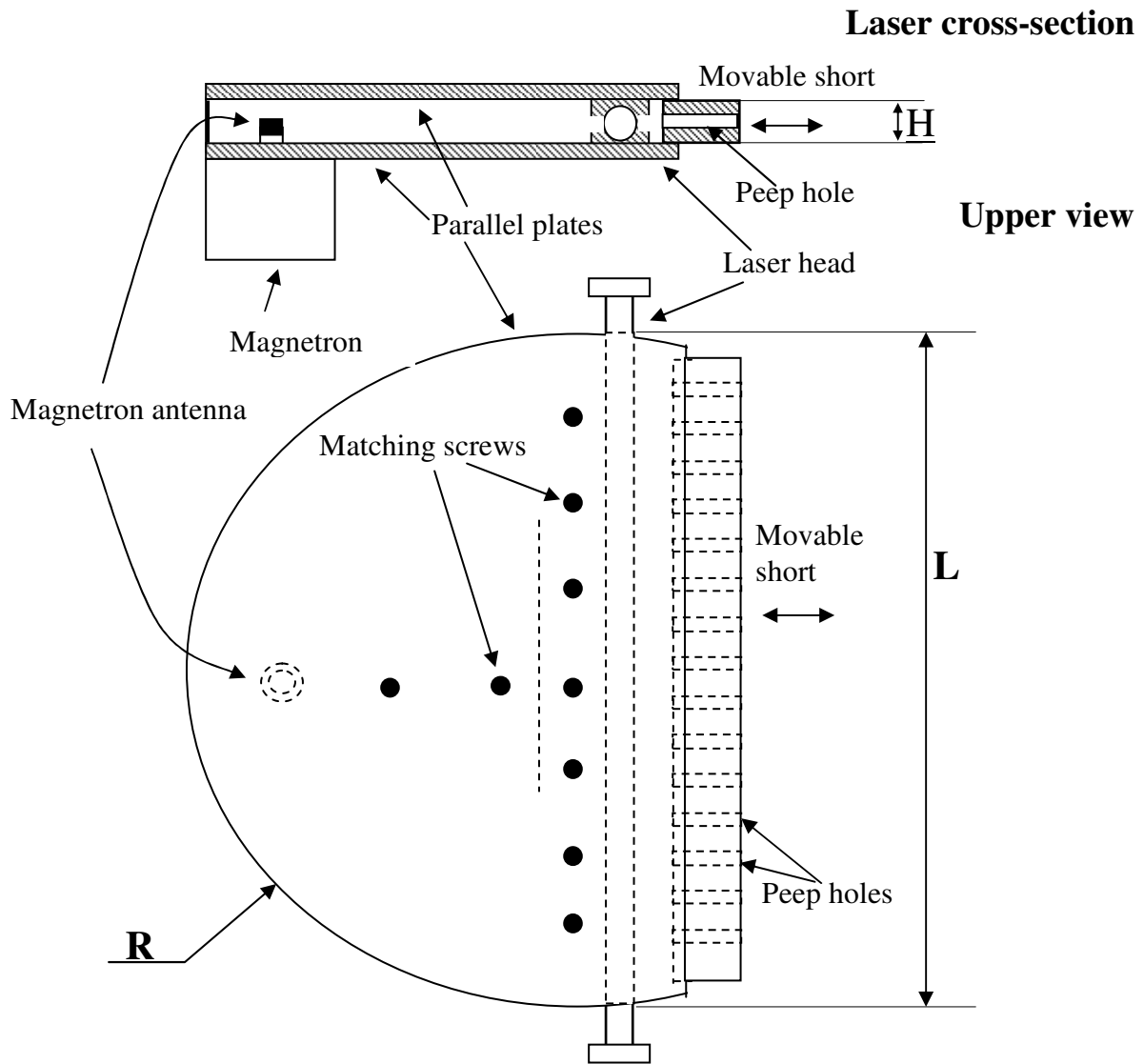


Fig. 4.4: The parallel-plate laser device.

The shape of the resonator is curved to allow better radiation tapering to the laser head. Table 4.1 specifies the setup dimensions. A simulation of the electric-field magnitude is depicted in Fig. 4.5 for different mode combinations in the lens-like parallel-plate resonator. The calculation is performed using the MATLAB software.

The different modes of the lens-like microwave resonator are combined, according to the boundary conditions it dictates. The magnetron antenna location is chosen as the resonator excitation port.

P Dimensions [mm]	
<u>Resonator :</u>	
Width (L)	300
Height (H)	8
Curvature radius (R)	190
<u>Pyrex tube:</u>	
Length	310
Outer/inner diameter	12/10

Table 4.1: Parallel-plate resonator dimensions.

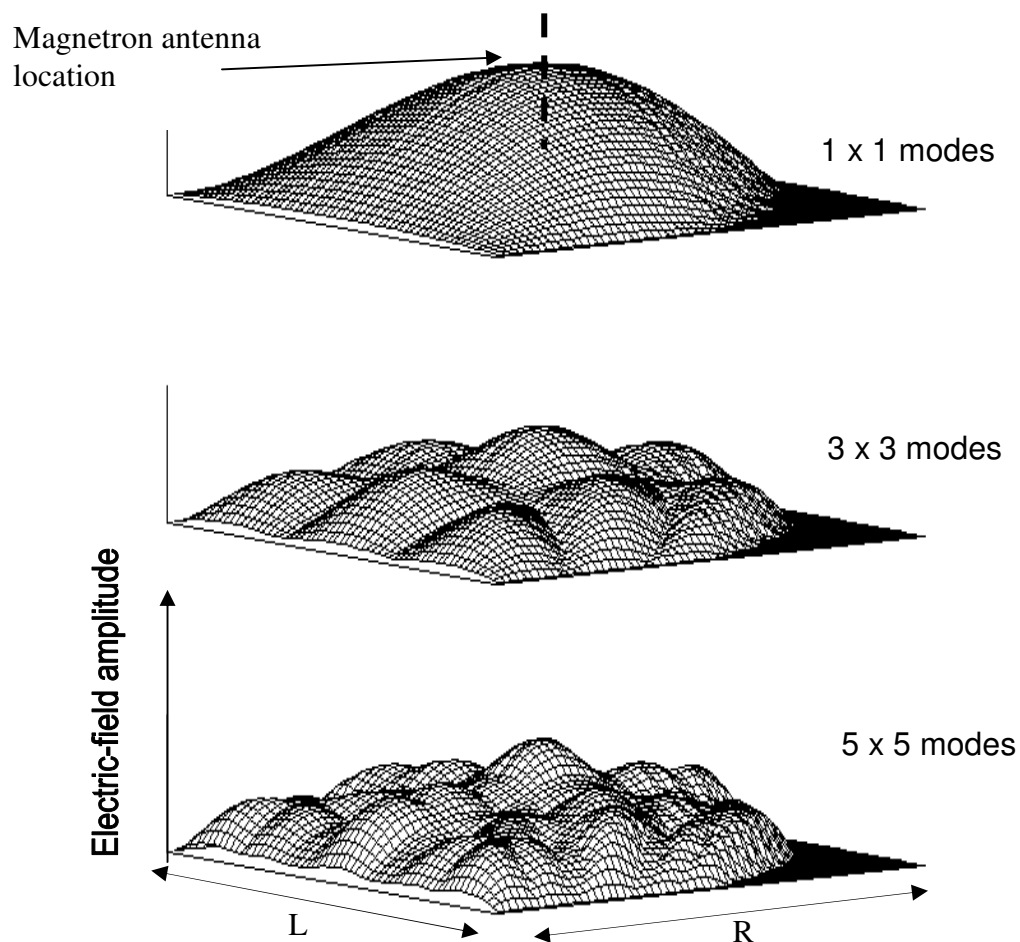


Fig. 4.5: different modes of the parallel-plate resonator.

Microwave radiation is injected into the resonator by the magnetron antenna (Fig 4.4). Many modes of the parallel-plate resonator develop at the point of energy coupling by the magnetron antenna. The domination of a certain mode is dictated by the boundary conditions of the resonator, its dimensions, the input-probe characteristics, and the magnetron frequency. The discharge field at the laser head is a sum of the resonator's odd modes due to the symmetrical feeding. The motivation for this structure, as depicted in Fig. 4.5, is to achieve a sum of the three fundamental odd longitudinal-modes (first, third and fifth modes) resulting in a homogeneous longitudinal discharge-field. This is achieved by controlling the modes amplitudes at the laser head with the tuning screws, and the movable short at the end of the resonator, beyond the Pyrex tube.

Fig. 4.6 shows the discharge luminescence along this laser head through the movable short.



Fig. 4.6: The parallel-plate laser discharge luminescence, as observed through peep-holes drilled in the movable short along the laser axis (see Fig. 4.4).

The discharge looks homogeneous, and no nulls appear in the longitudinal field pattern. However, the luminescence becomes whiter along the gas stream due to the gas dissociation [43].

The main disadvantage of this setup (considering the microwave design) was the inability to control the matching of the magnetron antenna to the parallel-plate resonator. As a result, the magnetron operated in a non-optimal regime (Appendix A). The height of the parallel plates (~ 1 cm), as dictated by the chosen laser-head dimensions, formed a basic mismatch between the magnetron impedance and that of the resonator. Even though the discharge seems homogeneous, the efficiency of this laser, as a consequence of the impedance mismatch, was relatively low (~ 1 %).

In section 4.2, a different microwave design that overcomes many of the limitations of the parallel-plate laser is presented.

4.1.3. Experimental Results (Scheme #1)

Figures 4.7 and 4.8 present the optical-mode structure of the parallel-plate cylindrical laser. The instability of the optical alignment in the first arrangement (Fig. 4.1) stems from the free standing mirror holders and the use of bellows in them. It yields high-order transverse laser-modes only, as presented in Fig. 4.7.



Fig. 4.7: The high-order modes of the first optical resonator configuration.

Fig. 4.8 presents the improved optical setup results. The four fundamental optical-resonator modes are evident, and obtained by the optical resonator alignment.

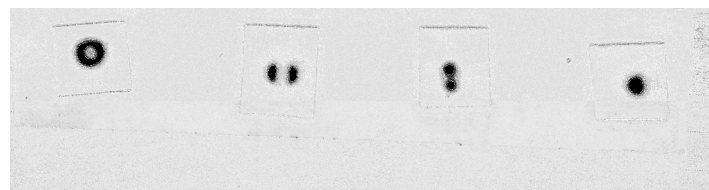


Fig. 4.8: The optical modes of the second optical configuration.

Figures 4.9 and 4.10 show the average and peak laser-power, respectively, versus the pulse width for pulse-repetition frequencies of ~ 450 , 670 , and 840 Hz.

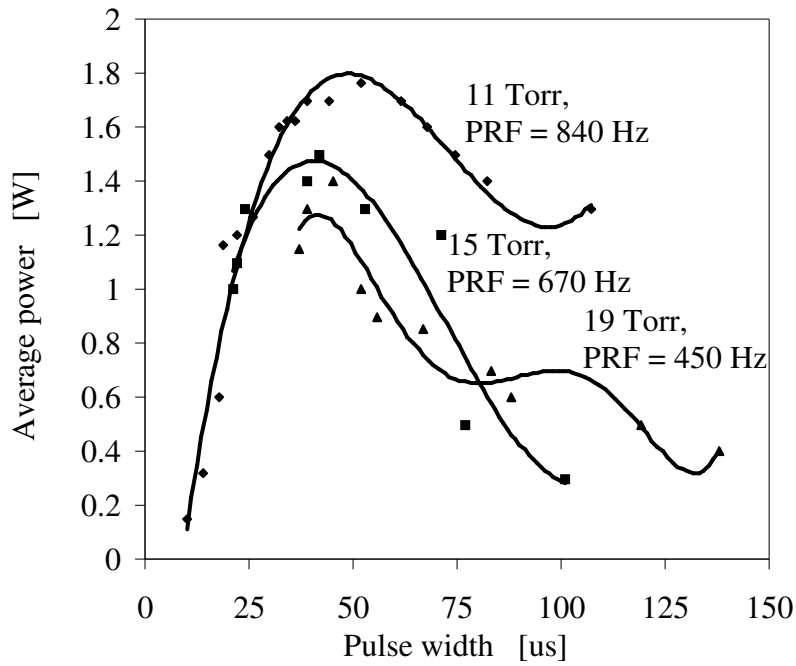


Fig. 4.9: The average laser power versus the pulse width for three pulse-repetition frequencies at optimized gas-pressures.

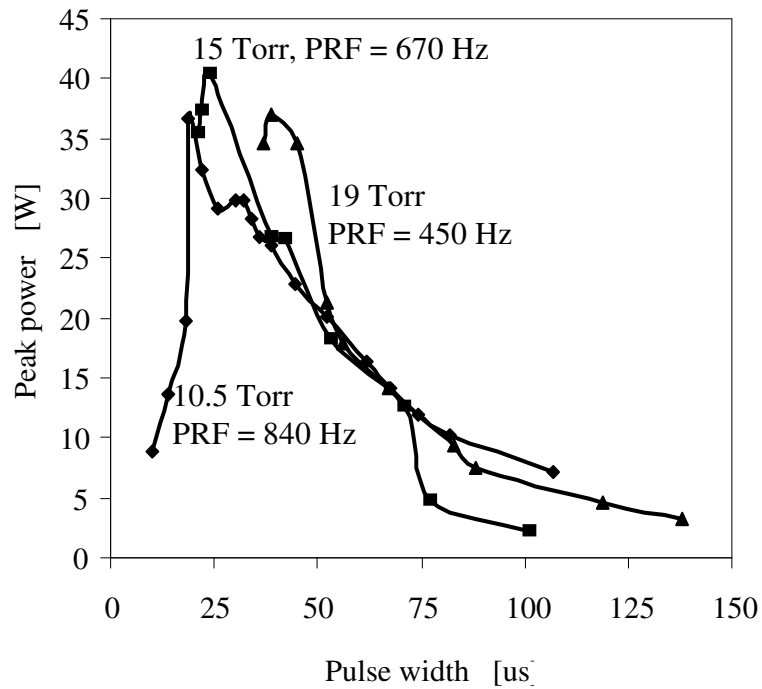


Fig. 4.10: The peak laser-power versus the pulse width for three pulse-repetition frequencies at optimized gas pressures.

The pressure for each pulse repetition-frequency was chosen to be the optimal for a specific pulse frequency. The maximal detected average-power is ~ 1.8 W, at a pressure of 11 Torr, a microwave pulse-width of ~ 52 μ s, and a pulse repetition-frequency of 840 Hz. The maximal detected peak laser-power is ~ 40 W, at a pressure of 19 Torr, a microwave pulse-width of ~ 25 μ s, and a pulse repetition frequency of 670 Hz. The total laser efficiency does not exceed 1 %.

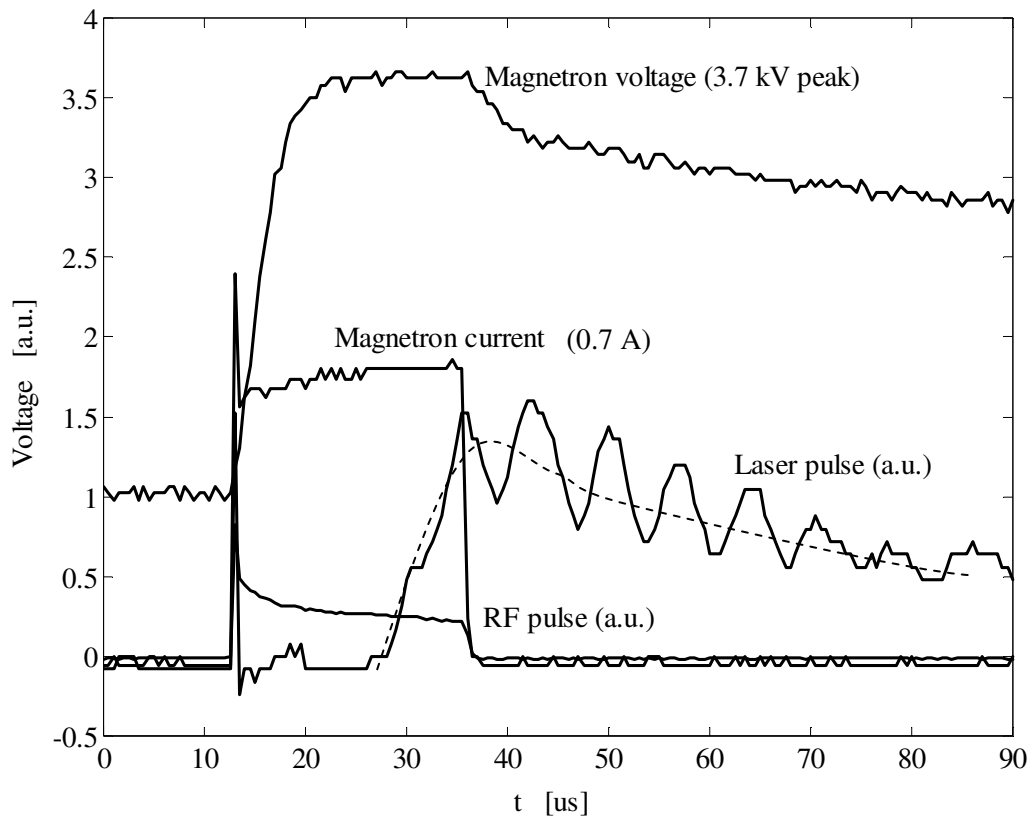


Fig. 4.11: A temporal presentation of a typical laser-pulse.

A typical laser-pulse is presented in Fig. 4.11, as recorded by a digital oscilloscope. Four traces are shown for a 25 μ s current pulse. The magnetron high-voltage peaks at ~ 3.7 kV with a relatively large rise-time (~ 5 μ s) determined by the DC power-supply capacitor. The average magnetron-current is ~ 0.7 A. The spike evident at the beginning of the pulse forms due to the inductive nature of the magnetron wiring to the power supply. At high input-powers and large pulse-rates this phenomenon strengthens. A solution for this phenomenon is presented in the next

sections describing the slab-laser configuration. The current time-span represents the operation time of the magnetron. It is observed that the microwave pulse follows the magnetron current, and decreases as the current increases. The delayed laser pulse is about twice as large as the microwave pulse. The noise in the laser-pulse measurement is due to the operation of the thermal detector in a noisy environment. In the next experimental setup this measurement is improved, as will be further discussed (Appendix B).

4.1.4. Discussion

The parallel-plate cylindrical laser is a compact device that allows observing the phenomena in a microwave-excited gas laser using a simple design. The design of this device avoids complex glass processing, and uses a standard cylindrical Pyrex-tube with no modifications. The microwave applicator in this scheme is a commercial magnetron coupled to a parallel-plate resonator embracing the Pyrex tube. A homogeneous discharge is observed in this device. It is achieved by tuning screws and a variable short at the wide end of the microwave resonator (Fig. 4.4). An average power of ~ 2 W is measured in this device with a peak power of 40 W. The total efficiency of the device does not exceed 1 %. This minute efficiency is the result of the incompatible magnetron and parallel-plate-resonator impedances, and due also to discharge instabilities. The large discharge-width (10 mm), as dictated by the inner Pyrex-tube radius, does not allow a proper cooling of the gas, thus, the rise of unrestrained thermal-instabilities deteriorate the laser action. Fig. 4.12 demonstrates an extreme case of a thermal instability evolvment, in which the discharge constriction deforms and eventually punctures the cylindrical Pyrex-tube.

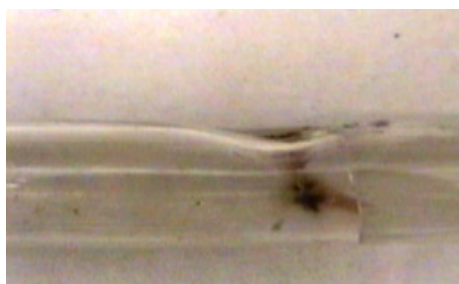


Fig. 4.12: The Pyrex-tube breakdown caused by the development of a thermal instability.

The parallel-plate cylindrical laser, in spite of its disadvantages, is a simple and compact design in which the microwave excitation of laser plasma can be studied. Variations in the microwave design, namely: (a) changing the microwave resonator impedance (by a variable cross-section, for instance), or (b) adding another matching link between the magnetron and the resonator may improve the device efficiency. Using a thicker cylindrical Pyrex-tube together with operating the laser at shorter pulse widths can decrease thermal instabilities.

The next sections describe in detail the CO₂ slab-laser experimental setup, design considerations, and the experimental results and optimization.

4.2. The CO₂ Slab-Laser (Scheme #2)

The requirement of a compact, slow flow CO₂ laser yielding tens of watts of average power with a high peak to average power ratio, has led to the design and construction of a microwave-excited slab-laser. The desired design characteristics included a parameter operation-regime of tens of μ s pulse widths, and above 1 kHz pulse repetition frequencies. A homogeneous microwave discharge was required for the enhancement of the overall device efficiency, when a 2.45 GHz, 2 kW industrial magnetron was used. By viewing the microwave-source to plasma power matching difficulties in other schemes, a simple microwave power matching ability was sought.

The next sections describe in detail the experimental setup of the CO₂ slab-laser investigated in this thesis. Microwave design considerations supported by analytical as well as numerical models are presented and verified by the experimental results. A comprehensive description of the laser experimental results and optimization is presented. The experimental results given for two discharge widths include measurement and optimization for the following parameters:

- Gas pressure and flow rate.
- Microwave pulse width and repetition frequencies.
- Microwave power coupling and matching.
- Small signal gain.
- Optical-resonator output coupler.
- Beam quality.

4.2.1. Experimental Setup

The experimental setup of the CO₂ slab-laser is designed considering the parallel-plate cylindrical-laser experimental-device limitations. Appendix A describes the magnetron chosen for this set up, and Appendix B outlines the different high-voltage switching considered for it. Fig. 4.13 shows the slab-laser experimental setup. An 8 kV D.C. power-supply is connected through a high-voltage switch (Rotem MOSFET-switch) to the magnetron. The pulse width and repetition-frequency are controlled through the switch control-panel. A Rogowski coil (Pearson Inc. model No. 110) monitors the magnetron current, and a high-voltage probe (Textronix P6015A) monitors the magnetron high-voltage. A variac (Voltac SB-10) controls the magnetron heating-voltage. The microwave setup and the laser head are described in detail in the next section. Water is circulated through the laser-head ridges and the microwave circulator protecting the magnetron. Two thermometers placed at the laser cooling-water inlet and outlet allow to measure the discharge average power dissipation. An optical detector (Ophir F300A-SH) measures the average laser-power, and a Pyroelectric detector (Molelectron P3-00) allows the peak laser-power measurement. A 2.45 GHz microwave survey-meter (Holiday Ind., Model 1501) measures the microwave leakage in the setup. All signal-lines monitored in the setup (magnetron high-voltage and current, reflected and transmitted-wave voltages, laser-pulse amplitude voltage, and all control lines) are rolled on a ferrite ring to cancel the common-mode noise (see Appendix B). Table 4.2 summarizes the physical dimensions of the setup and Fig. 4.14 depicts the laser-head configuration. The gas mixture used in this setup is composed of 18 % of N₂, 6.5 % of CO₂, 1.5 % of Xe, and 74 % He. A Wilmad rectangular Pyrex-tube (Table 4.2) serves as the gas confinement chamber, and as the microwave stabilizing ballast dielectric-strip. Laser mirrors are attached directly to the Pyrex tube, or by the use of mirror holders (Appendix C). A hemispheric optical-resonator is used. The rear full-reflecting mirror has a 5 m radius of curvature, and the front output-coupler is optimized.

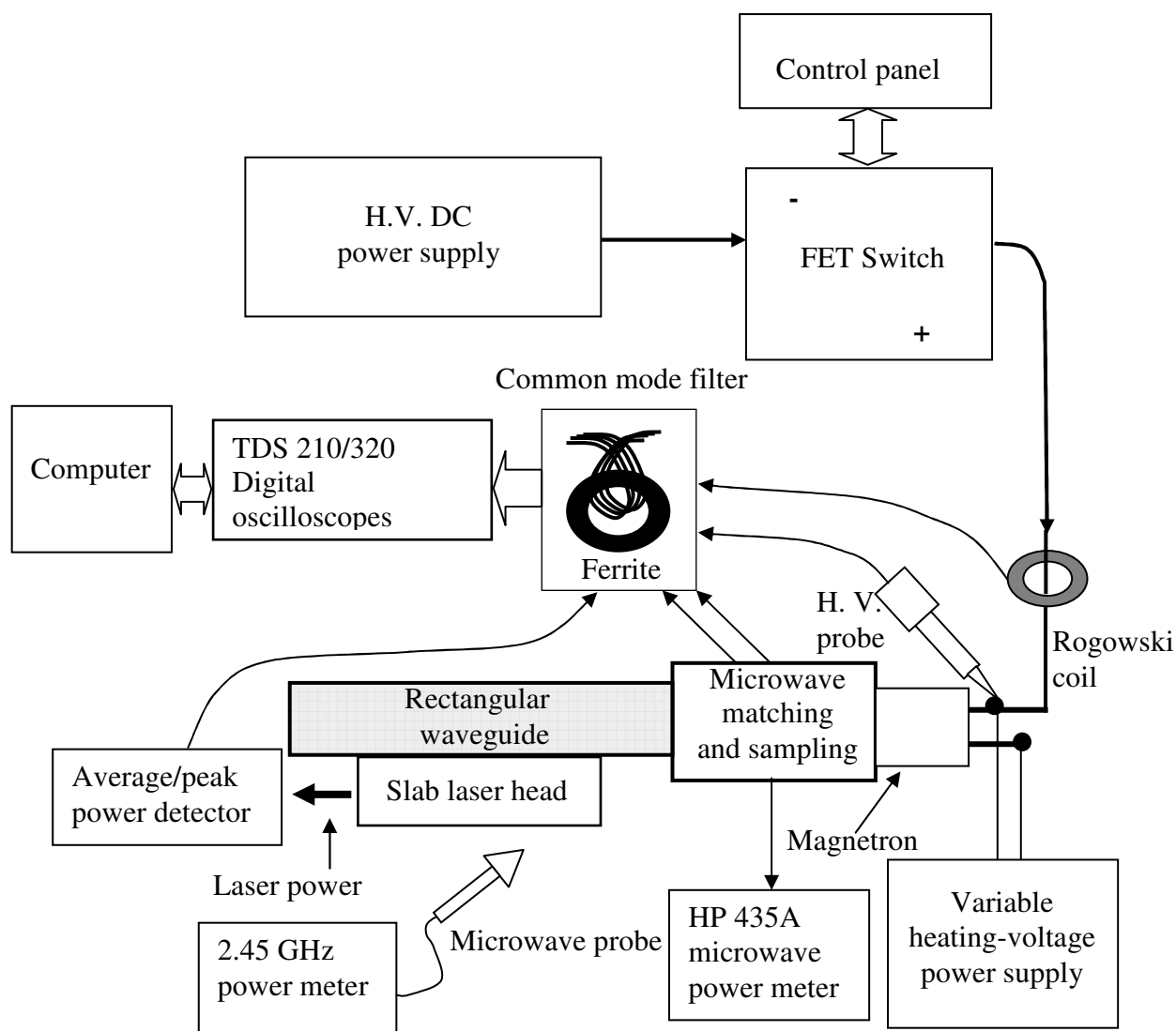


Fig. 4.13: The slab laser experimental setup.

<u>Rectangular waveguide (Copper):</u>		
Length	740	
Width	61.4	
Height	30.7	
<u>Double ridged waveguide (Copper):</u>		
Length	400	
Width	41	
Height	8	
Ridge width	20	
Ridges spacing	4.65	
<u>Rectangular Pyrex tube</u>		
(Corning 7740 or Schott 8330):		
Inner width	21.0	20.0
Inner height	1.5	2.0
Wall thickness	1.50	1.30
Length	425	
Wall tolerance	± 0.3	

Table 4.2: Physical dimensions (all in millimeters).

The microwave experimental setup is illustrated in Fig. 4.14. The microwave source is a 2 kW magnetron (Hitachi 2M130) at 2.45 GHz, delivering a maximal peak-power of ~ 15 kW at short pulses of 2-30 μ s (Appendix A). The microwave radiation is delivered through a circulator (Philips PDR-26) acting as an isolator to a 60 dB coupler (Muegge MW-6971-0070). This allows the monitoring of the transmitted and reflected powers in this setup. An E-H tuner enables the basic matching of the radiation to a rectangular resonator. A double ridge waveguide is attached sideways to the rectangular resonator (Fig. 4.14). The microwave radiation is coupled to the double ridge waveguide through a slit. A Wilmad rectangular Pyrex-tube (see Table 4.2) is placed between the ridges and attached to them by application of a Silicon heat-conducting paste and indium strips [76] (see Appendix C). The tube serves as the discharge chamber, and as the microwave stabilizing ballast dielectric-strip (as discussed in Chapter 3). The chosen Pyrex tube wall thickness ensures the

prevention of thermal instabilities in the operation regime [69]. The fine tuning of the discharge electric-field is achieved by: (a) variable stub at one end of the rectangular-waveguide resonator, and (b) screws along the slit connecting the two waveguides. The average input microwave-power is measured by a microwave power-meter (HP435A). The setup dimensions are summarized in Table 4.2.

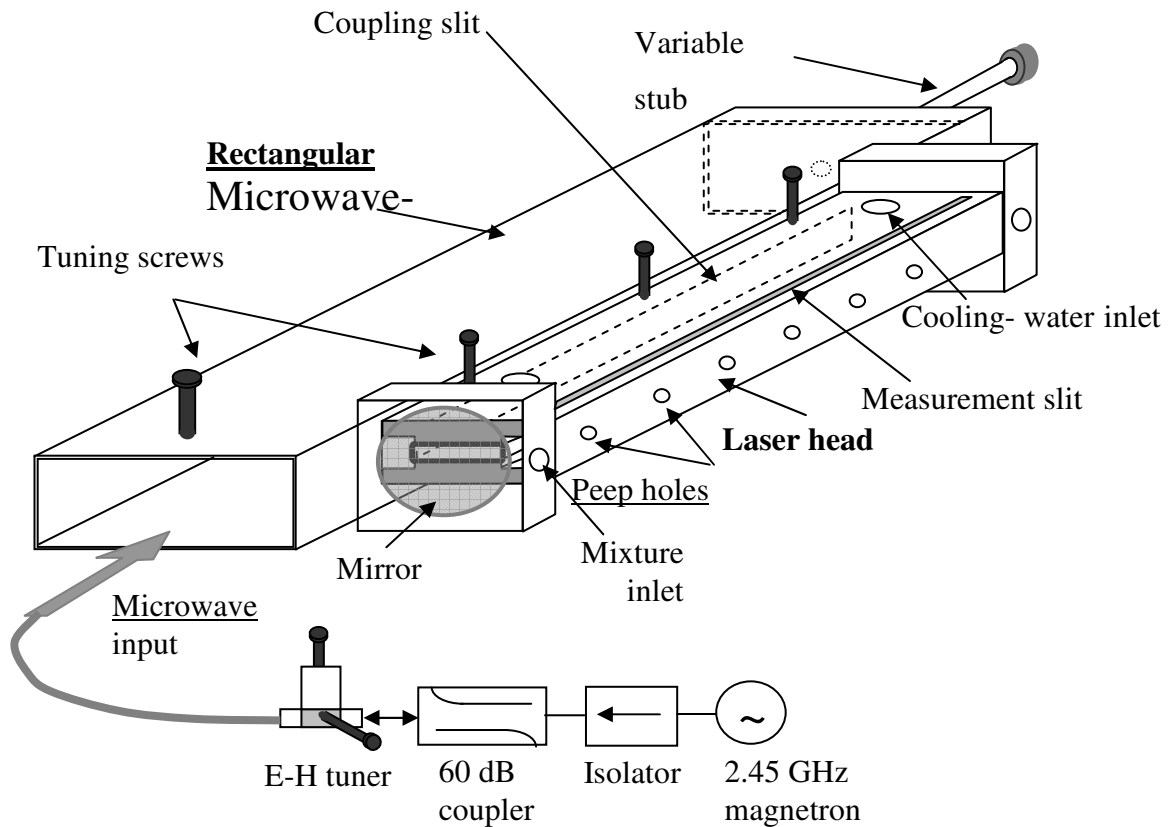


Fig. 4.14: The experimental device and microwave-setup.

4.2.2. Microwave Setup and Design

A compact CO₂ laser design realized by a microwave-excited slab laser-head configuration has the following features: (a) tens of watts of average power, (b) a large peak to average power-ratio, and (c) operation in a low gas-flow or sealed regime. A longitudinally homogeneous microwave-discharge is achieved in this scheme by a rectangular waveguide resonator that operates slightly above a cutoff frequency of 2.45 GHz. Thus, only its fundamental longitudinal TE mode propagates along the resonator. For improving the discharge electric-field uniformity, a double-

ridged waveguide [73-76] (forming the laser-head) is symmetrically H-plane attached to the rectangular resonator (Fig. 4.14). The laser head is axially shorter than the resonator. Therefore, the electric-field amplitude at the laser-head edges drops to $\frac{2}{3}$ of the maximal amplitude at the center of the rectangular-resonator.

The cutoff wavelength for a double-ridged waveguide [74] is

$$\lambda_c = 2(a_1 - a_2) \left\{ 1 + \left[(2.45 + \frac{a_2}{a_1}) \epsilon_r a_2 \frac{b_1}{[d_b + \epsilon_r(b_2 - d_b)](a_1 - a_2)} \right] + \frac{4\epsilon_r b_2}{\pi[d_b + \epsilon_r(b_2 - d_b)]} \left[1 + \frac{1}{5} \sqrt{\frac{b_1}{a_1 - a_2}} \right] \frac{b_1}{a_1 - a_2} \ln \left(\frac{1}{\sin(\pi b_2 / 2b_1)} \right) \right\}^{\frac{1}{2}} . \quad (46)$$

a_1 and a_2 are the waveguide and ridges widths respectively, b_1 and b_2 are the waveguide height and the ridges spacing respectively. ϵ_r and $d_b/2$ are the relative dielectric constant and wall thickness of a rectangular Pyrex tube placed between the ridges, as shown in Fig. 4.15.

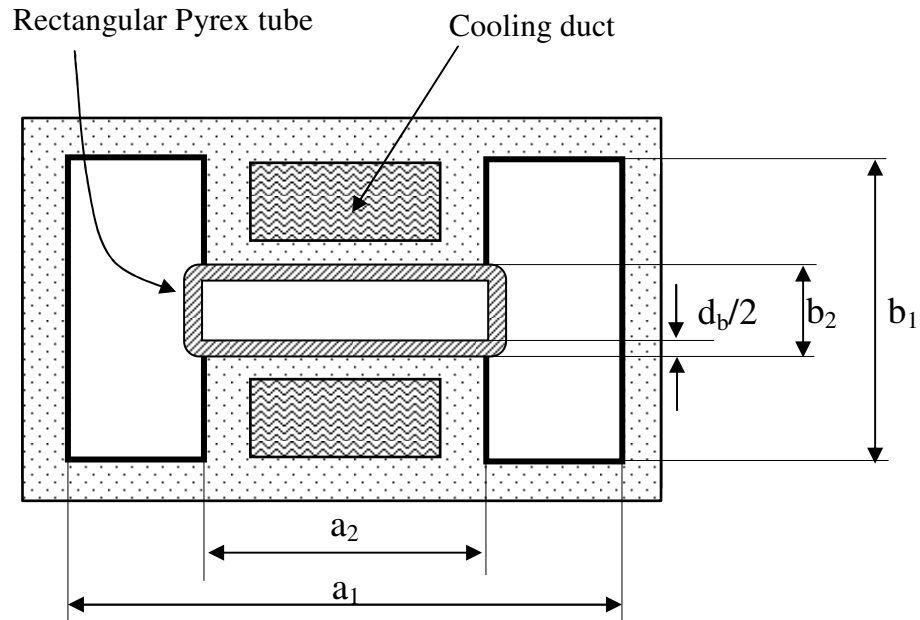


Fig. 4.15: The laser-head double-ridge waveguide cross-section.

The double-ridged waveguide is designed to be below cutoff, considering a discharge width of 2 or 1.5 mm (see Table 4.2), and the dielectric properties of the Pyrex tube. Thus, the electric field in the discharge zone is composed of a sum of the decaying odd axial-modes of the ridged waveguide, due to the symmetrical coupling between the resonators [72]. At the same time, the principal longitudinal-mode of the rectangular waveguide continues to propagate.

4.2.3. Experimental-Measurements Setup

The presented CO₂ slab-laser is designed for pulsed operation in the kilohertz regime with pulse widths of tens of microseconds. Average and peak laser powers are measured with respect to the pulse width, pulse repetition-frequency, gas pressure, and gas flow rates for various input microwave-powers. The measurements are performed for two different discharge cross-sections. One scheme includes a Pyrex tube with an inner height of 2.0 mm and a wall thickness of 1.3 mm. Another scheme includes a Pyrex tube with 1.5 mm discharge width and a 1.5 mm wall thickness. Measurements are taken for each scheme at different gas flow-rates, for which the gas inlet and outlet configurations are changed accordingly (Appendix C). The small-signal gain is measured for each tube, and the beam quality is estimated. The output coupler is optimized for both configurations.

The discharge uniformity measurements are performed in two ways. The microwave power homogeneity is measured by a Scalar Network Analyzer (HP8757A). Microwave power is injected through a coax-to-waveguide coupler attached to a magnetron antenna. A microwave dipole-antenna probe inserted into a slit along the ridges of the laser head (Fig. 4.14) couples the transmitted microwave power to the analyzer. The measurement of the reflected power (with the circulator excluded from microwave chain) allows the proper matching of the microwave power at 2.45 GHz by the tuning screws. A measurement of the discharge light emission is taken by an optical detector (Ophir PD300-3W) calibrated to 488 nm. This measurement allows the calculation of the reduced field variation along the laser head. Using the experimental data presented by Ledig and Schreder [41], the CO₂ molecules' electronic-states energy is estimated for a gas-mixture of He:N₂:CO₂ = 8:1:1. Thus, the longitudinal discharge uniformity measurements are

performed for this gas mixture as follows: after the laser operation is optimized (i.e. optimal reduced field (E/N)), the discharge light emission at 488 nm is measured through the peep holes (Fig. 4.14) along the laser head axis. Therefore, the deviation from the optimal reduced field can be extracted.

4.2.4. Experimental Results (Scheme #2)

The succeeding subsections summarize the following CO₂ slab-laser measurements: (a) longitudinal discharge homogeneity, (b) power measurement for the two chosen discharge widths, (c) laser output pulse-widths, (d) small signal gain, (e) beam quality, and (f) output coupler optimization. An extensive discussion of the results is given in the next chapter.

4.2.4.1. Longitudinal Discharge Homogeneity

This subsection describes the experimental measurement of the longitudinal variation of the discharge electric-field amplitude.

Figures. 4.16a and 4.16b depict the transmitted-wave amplitude along the laser head for two different dielectric-loads in the laser head (as presented in Table 4.2).

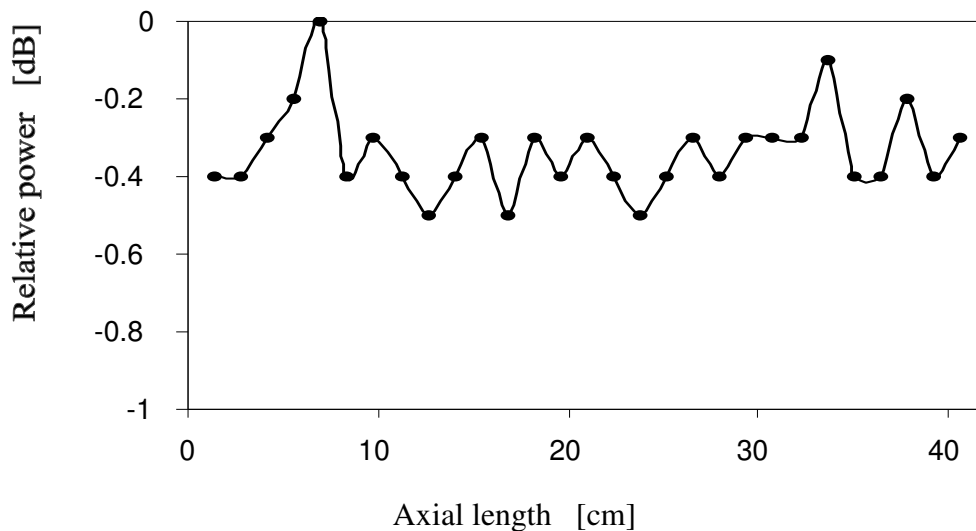


Fig. 4.16a: The longitudinal variation of the transverse microwave-power measured perpendicularly beyond the ridges for a discharge width of $d_p = 2.0$ mm.

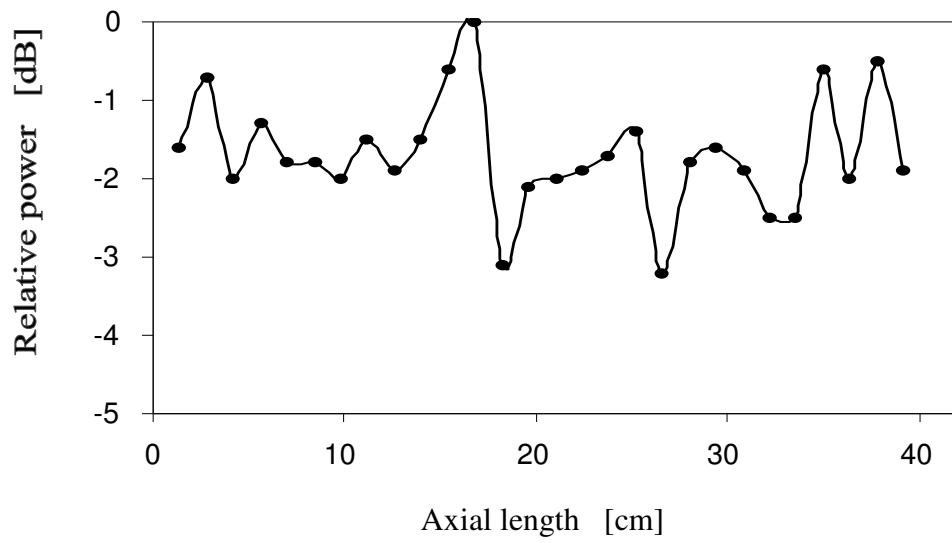


Fig. 4.16b: The longitudinal variation of the transverse microwave-power measured perpendicularly beyond the ridges for a discharge width of $d_p = 1.5$ mm.

Figures. 4.17a and 4.17b show the variation of the reduced field along the laser head, as calculated from the discharge light-emission.

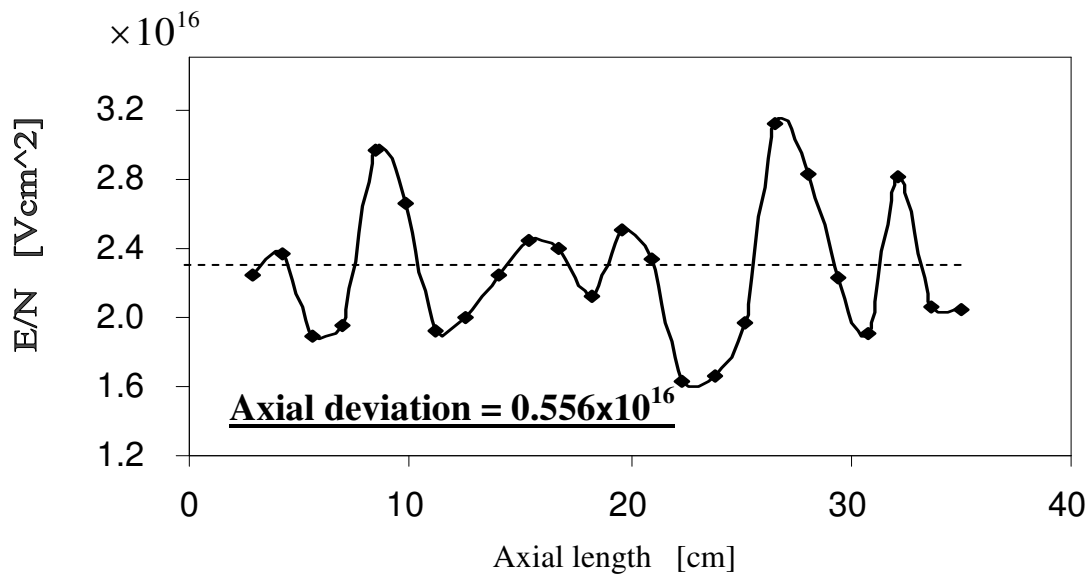


Fig. 4.17a: Calculated electric reduced field corresponding to the measured discharge light-emission intensity for a discharge width of $d_p = 2.0$ mm.

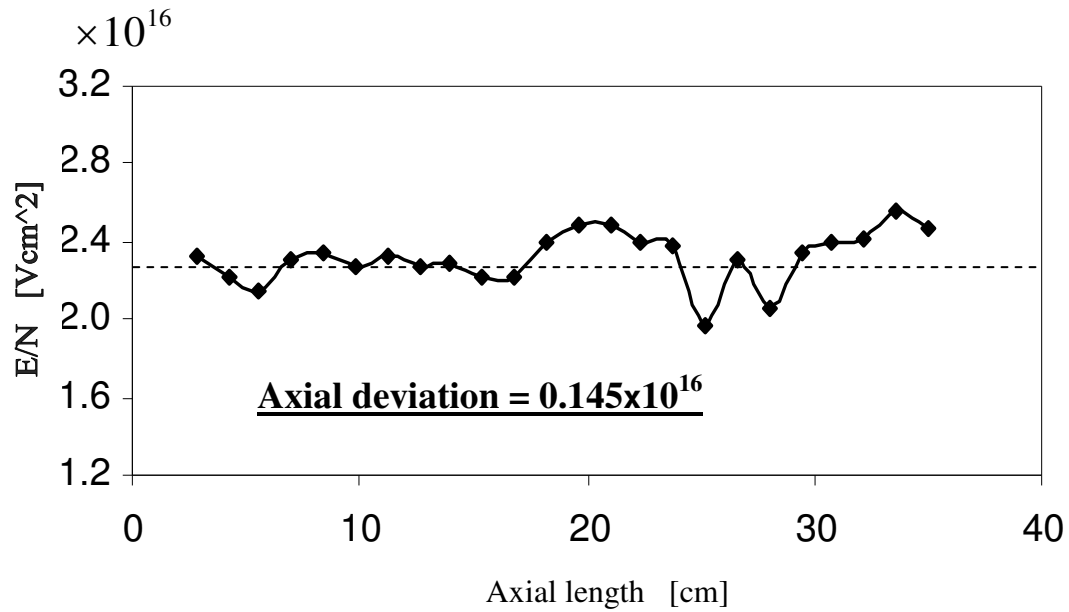


Fig. 4.17b: Calculated electric reduced field corresponding to the measured discharge light-emission intensity for a discharge width of $d_p = 1.5$ mm.

The CO₂ slab-laser discharge longitudinal luminescence is shown in Fig. 4.18. A microwave discharge pattern containing no nulls is evident for a longitudinal length much larger than the microwave free-space wavelength.

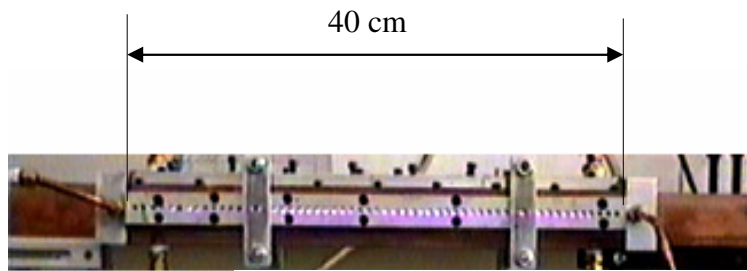


Fig. 4.18: The discharge luminescence across the laser head axis.

4.2.4.2. A 2.0 mm Discharge-Width Laser

A qualitative presentation of a single measurement point in each of this subsection proceeding graphs is presented in Fig. 4.19. It includes the magnetron high-voltage and current, the reflected and transmitted microwave wave-amplitudes, and the corresponding output laser pulse. Additional recorded data is the gas pressure and

flow-rate, the average microwave power, the cooling water temperature (at the water inlet and outlet), and the average laser power.

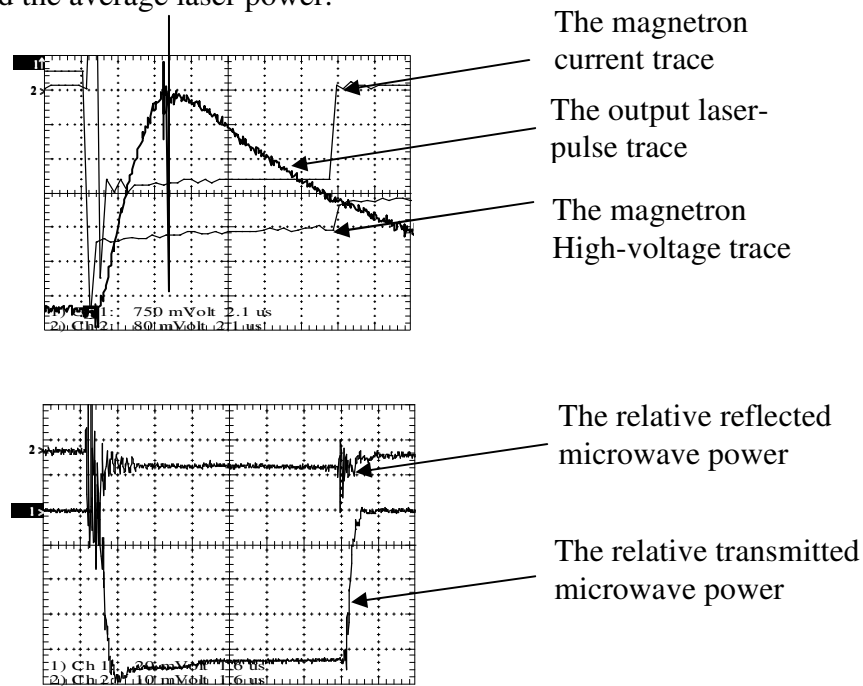


Fig. 4.19: An example of a single measurement point
(all traces except the laser pulse are negatively polarized).

Figures 4.20-4.28, present experimental results for the laser head with a 2.0 mm discharge width. Figures 4.20-4.27 show the power and efficiency measurements for 6, 10, 20, and 30 μ s pulse widths versus the pulse repetition-frequency. Figures. 4.28a, and 4.28b summarize these results. The first set of results (Figs. 4.20-4.23) is given for a gas pressure of ~ 100 Torr, and a gas flow-rate of 1.4 l/s. Figures. 4.20a-4.23a show the average and peak laser powers. Figs. 4.20b,c-23b,c show the power conversion efficiencies of the experimental setup. Figs. 4.20b-23b present the plasma, microwave, and DC to laser power conversion efficiencies. Figs. 4.20c-23c show the microwave to plasma, and DC to microwave power conversion efficiencies. The next set of results (Figs. 4.24-4.27) describe the same parametrical investigation of the laser, shown in Figs. 4.20-4.23, but the flow-rate is raised to ~ 1.8 l/s, at a pressure of 65 Torr. This setup uses an improved gas inlet and outlet as described in Appendix C.

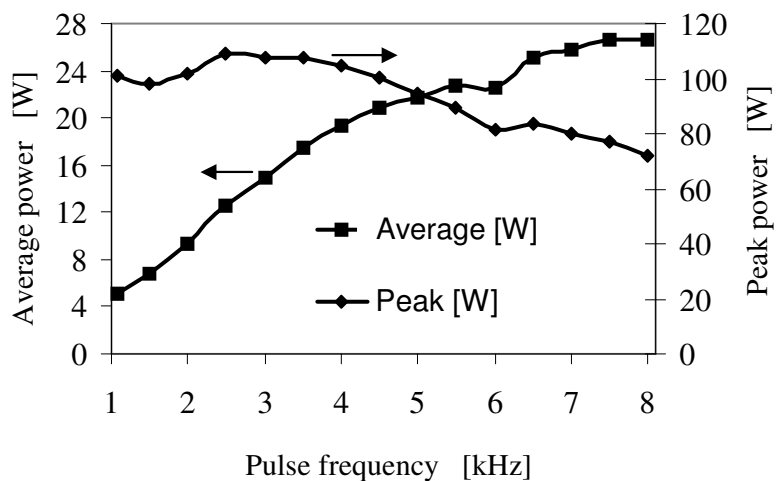


Fig. 4.20a: The average and peak laser power for a 6 μ s pulse width versus the PRF. The gas pressure is 100 Torr, and the gas flow-rate is 1.4 l/s.

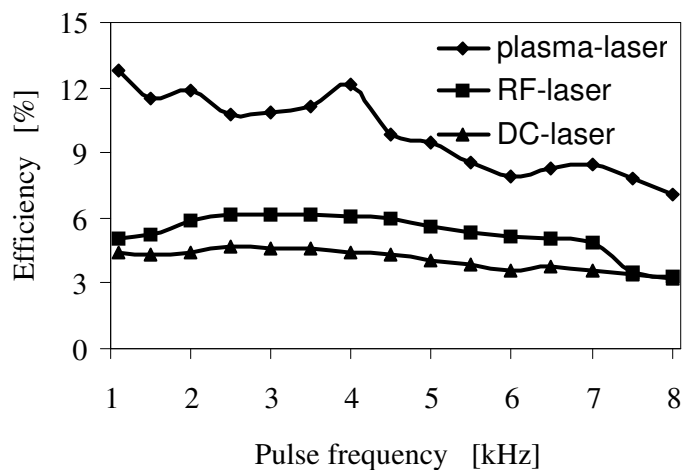


Fig. 4.20b: The plasma, microwave, and DC to laser power conversion efficiencies.

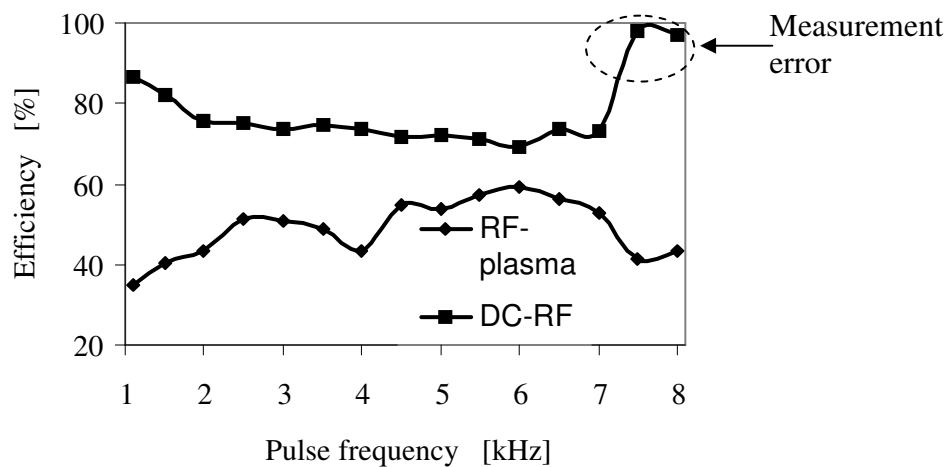


Fig. 4.20c: The microwave to plasma and DC to microwave conversion efficiencies.

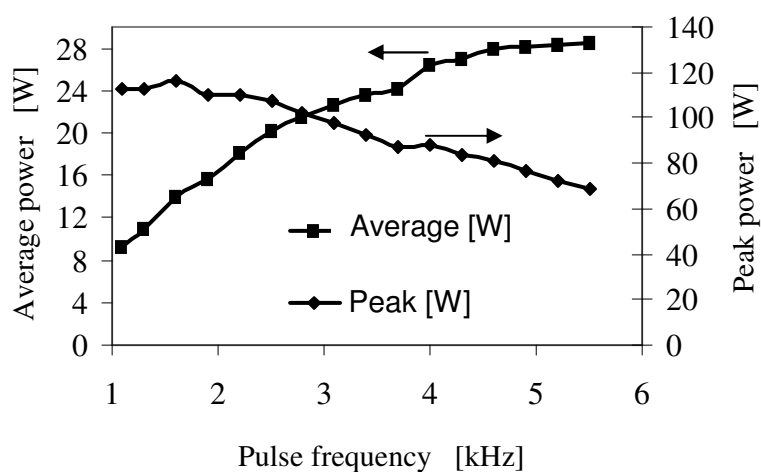


Fig. 4.21a: The average and peak laser power for a 10 μ s pulse width versus the PRF. The gas pressure is 100 Torr, and the gas flow-rate is 1.4 l/s.

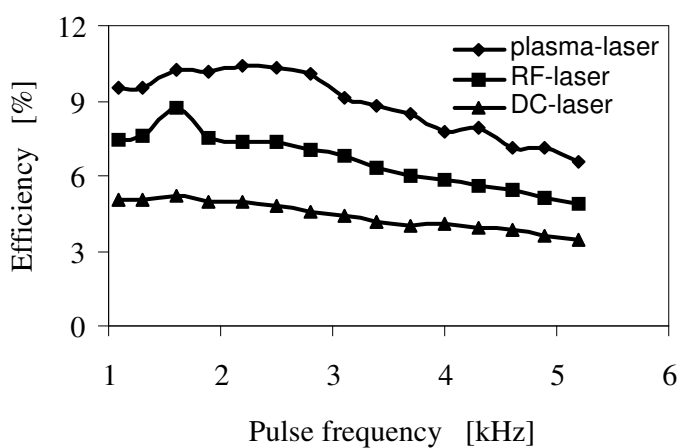


Fig. 4.21b: The plasma, microwave, and DC to laser power conversion efficiencies.

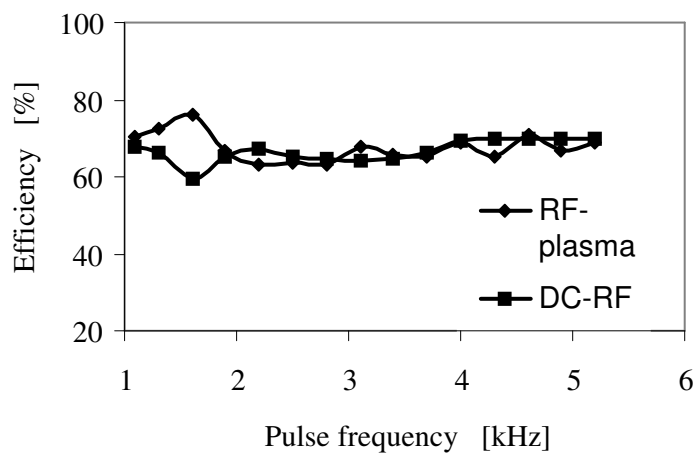


Fig. 4.21c: The microwave to plasma and DC to microwave conversion efficiencies.

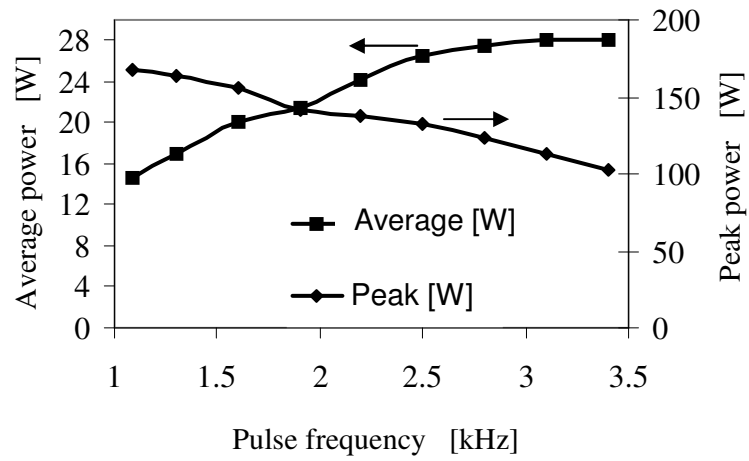


Fig. 4.22a: The average and peak laser-power for a 20 μ s pulse width versus the PRF. The gas pressure is 100 Torr, and the gas flow-rate is 1.4 l/s.

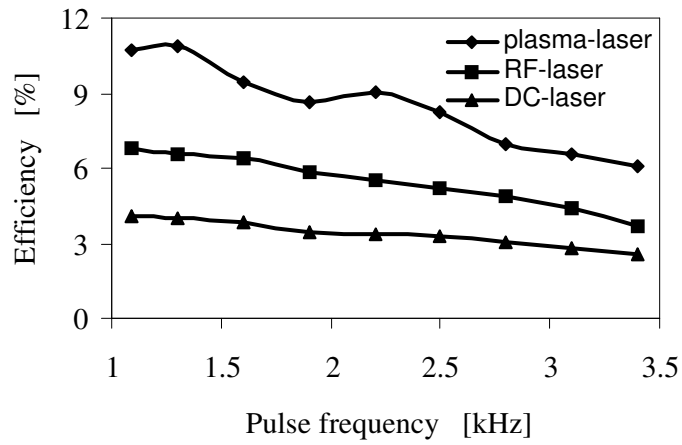


Fig. 4.22b: The plasma, microwave, and DC to laser power conversion efficiencies.

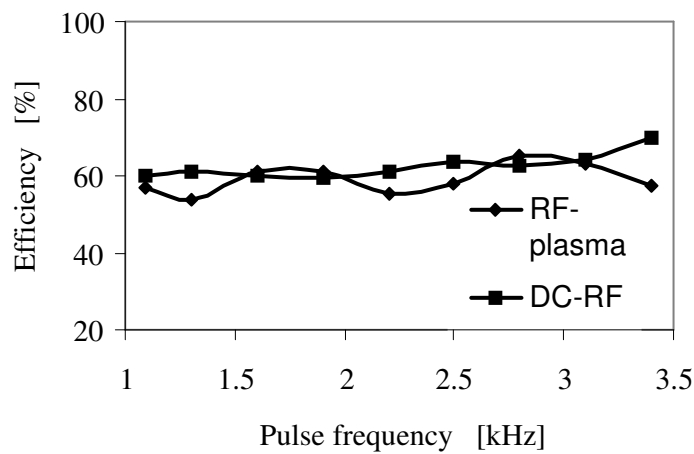


Fig. 4.22c: The microwave to plasma and DC to microwave conversion efficiencies.

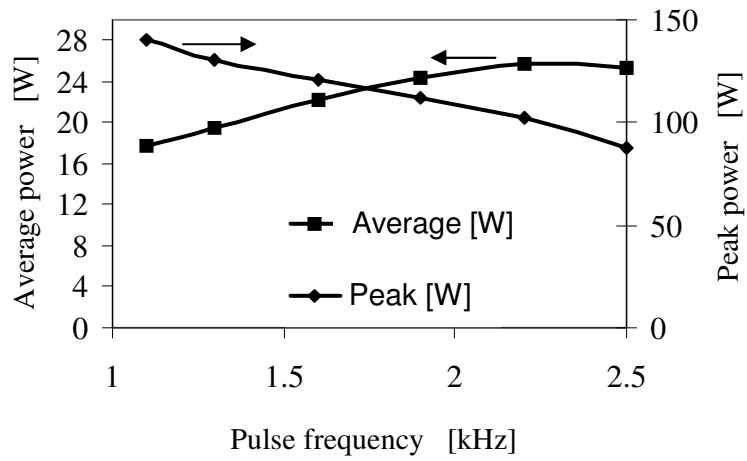


Fig. 4.23a: The average and peak laser power for a 30 μ s pulse width versus the PRF.

The gas pressure is 100 Torr, and the gas flow-rate is 1.4 l/s.

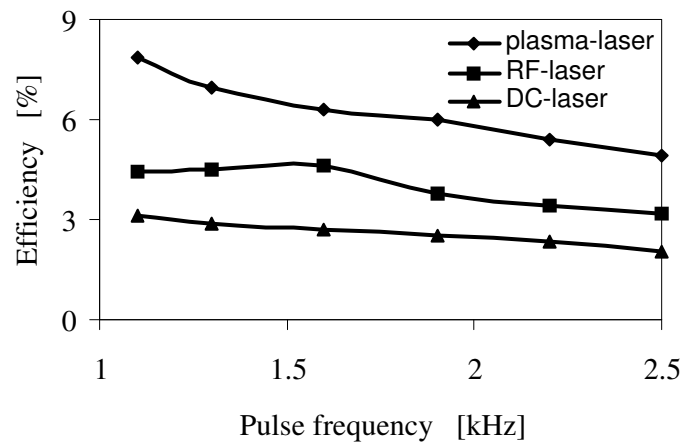


Fig. 4.23b: The plasma, microwave, and DC to laser power conversion efficiencies.

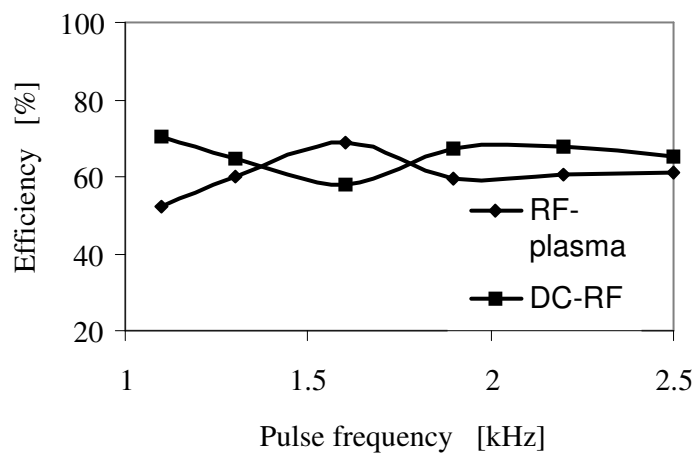


Fig. 4.23c: The microwave to plasma and DC to microwave conversion efficiencies.

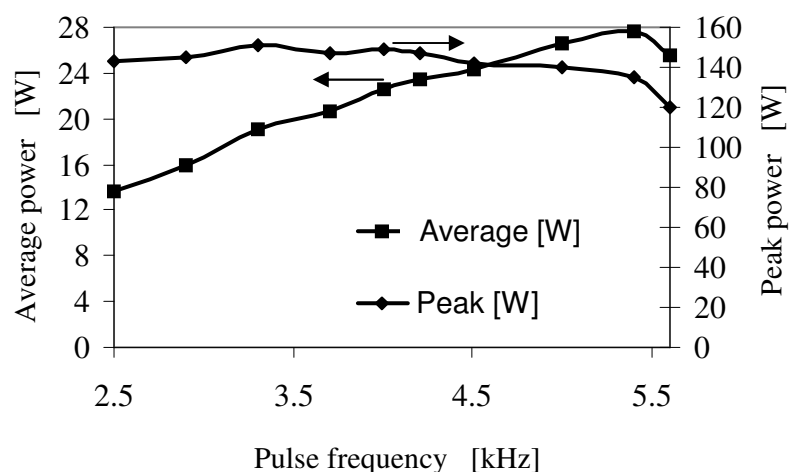


Fig. 4.24a: The average and peak laser power for a 6 μ s pulse width versus the PRF.

The gas pressure is 65 Torr, and the gas flow-rate is 1.8 l/s.

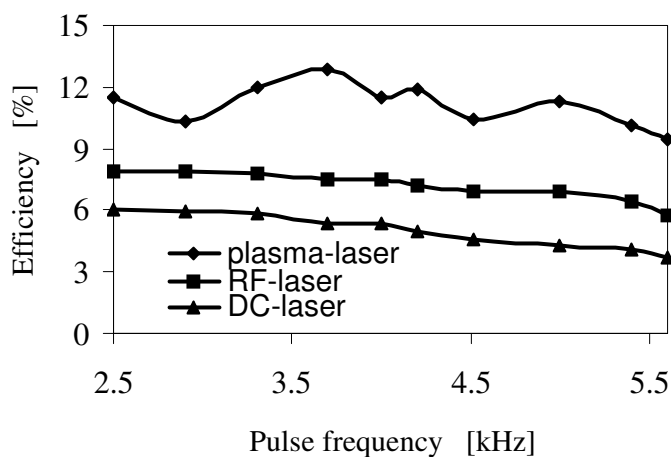


Fig. 4.24b: The plasma, microwave, and DC to laser power conversion efficiencies.

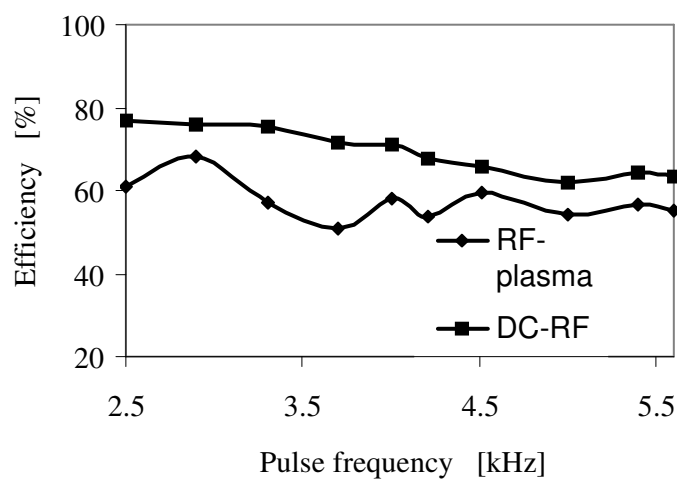


Fig. 4.24c: The microwave to plasma and DC to microwave conversion efficiencies.

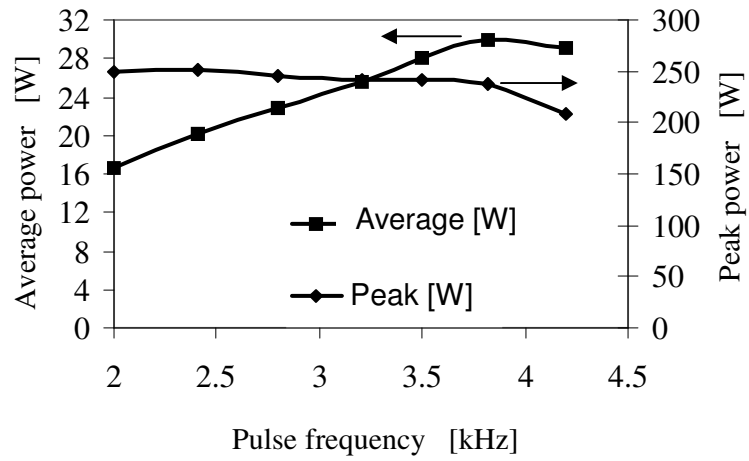


Fig. 4.25a: The average and peak laser power for a 10 μ s pulse width versus the PRF. The gas pressure is 65 Torr, and the gas flow-rate is 1.8 l/s.

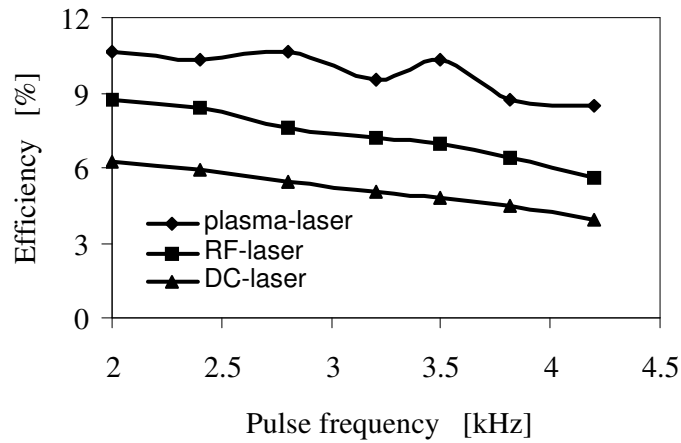


Fig. 4.25b: The plasma, microwave, and DC to laser power conversion efficiencies.

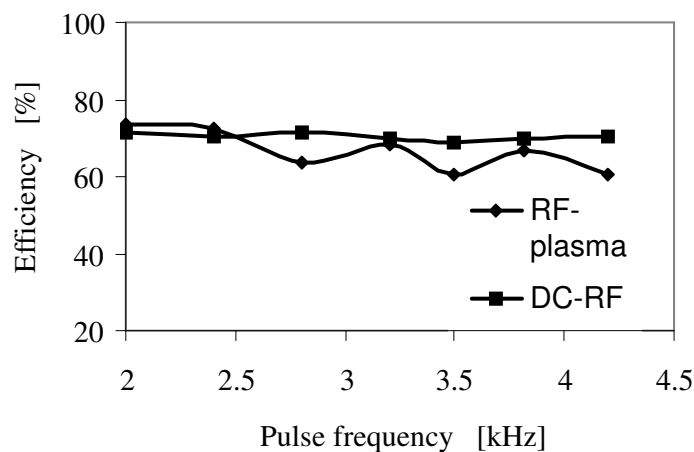


Fig. 4.25c: The microwave to plasma and DC to microwave conversion efficiencies.

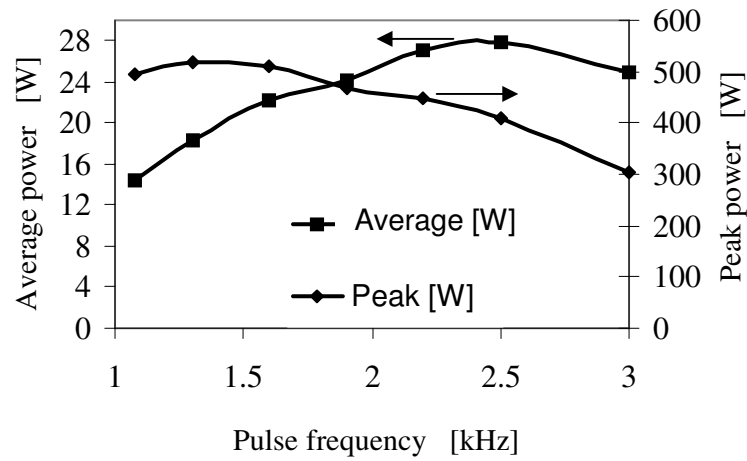


Fig. 4.26a: The average and peak laser power for a 20 μ s pulse width versus the PRF.
The gas pressure is 65 Torr, and the gas flow-rate is 1.8 l/s.

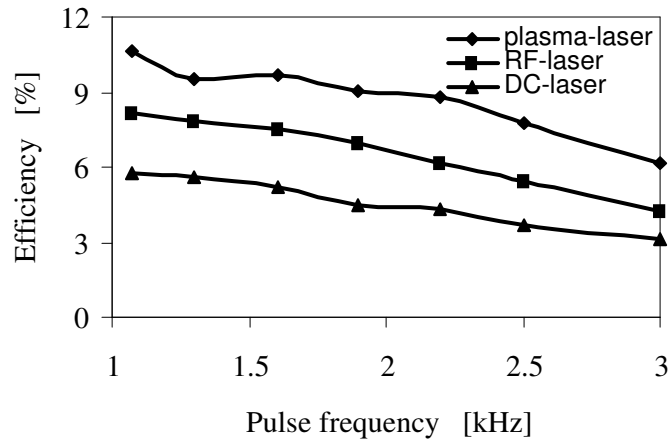


Fig. 4.26b: The plasma, microwave, and DC to laser power conversion efficiencies.

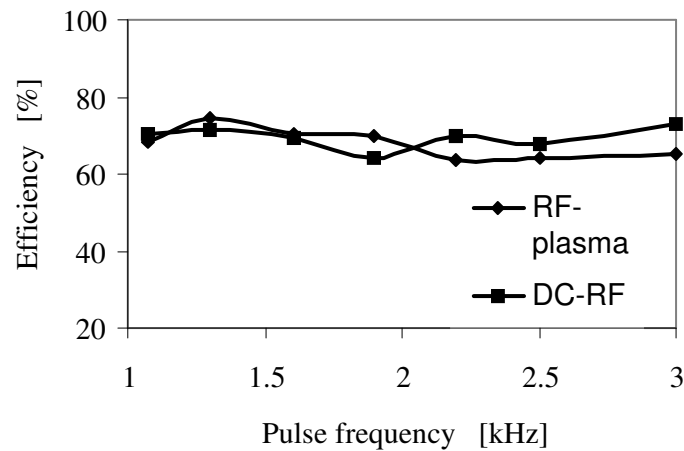


Fig. 4.26c: The microwave to plasma and DC to microwave conversion efficiencies.

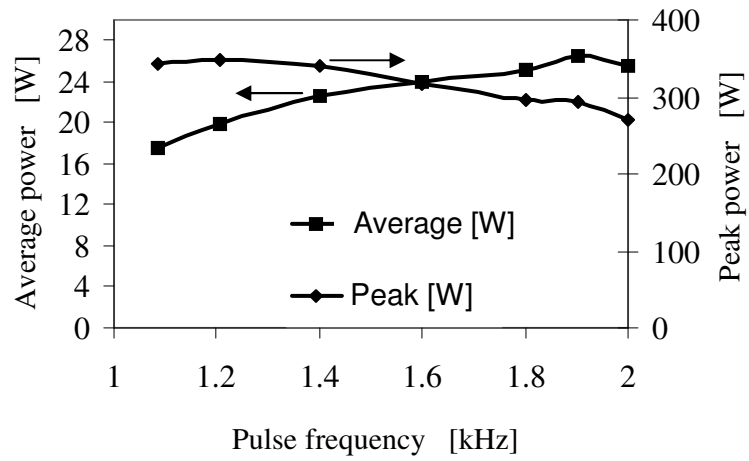


Fig. 4.27a: The average and peak laser power for a 30 μ s pulse width versus the PRF.
The gas pressure is 65 Torr, and the gas flow-rate is 1.8 l/s.

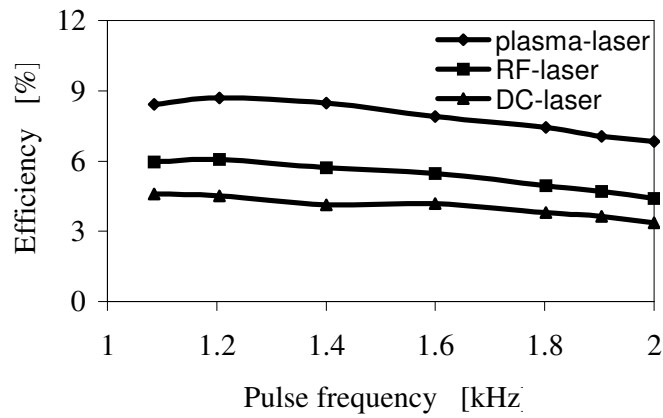


Fig. 4.27b: The plasma, microwave, and DC to laser power conversion efficiencies.

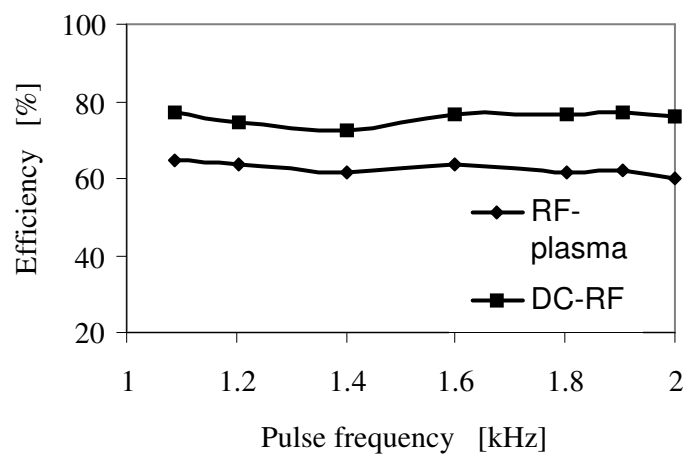


Fig. 4.27c: The microwave to plasma and DC to microwave conversion efficiencies.

Figures 4.28a and 4.28b summarize the measurements of the average and peak laser powers for three gas flow-rates, namely, 1.4, 1.8, and 2.0 l/s. The corresponding gas pressures are 100, 65, and ~ 40 Torr, respectively. The results are given for a 20 μ s pulse-width in which the maximal peak and average powers are achieved.

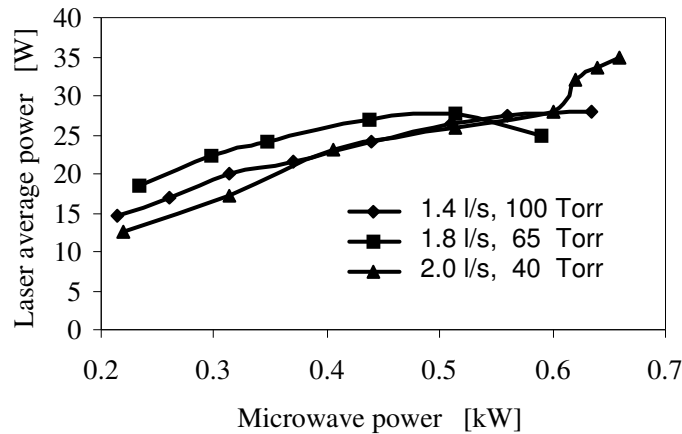


Fig. 4.28a: The average laser-power versus the microwave power for three gas flow-rates.

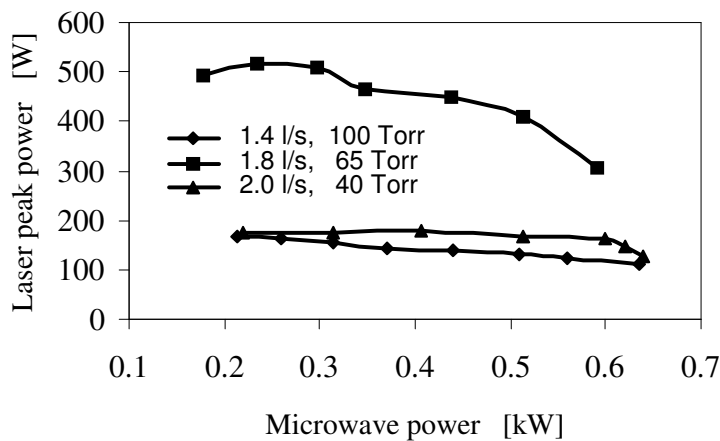


Fig. 4.28b: The peak laser-power versus the microwave power for three gas flow-rates.

The maximal laser powers for the 2.0 mm discharge width are as follows: an average laser power of ~ 36 W is measured at a microwave pulse width and repetition frequency of 20 μ s and 3.3 kHz, respectively. The corresponding laser pulse width is 93.7 μ s. A peak laser power of ~ 520 W is measured at a microwave pulse width and repetition frequency of 20 μ s and 1.3 kHz, respectively. The corresponding laser pulse width for this measurement is 27.3 μ s.

4.2.4.3. A 1.5 mm Discharge-Width Laser

This section presents the laser experimental results for a 1.5 mm discharge width. The results are presented in the same format as in the previous section. The first two set of results (Figs. 4.29-4.32, and Figs. 4.33-4.36) present the laser average and peak powers, and the setup efficiencies for 6, 10, 20, and 30 μs pulse widths. All the results are shown versus the pulse repetition-frequency. Figures 4.29-4.32 describe experiments conducted at a pressure of ~ 70 Torr and a gas flow-rate of 0.4 l/s. Figures 4.33-4.36 describe experiments conducted at a pressure of 50 Torr and a gas flow-rate of 1.1 l/s, which is the maximal attained for the 1.5 mm discharge width. The laser average and peak powers are presented in Figs. 4.29a-4.36a. The plasma-to-laser, microwave-to-laser, and DC-to-laser power conversion-efficiencies are presented in Figs. 4.29b-4.36b. Figures 4.29c-4.36c show the DC-to-microwave and microwave-to-plasma power conversion efficiencies.

Figures 4.37a and 4.37b summarize the results of the laser average and peak powers. Laser power is detected versus the input microwave power, for three gas flow-rates, namely, 0.4, 0.85, and 1.1 l/s. This summary is given for the optimal pulse widths, in which the maximal average and peak powers are measured for each flow rate. The optimal pulse width for 0.4, and 1.1 l/s flow rates is 10 μs , and for the 0.85 l/s it is 20 μs . The optimal pulse width for the peak laser power measurements is 20 μs .

The maximal laser powers for the 1.5 mm discharge width are as follows. An average laser power of ~ 40 W is measured at a microwave pulse width and repetition frequency of 10 μs and 6.0 kHz, respectively. A peak laser power of 575 W is measured at a microwave pulse width and repetition frequency of 20 μs and 1.0 kHz, respectively. The measured laser pulse width corresponding to both measurements is 35 μs .

The succeeding sections present the laser small signal gain, and the beam quality for the two discharge widths (2 and 1.5 mm). The output coupler optimization and beam quality measurements are also given. The experimental setups in which these measurements are taken are described.

A comprehensive discussion of the laser results will follow in the next Chapter.

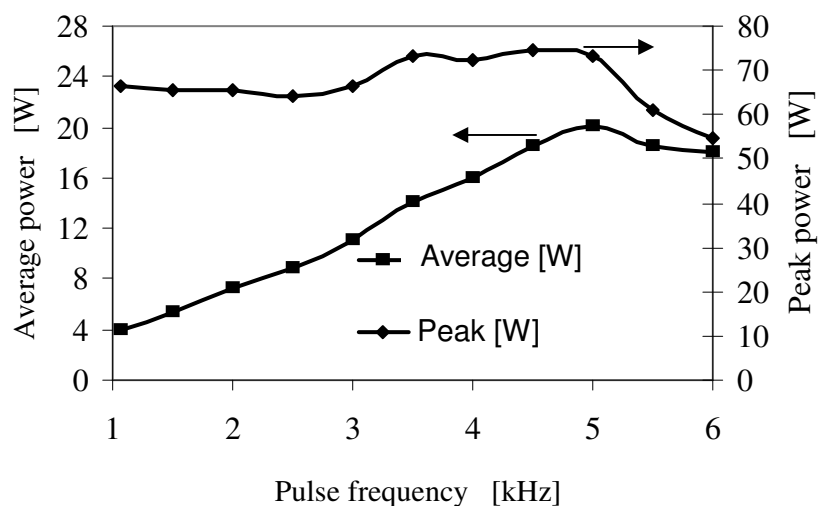


Fig. 4.29a: The average and peak laser power for a 6 μ s pulse width versus the PRF.

The gas pressure is 70 Torr, and the gas flow-rate is 0.4 l/s.

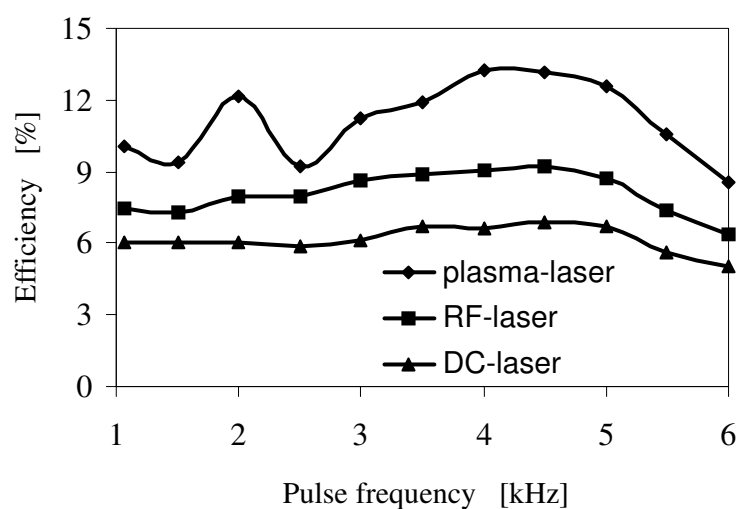


Fig. 4.29b: The plasma, microwave, and DC to laser power conversion efficiencies.

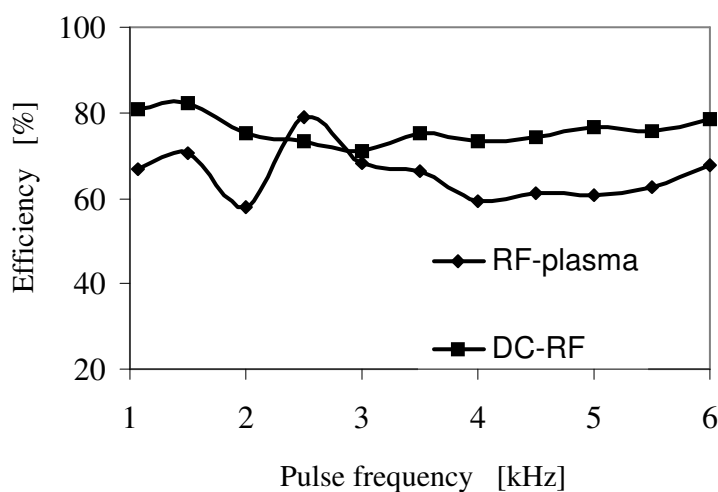


Fig. 4.29c: The microwave to plasma and DC to microwave conversion efficiencies.

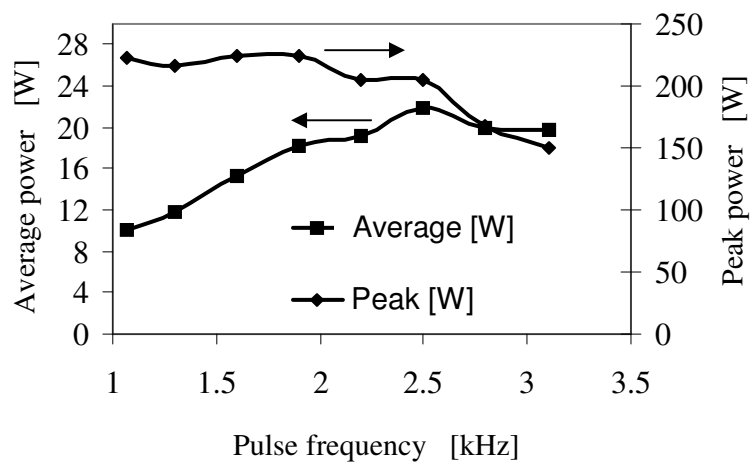


Fig. 4.30a: The average and peak laser power for a 10 μ s pulse width versus the PRF.

The gas pressure is 70 Torr, and the gas flow-rate is 0.4 l/s.

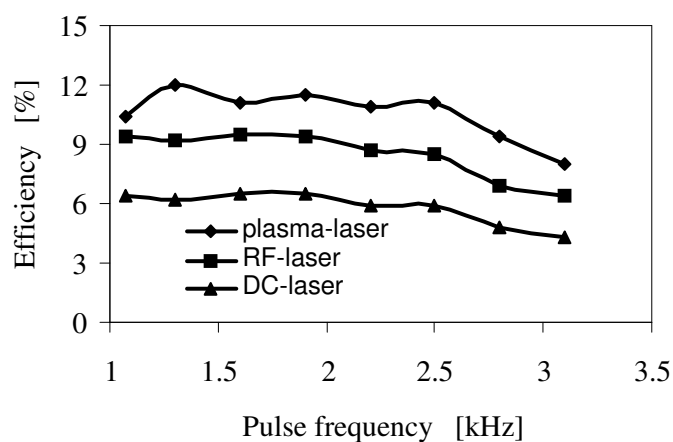


Fig. 4.30b: The plasma, microwave, and DC to laser power conversion efficiencies.

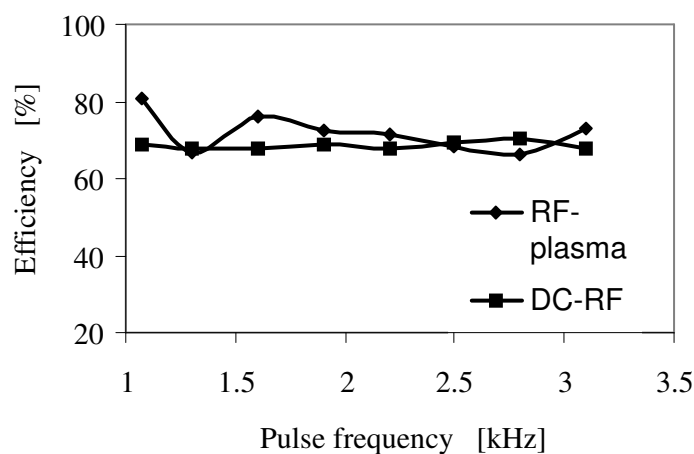


Fig. 4.30c: The microwave to plasma and DC to microwave conversion efficiencies.

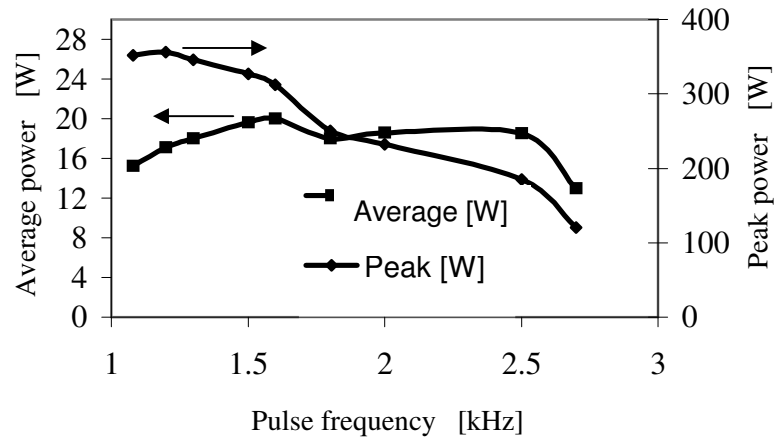


Fig. 4.31a: The average and peak laser power for a 20 μ s pulse width versus the PRF.
The gas pressure is 70 Torr, and the gas flow-rate is 0.4 l/s.

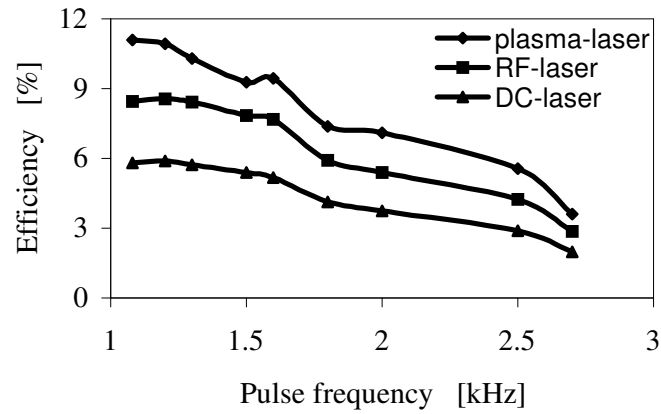


Fig. 4.31b: The plasma, microwave, and DC to laser power conversion efficiencies.

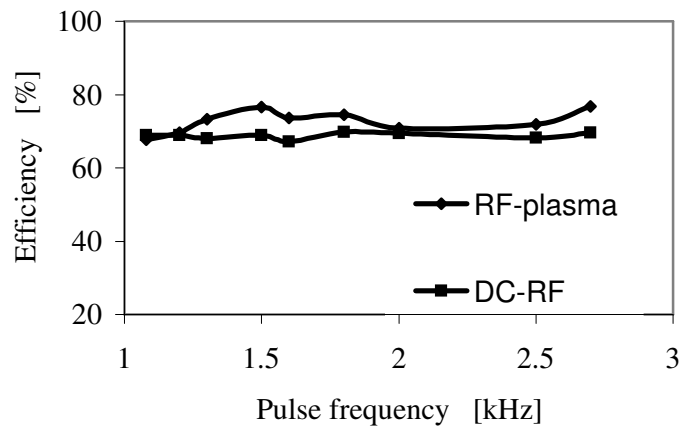


Fig. 4.31c: The microwave to plasma and DC to microwave conversion efficiencies.

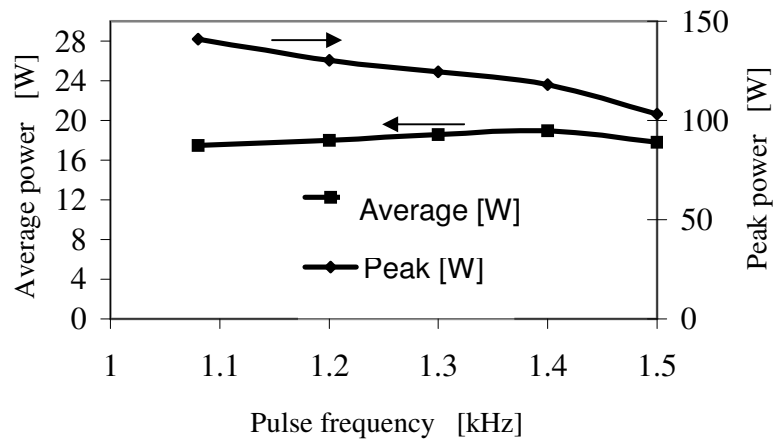


Fig. 4.32a: The average and peak laser power for a 30 μ s pulse width versus the PRF.
The gas pressure is 70 Torr, and the gas flow-rate is 0.4 l/s.

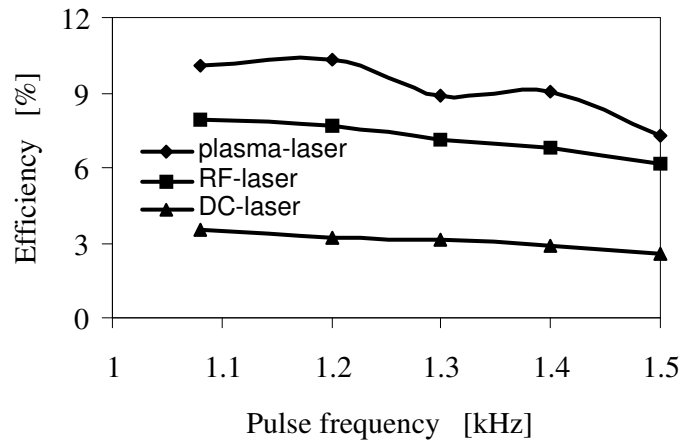


Fig. 4.32b: The plasma, microwave, and DC to laser power conversion efficiencies.

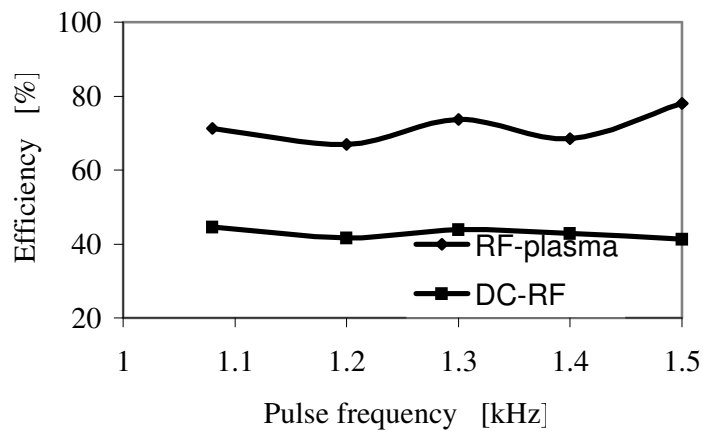


Fig. 4.32c: The microwave to plasma and DC to microwave conversion efficiencies.

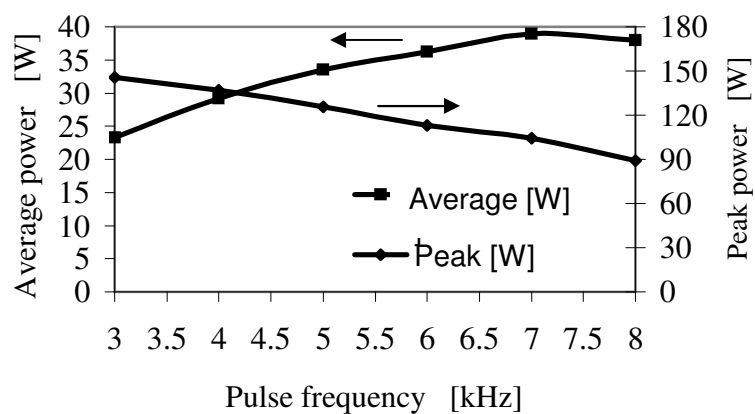


Fig. 4.33a: The average and peak laser power for a 6 μ s pulse width versus the PRF.
The gas pressure is 50 Torr, and the gas flow-rate is 1.1 l/s.

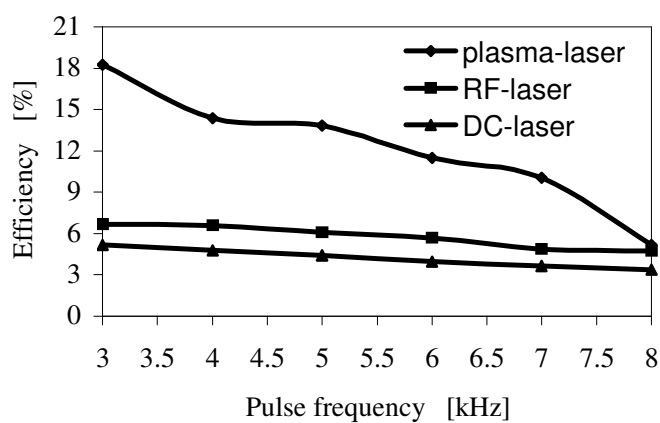


Fig. 4.33b: The plasma, microwave, and DC to laser power conversion efficiencies.

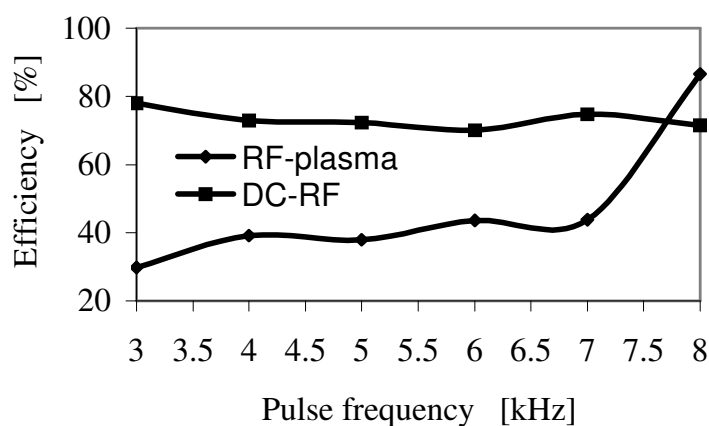


Fig. 4.33c: The microwave to plasma and DC to microwave conversion efficiencies.

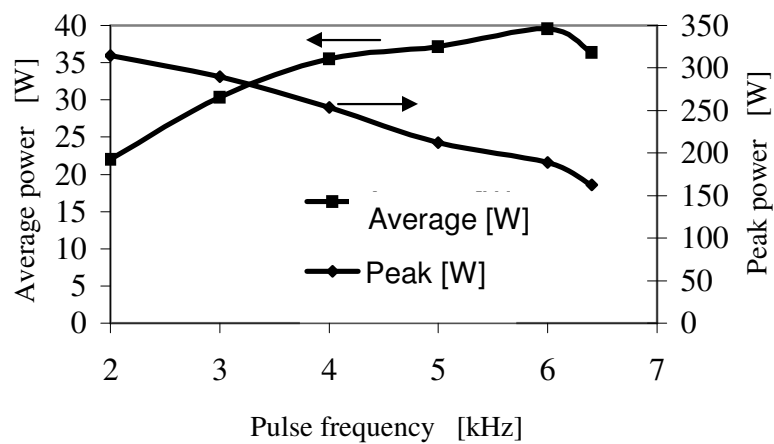


Fig. 4.34a: The average and peak laser power for a 10 μ s pulse width versus the PRF.
The gas pressure is 50 Torr, and the gas flow-rate is 1.1 l/s.

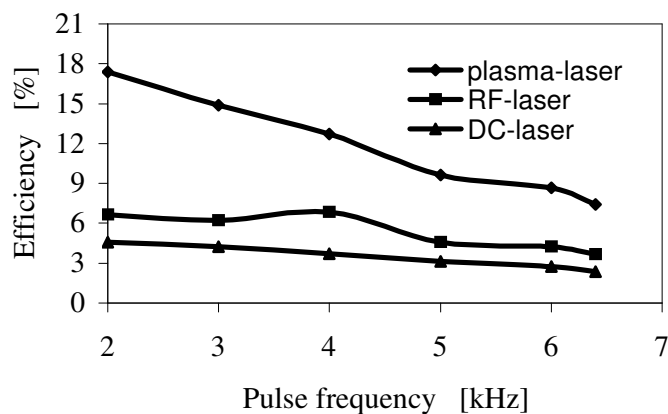


Fig. 4.34b: The plasma, microwave, and DC to laser power conversion efficiencies.

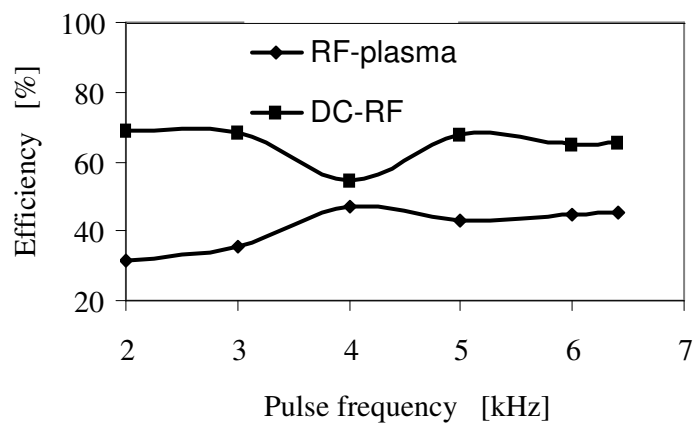


Fig. 4.34c: The microwave to plasma and DC to microwave conversion efficiencies.

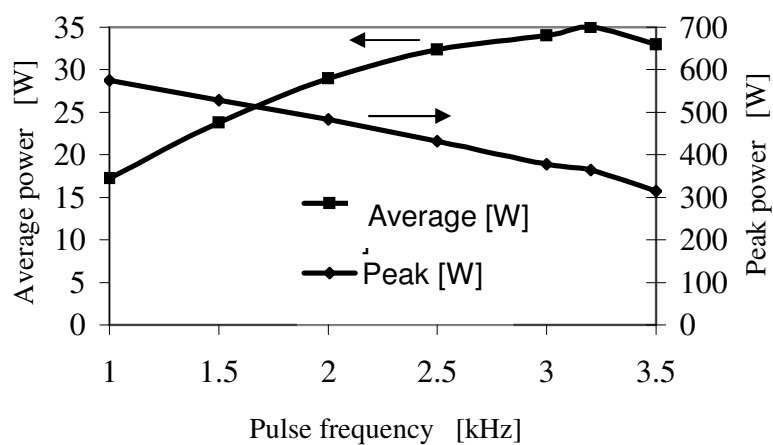


Fig. 4.35a: The average and peak laser power for a 20 μ s pulse width versus the PRF.

The gas pressure is 50 Torr, and the gas flow-rate is 1.1 l/s.

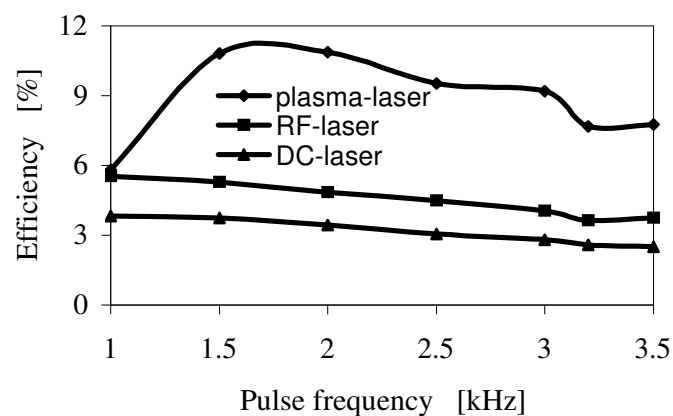


Fig. 4.35b: The plasma, microwave, and DC to laser power conversion efficiencies.

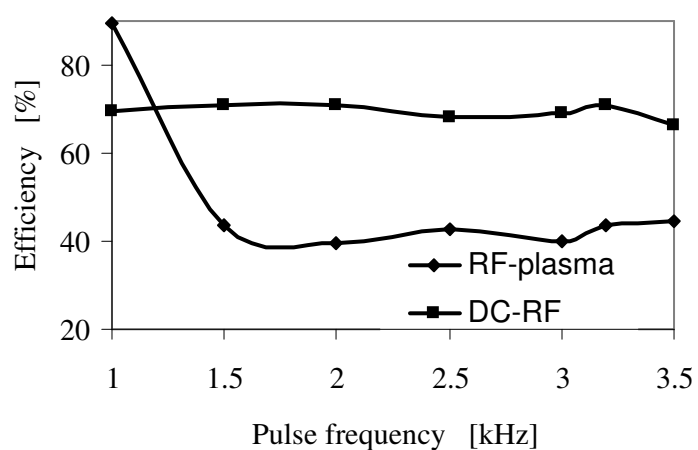


Fig. 4.35c: The microwave to plasma and DC to microwave conversion efficiencies.

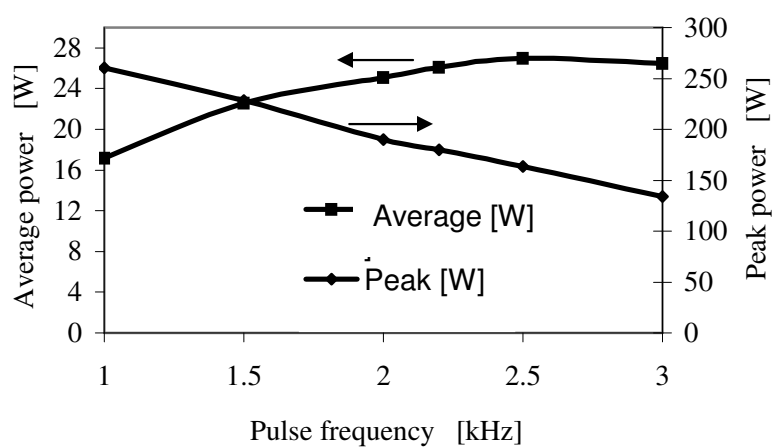


Fig. 4.36a: The average and peak laser power for a 30 μ s pulse width versus the PRF.

The gas pressure is 50 Torr, and the gas flow-rate is 1.1 l/s.

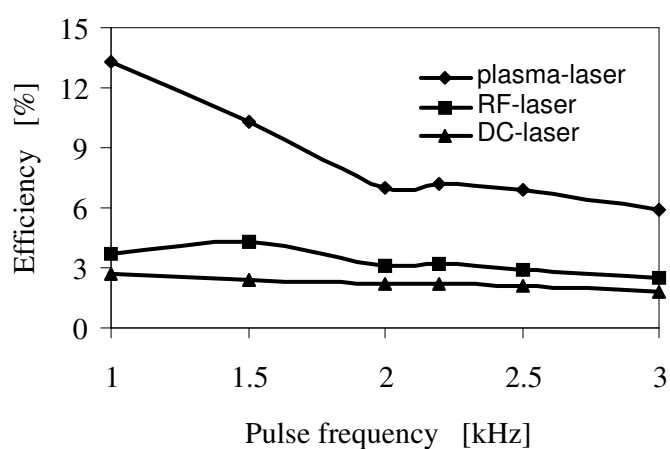


Fig. 4.36b: The plasma, microwave, and DC to laser power conversion efficiencies.

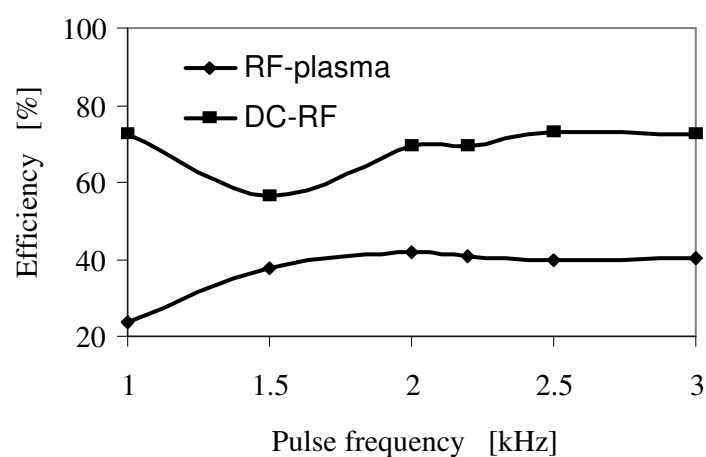


Fig. 4.36c: The microwave to plasma and DC to microwave conversion efficiencies.

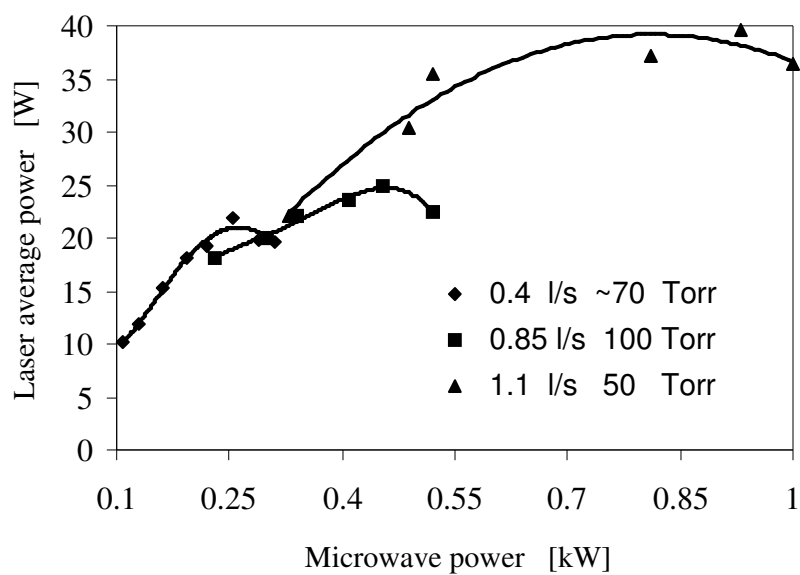


Fig. 4.37a: The average laser-power versus the input microwave power for three gas flow-rates. The pulse width for these measurements is 10 μ s.

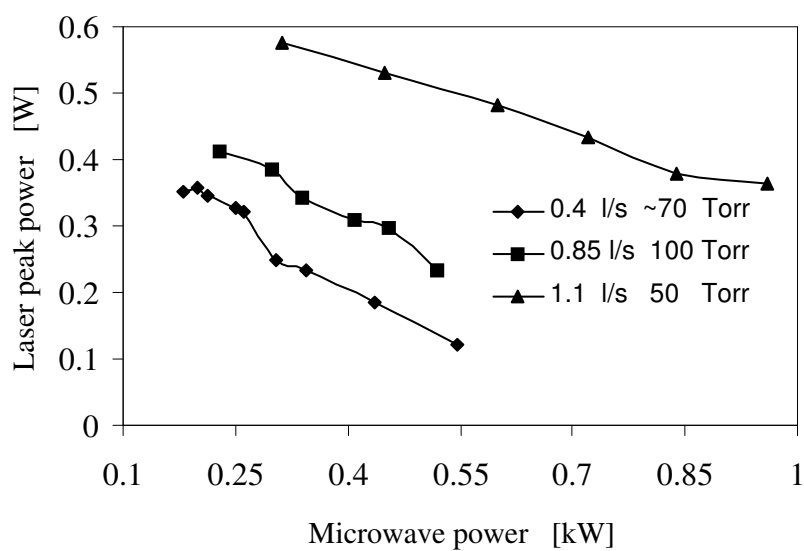


Fig. 4.37b: The peak laser-power versus the input microwave power for three gas flow-rates. The pulse width for these measurements is 20 μ s.

4.2.4.4. Laser Output-Pulse Measurements

This subsection presents the measured laser pulses, for the two investigated discharge widths (1.5 and 2.0 mm), at 6, 10, 20, and 30 μs microwave pulse widths. The laser pulse-widths are measured at the regime of operation yielding the maximal peak laser power for each discharge width. The optimal gas-pressure and flow rate, for the 2.0 mm discharge width, are 40 Torr, and 1.8 l/s. For the 1.5 mm, the pressure and flow rate are 50 Torr and 1.1 l/s respectively. Figures 4.38 and 4.39 present the laser pulse (Channel 1) and the reflected microwave-signal amplitude (Channel 2) traces, for the 2 and 1.5 mm discharge widths, respectively. The pulse widths are summarized in Table 4.3. As evident in Table 4.3, the pulse widening is minimal around a 20 μs microwave pulse-width for both the discharge widths. Therefore, the optimal reduced-field (E/N) is achieved for this pulse width. These results indicate a maximal exploitation of the population inversion for the 20 μs pulse width, due to an optimal operation regarding the gas temperature, as explained in Section 1.2.3. The increased pulse widening for the 6 and 30 μs pulse widths (for both discharge widths) indicates a deviation from the optimal discharge reduced-field due to the increased steady-state gas temperature, as will be further discussed.

Table 4.3 shows that the pulse widening is increased for the 1.5 mm discharge width compared to the 2.0 mm discharge width. This can be attributed to the larger pulse temperature-rise for this discharge width. This is shown using a thermal investigation of the laser head in the next Chapter.

Microwave pulse width [μs]	Laser pulse-width [μs]	
	2.0 mm discharge width	1.5 mm discharge width
6	38	53.3
10	45	35
20	27.3	30
30	47.3	66

Table 4.3: The laser pulse widening for the two discharge widths
(see Figs. 4.38, and 4.39).

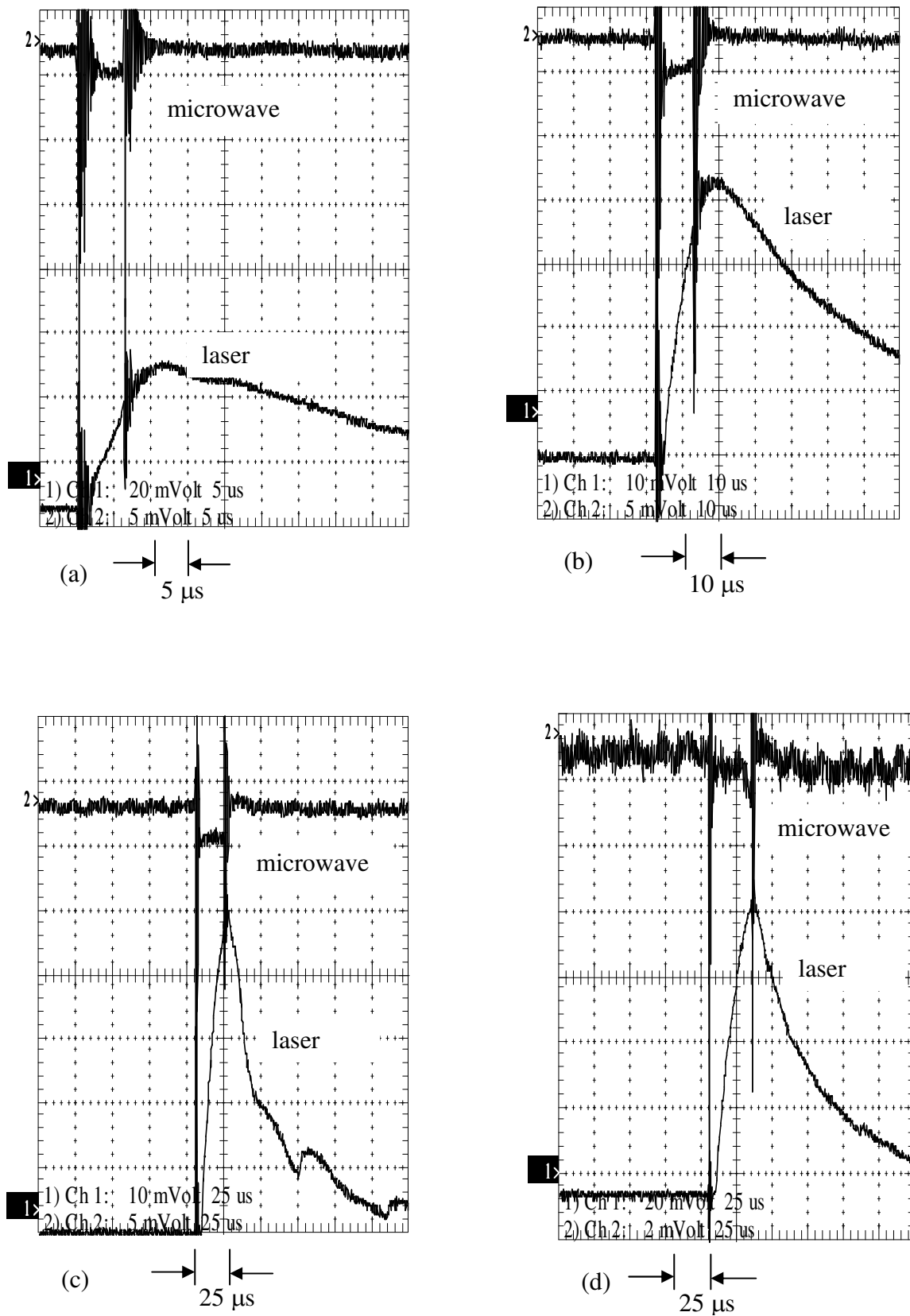


Fig. 4.38: The laser pulse for 6, 10, 20, and 30 μ s (a, b, c, and d, respectively) pulse widths for the 2.0 mm discharge width. Trace 2 represents the detected reflected microwave power, and specifies the power pulse temporal boundaries.

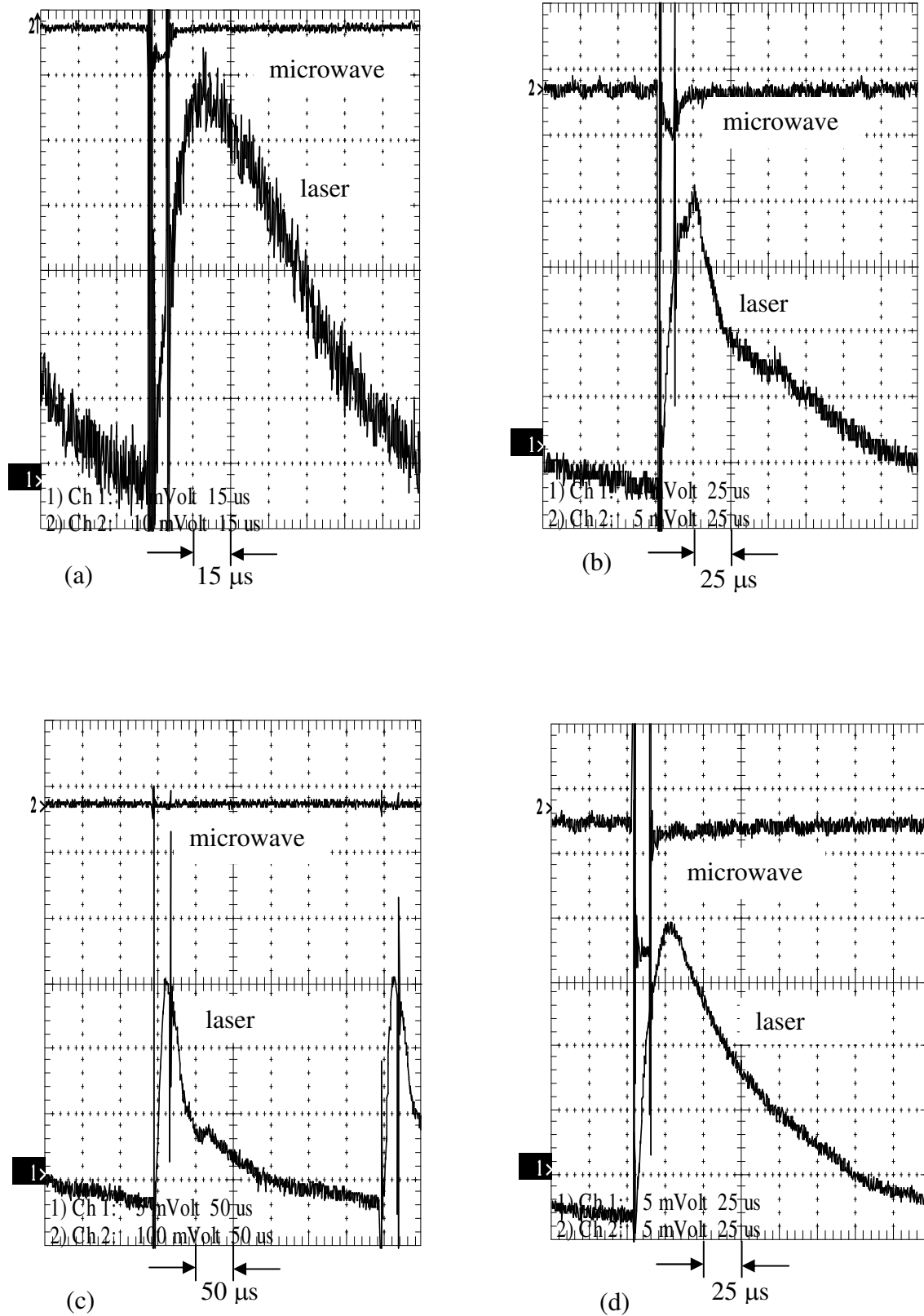


Fig. 4.39: The laser pulse for 6, 10, 20, and 30 μ s (a, b, c, and d, respectively) pulse widths for the 1.5 mm discharge width. Trace 2 represents the detected reflected microwave power, and specifies the power pulse temporal boundaries.

4.2.4.5. Small Signal Gain Measurements

The experimental setup for the small signal gain measurements is described in Fig. 4.40.

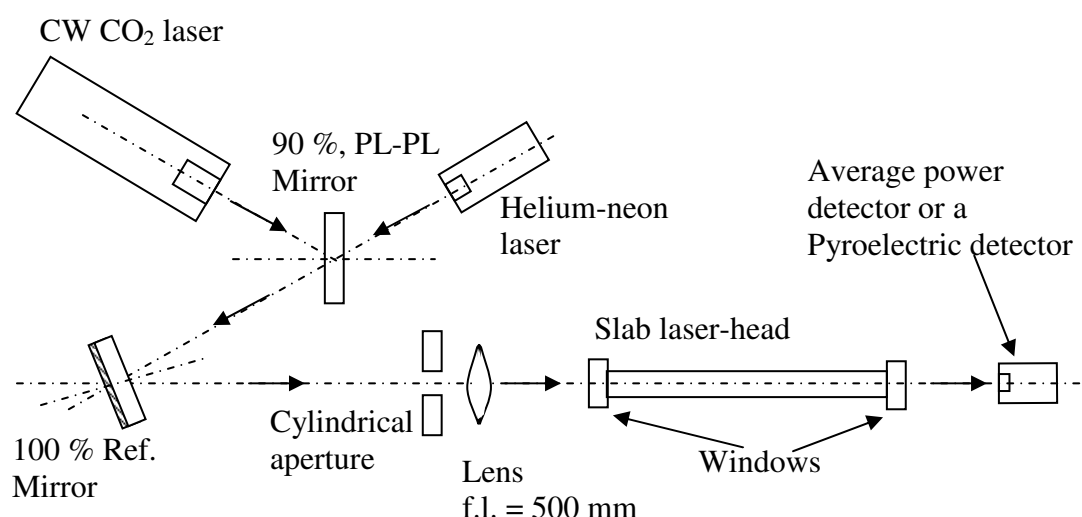


Fig. 4.40: The small signal gain measurement setup.

A Ferranti CM2044 CW CO₂ laser supplies the input power to the slab laser-head serving as an amplifier. The CW laser power is aligned on the axis of the slab laser with the use of a co-aligned Uniphase 1507-0 helium-neon laser. The input power is delivered through a cylindrical aperture and a lens (focal length = 500 mm) to the slab laser-head. Zinc-Selenide windows are located at both ends of the discharge chamber. The laser is operated in several pulse-widths for a variable pulse repetition-frequency. A thermal detector measures the average output-power. The output laser-pulse shape measured by a fast pyroelectric detector is used to accurately estimate the peak laser power. The small signal gain is deduced from (a) the average output-power with and without the presence of a discharge; (b) the pulse repetition-frequency, and (c) the amplified output laser pulse shape. Figures 4.41a and 4.41b present the small signal gain for the 2.0 and 1.5 mm discharge widths.

The small signal gain is used to determine the optimal output-coupler for the two discharge widths.

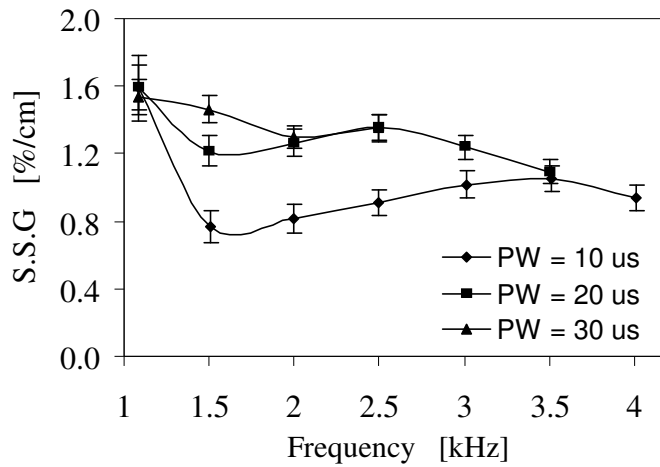


Fig. 4.41a: The small signal gain for a 2.0 mm discharge width for three microwave pulse widths (10, 20, and 30 μs) versus the pulse repetition frequency.

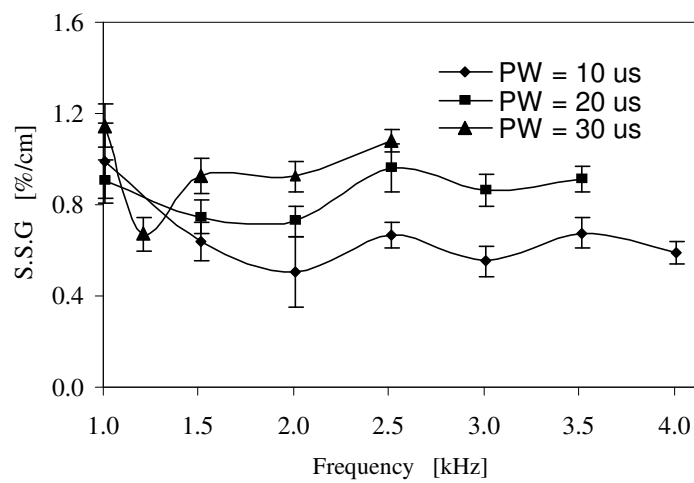


Fig. 4.41b: The small signal gain for a 1.5 mm discharge width for three microwave pulse widths (10, 20, and 30 μs) versus the pulse repetition frequency.

4.2.4.6. Output (Laser) Coupler Optimization

The optical losses in a slab laser result from wave guiding, diffraction, and output coupling. The wave-guiding loss in a waveguide consisting of two Pyrex slabs for the TE₁₀ laser-mode is [63]

$$\alpha_w(d, \epsilon_d) = \frac{\lambda^2}{8d^3} \operatorname{Re} \left\{ \frac{1}{\sqrt{\epsilon_d - 1}} \right\}. \quad (47)$$

d is the waveguide height, λ is the laser wavelength, and ϵ_d is the complex dielectric-constant of the Pyrex at 10.6 μm . The glass refractive-index is $n_g \equiv \sqrt{\epsilon_d} \cong 2.1 - j1.2$ [63], and d (the discharge width) is 2.0 or 1.5 mm.

The diffraction losses are calculated by [64]

$$\Gamma_d = 65.4 \left(\frac{z\lambda}{1.3d^2} \right)^{3/2} \quad [\%] \quad (48)$$

where z is the distance between the waveguide and the mirror.

Assuming that the diffraction losses are equal at both ends of the optical resonator, the round-trip loss is given by

$$\alpha_T = \alpha_w - \frac{\ln(1 - \Gamma_d/100)}{L} \quad (49)$$

where L is the waveguide length. The power-density emitted from the output coupler is [78]

$$I_{\text{out}} = I_{\text{sat}} T \left[\frac{2L\gamma_0}{2L\alpha_T - \ln(1 - T)} - 1 \right], \quad (50)$$

where T is the transmission of the output-coupler, I_{sat} is the saturation power-density, and γ_0 is the small signal gain.

Figures 4.42a and 4.42b depict the calculated results for the laser normalized output power-flux. Experimental results are presented for three different output couplers (80 %, 85 %, and 90 % reflectance) considering the measured small-signal gain. Each figure presents two traces. One calculation is performed for a setup that uses windows attached to the Pyrex waveguide and external mirrors. In the second setup, the mirrors are attached directly to the waveguide, hence, the diffraction losses are avoided. The optimal reflection for each setup is indicated.

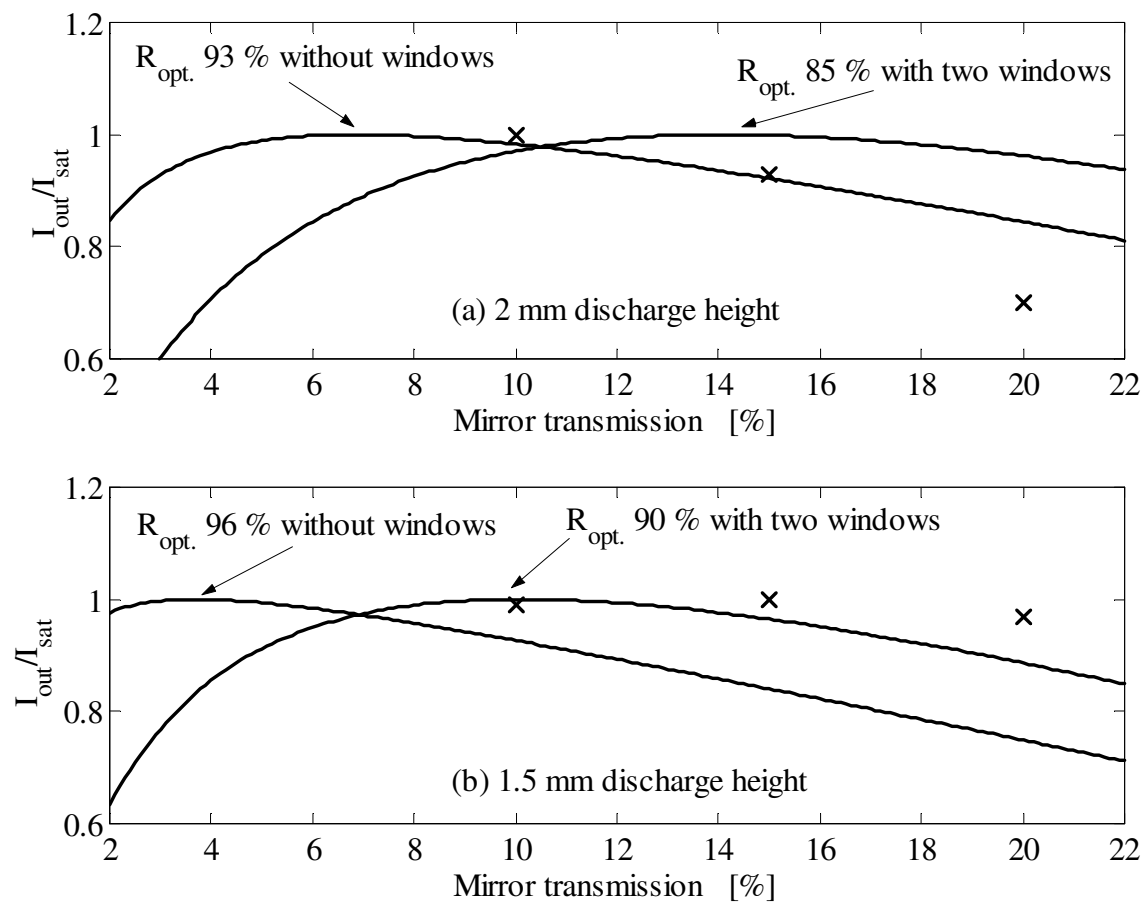


Fig. 4.42: The normalized laser power-density dependence on the output coupler, for (a) a 2.0 mm, and (b) a 1.5 mm discharge width. The traces present a calculation for two setups, and the **x** marks represent the experimental results.

The optimal output-coupler reflection for the 2.0 mm discharge width is 85 %, for an optical setup including windows, and 93 % when windows are excluded, as explained above. The optimal output-coupler reflection for the 1.5 mm discharge width is 90 %, for an optical setup including windows, and 96 % when windows are excluded.

4.2.4.7. Beam Quality Measurements

The beam quality measurement setup is described in Fig. 4.43. A lens with a focal length of 100 mm is placed next to the laser output-coupler. A knife-edge aperture attached to an x-y-z translation stage is placed at the lens focal point. An average power detector is placed after the aperture.

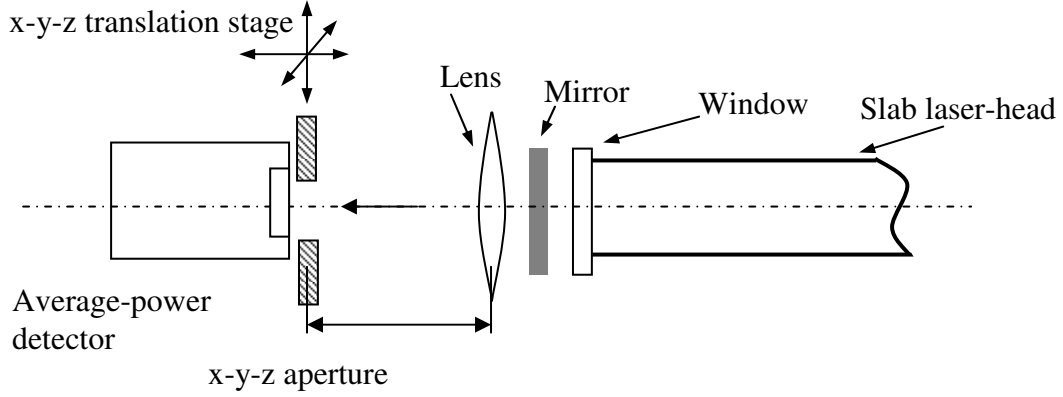


Fig. 4.43: The beam quality measurement setup.

The measurement of the beam quality (M^2) is performed in the following way: the aperture is opened to its maximum, allowing the full beam cross-section to reach the detector. The power reaching the detector can be reduced to 0.86 of the full beam power at its waist, by the z and x or y translation. The beam divergence (θ) is calculated by

$$\theta = \frac{\lambda 4}{d\pi}. \quad (51)$$

The beam quality (M^2) is defined as

$$M^2 = \frac{\theta'}{\theta}, \quad (52)$$

where θ' is defined as $\theta' = d'/f$, for a slit width of d' and a focal length of f .

The y-axis beam quality for the 2.0 and 1.5 mm discharge widths is $M_y^2 = 3.41$, and $M_y^2 = 2.41$, respectively. The x-axis beam quality for the 2.0 and 1.5 mm discharge widths is ~ 80 , and 75 , respectively, due to the multi-mode operation of the waveguide.

4.2.5. Sealed Microwave-Excited CO₂ Slab-Laser

Microwave excitation of CO₂ lasers is inherently pulsed, as explained in Chapter 3. Besides the increased thermal instabilities of microwave excited CO₂ lasers, the high peak-power microwave-pulses deteriorate the laser gas mixture. The pulsed operation regime often dictates a large reduced-field (E/N), which enhances the gas dissociation and instabilities. In sealed microwave-excited devices, the enlarged dissociation degrades the laser performance significantly, since the gas is stagnant and not refreshed as in slow-flow schemes.

The sealed CO₂ laser operation-advantages are: (1) compact schemes with cheaper operation, (2) reduced overhead, and (3) possible use of exotic gas mixtures. Various works describe the chemical processes taking place in a sealed CO₂-laser, and offer improvements for these devices [79-82]. Sintov *et al* [33] have demonstrated the operation of a microwave-excited sealed CO₂ slab-laser. Nevertheless, no basic research is found in the CO₂ laser literature, devoted to the subject of sealed operation of microwave-excited CO₂ lasers.

Experimental results for a sealed microwave-excited CO₂ slab-laser are presented in this subsection. The sealed tube is described in detail in Appendix C. It uses a 2.0 mm discharge width and 80 cm² discharge area. The laser head microwave resonator resembles that of the slow flow schemes (see Table 4.2).

The basic gas mixture used for the sealed operation is composed of 17.5 % of N₂, 6 % of CO₂, 2 % of Xe, 0.9 % of CO, 0.2 % of H₂, and 73.4 % of He. An optimization of the Xe percentage was performed. The additional mixture elements, compared to other customary mixtures, are used to enhance the dissociated CO₂-molecules recombination, and to lower the average ionization energy of the gas [78,79]. Thus, a more efficient vibrational excitation of the CO₂ molecules is attained.

4.2.5.1. Experimental Results

The maximal average and peak powers measured for the sealed tube are 13 W and ~ 210 W, respectively. These results were measured for a microwave pulse width and repetition frequency of 11.5 μ s and 1.7 kHz, respectively, at a gas pressure of 95 mbar, and a mixture with a 2 % of Xe. The average microwave power is 335 W,

corresponding to a microwave to laser-power conversion efficiency of $\sim 4\%$. A 5% decrease in the peak laser power is observed after a two-hour operation.

Fig. 4.44 shows the average and peak laser powers versus the gas mixture Xe percentage. All measurements are performed for microwave pulse widths of $9\text{--}12\ \mu\text{s}$, pulse repetition frequencies of $1.5\text{--}1.7\ \text{kHz}$, and gas pressures of $\sim 100\ \text{mbar}$. A deviation from these parameters markedly reduces the laser power and efficiency. Optimal average and peak powers are observed for 2% of Xe in the laser gas mixture.

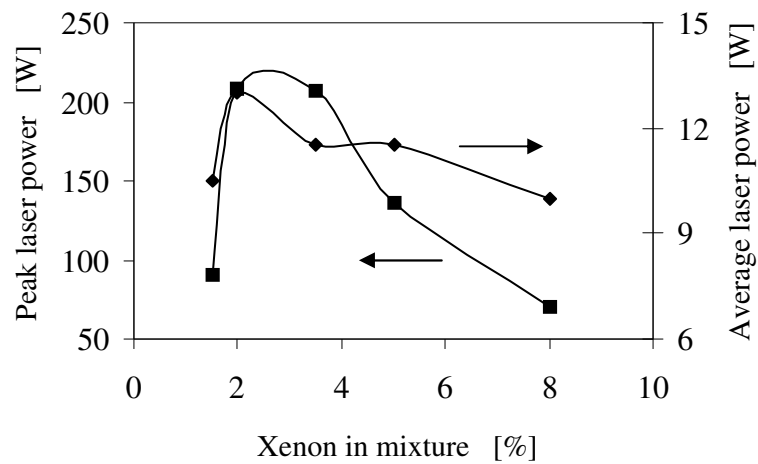


Fig. 4.44: The laser average and peak powers vs. the Xe percentage in the mixture.

When compared to the slow-flow laser schemes, the sealed-laser power is highly sensitive to the optical resonator alignment, the microwave matching, and the microwave-pulses parameters. Thus, further research is needed in order to optimize the presented sealed device, regarding a more accurate optical-resonator alignment, and a finer microwave tuning. Gas mixture optimization should be investigated in order to attain the optimal operation of this sealed device.

The sealed microwave-excited CO_2 slab-laser preliminary results prove the possibility of constructing a compact device with the feature of a high peak to average power ratio. The presented scheme is relatively simple and cost effective, compared to other schemes operating in the same parametric regime.

5. Analysis

This chapter summarizes and discusses the experimental results of the slab laser (scheme #2). The next chapter will provide a conclusive summary of the entire thesis, regarding the research questions and related future trends.

The microwave excitation of a CO₂ slab laser is investigated in this thesis. The main parameters influencing the extracted laser power in such a design can be divided into three main groups:

(a) The microwave feeding parameters

- 1) The input microwave power.
- 2) The temporal stability of the microwave-power pulse.
- 3) The magnetron operation regime.
- 4) The magnetron matching ability.
- 5) The microwave pulse width.
- 6) The microwave pulse repetition frequency.

(b) The discharge parameters

- 1) The gas cooling mechanism.
- 2) The discharge geometrical configuration.
- 3) The gas mixture type and optimization.
- 4) Gas pressure.
- 5) Gas flow rate.
- 6) Gas compartment cleanliness.
- 7) Inorganic material in the discharge zone (Torr-seal, plastic tubes).
- 8) Laser Pyrex-tube attachment to the metal walls.

(c) Optical setup parameters

- 1) Optical resonator type (single\multi mode operation).
- 2) Optical waveguide material (Quartz\Pyrex\Alumina\metal).
- 3) Optical waveguide dimension-tolerances.
- 4) Mirror mount configuration.

These parameters, in turn, control the following processes occurring in the slab laser experimental setup:

1. Magnetron average and peak-power extraction and matching.
2. Gas heating.
3. Evolution of discharge instabilities, thermal instabilities in particular.
4. Longitudinal homogeneity of the reduced field.
5. Gas dissociation.

These processes, in turn, determine the slab laser overall efficiency and output peak and average powers.

The next subsection discusses the microwave discharge development in the slab-laser plasma. An analytical model is used for the assessment of the longitudinal homogeneity of the microwave discharge, and the optimal microwave power coupling to the laser plasma. An accurate evaluation of laser longitudinal discharge field is accomplished by a 3D numerical microwave simulation program (ANSOFT HFSS).

5.1. Transient Temporal and Longitudinal Amplitude-Buildup

In order to describe a laser's microwave applicator, a microwave source feeding an arbitrary resonator through a known coupling agent is considered (Fig. 5.1). The resonator is characterized by its modal wave-number, characteristic impedance, and wall attenuation. While plasma is introduced in a part of the resonator's volume, the longitudinal wave-attenuation is modified accordingly. Two separate cases are studied, namely: (a) the matching of the source to an empty waveguide, and (b) matching to a plasma-loaded waveguide. The scattering matrix, $\underline{\underline{S}}$, describing the resonator coupling circuit [77] presented in Fig. 5.1 in the frequency domain is

$$\begin{bmatrix} V_1^- \\ V_2^- \end{bmatrix} = \underline{\underline{S}} V^+ = \begin{bmatrix} -\sqrt{1-K^2} & jK \\ jK & -\sqrt{1-K^2} \end{bmatrix} \begin{bmatrix} V_1^+ \\ V_2^+ \end{bmatrix}. \quad (53)$$

V^+ and V^- denote the wave amplitudes entering and exiting the two-port network, respectively. $|K| = \sqrt{1-|S_{11}|^2}$ is the coupling to the resonator, determined by the specific chosen method of coupling. Port 1 and 2 represent the coupling agent input and output ports. The input port (1) receives the source power, and the output port (2) couples the energy to the plasma loaded resonator.

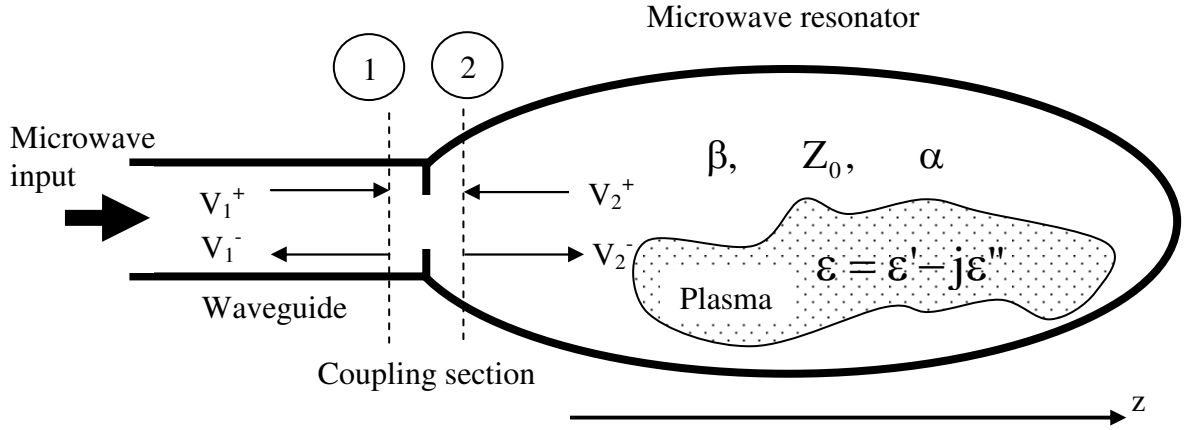


Fig. 5.1: The laser's microwave applicator represented by a source coupled to an arbitrary resonator, partially loaded by plasma.

A critical coupling of the microwave power to the resonator is defined as a coupling in which a minimum reflection exists at Port-1, and a maximal transmission exists at Port-2. By considering the resonator's electric length and internal attenuation, this coupling is found (Eq. (53)) as

$$K = \pm \sqrt{1 - e^{-2\alpha_T}} \quad (54a)$$

$$\alpha_T = 2\alpha z|_{z=L} \cdot \quad (54b)$$

α_T (Eq. 54b) is the round-trip total longitudinal-attenuation of the resonator, where α is the total resonator loss per meter, and L is the resonator axial length. Using a multiple reflection technique, where the resonator is simulated by a lossy transmission-line shortened at its end, the electric-field amplitude buildup at the two ports is found. When plasma is introduced in part of the resonator's volume, a longitudinal loss is added to the resonator wall-loss. This loss depends on the plasma conductivity (Eq. (33a)) which in turn depends on the electric field.

A transient temporal solution for two-port reflection coefficients is found by a series expansion of the forward and backward waves inside the resonator. The reflection coefficient at Port-1, defined as the relation between V_1^- and V_1^+ , is then evaluated for an amplitude buildup in the resonator as [77]

$$\Gamma_1(t) \equiv \frac{V_1^-(t)}{V_1^+(t)} = -\sqrt{1-K^2} + K^2 e^{-\alpha_T} \frac{1 - (\sqrt{1-K^2} e^{-\alpha_T})^{t/T}}{1 - \sqrt{1-K^2} e^{-\alpha_T}}, \quad (55)$$

where T is the round trip longitudinal transit-time of the wave defined by $T \equiv 2L/v_g$, L is the resonator's axial length and v_g is the group velocity of the wave. A similar expansion yields the reflection coefficient at Port-1 for a decaying field-amplitude in the resonator when the source is turned off, as

$$\Gamma_1(t) \equiv \frac{V_1^-(t)}{V_1^+(t)} = \frac{K^2 e^{-\alpha_T} (\sqrt{1-K^2} e^{-\alpha_T})^{t/T}}{1 - \sqrt{1-K^2} e^{-\alpha_T}}. \quad (56)$$

Using Eqs. (55), (56), the amplitude buildup and decay can be calculated for a pulsed operation under different coupling conditions, both temporally and longitudinally.

Next, we present a plasma-loaded microwave-setup together with its design considerations. Temporal results of the reflected and transmitted microwave power are presented, as well as results describing the longitudinal electric-field amplitude-buildup along the laser head. These results are compared to the experimental ones.

The presented mathematical model simulates the different longitudinal and temporal regimes for the suggested microwave coupling for the slab laser. A variable coupling-agent between the microwave source and the resonator, determines the coupling regime (e.g. under or over coupling, or critical). Two different critical-coupling values can be found, namely, for an empty waveguide (before the discharge initiation), and for the plasma loaded waveguide. The process of initiating a discharge will therefore be:

1. Setting a critical coupling for the empty waveguide.
2. Discharge initiation after a sufficient power-buildup in the resonator.
3. Setting a new critical coupling value for a maximal transmission of power to the plasma.

The resonator parameters are set for slightly-above cutoff operation. The length of the resonator is the same as in the experiment (Table 4.2), and the plasma characteristics (electron density, volume and channel length) fit the ones in the experiment as well. For this simulation we do not separate the laser head from the resonator. As a first approximation, we spread the plasma over the whole cross-

section of the microwave resonator, but only at a chosen part of its length. A complete and structurally exact numerical simulation of the device will be given as well.

Figs. 5.2a-c demonstrate the three different operation regimes. These figures show the relative amplitudes of the reflected wave at Port-1 (V_1^-), the transmitted wave at Port-2 (V_2^+), and the source's microwave-input envelope (V_{in}). The coupling in Fig. 5.2a is the critical for the empty waveguide, without the discharge plasma. Fig. 5.2b shows an initiation of a discharge under the same critical coupling (e.g. for an empty waveguide). The process observed occurs as follows: power builds up, until at a certain input-wave amplitude - the plasma is ignited (according to the specific geometry and gas pressure). At breakdown, plasma forms, and changes the critical coupling value. Thus, the input wave amplitude (V_2^+) drops, and the reflected-wave amplitude (V_1^-) rises. These fluctuations continue until a sufficient power is built up inside the resonator for a sustained discharge (steady state is reached).

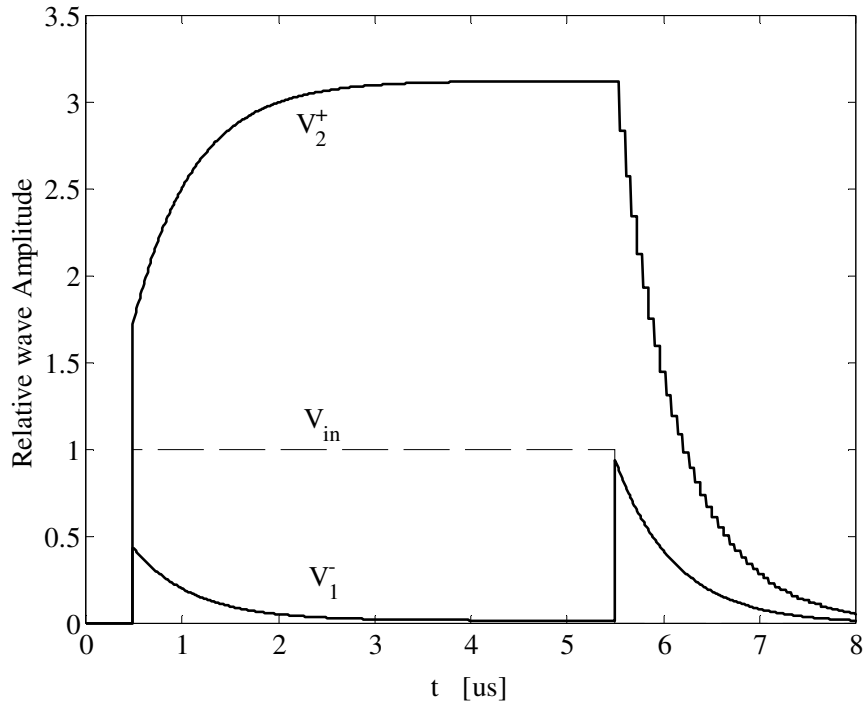


Fig. 5.2a: Critical coupling for an empty waveguide without plasma.

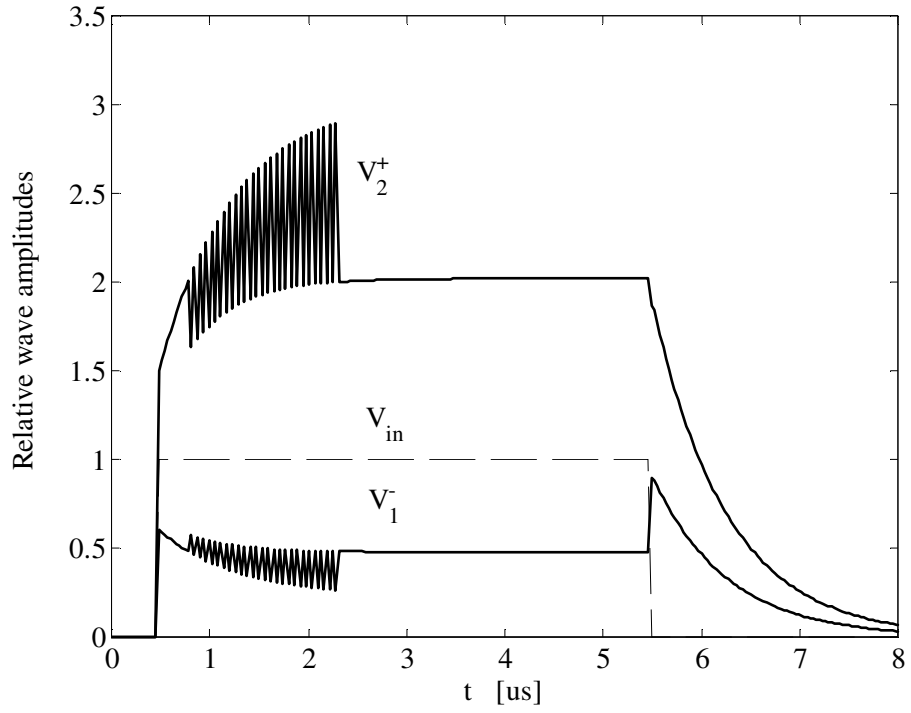


Fig. 5.2b: A discharge is initiated under empty waveguide critical-coupling.

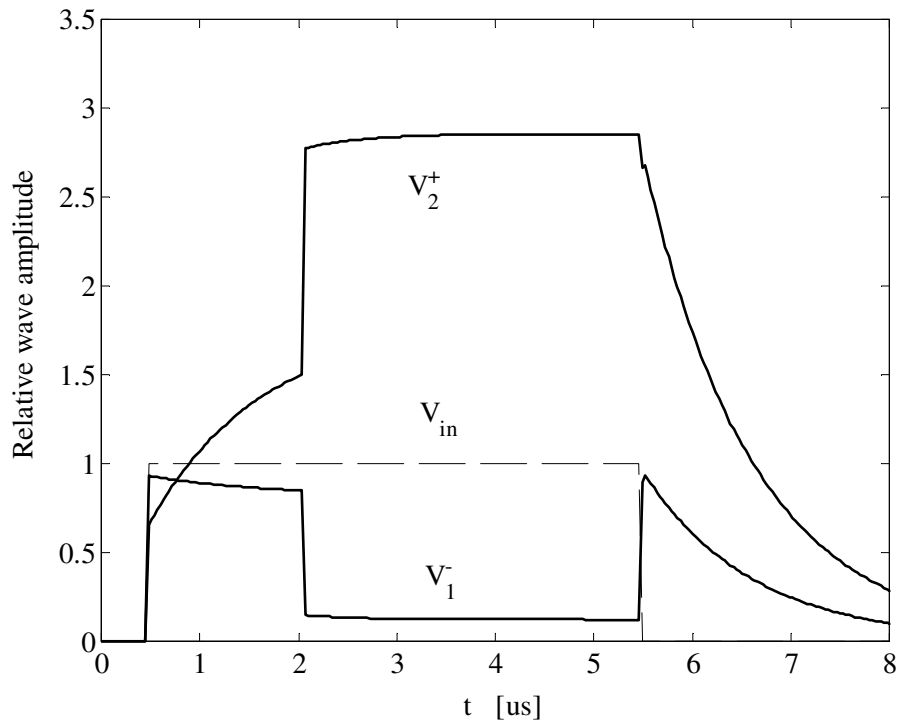


Fig. 5.2c: Critical coupling in the presence of plasma.

When the discharge is sustained, the values of the reflected and transmitted waves are not optimal since the coupling is still not optimized for a plasma-loaded resonator. Fig. 5.2c demonstrates a situation in which the coupling fits a plasma loading of the resonator. Before a discharge is initiated the reflection is relatively high. When the forward-wave amplitude in the resonator is sufficient for initiating the discharge, plasma is formed. The coupling now is critical (e.g. for the plasma loaded resonator) and the reflected-wave amplitude drops drastically. At the end of the microwave pulse, the discharge is not sustained, and the resonator's stored-energy decays.

The next figures present experimental results demonstrating the forward and reflected waves amplitudes, for a 10 μ s microwave pulse-width, detected by a directional coupler (Fig. 4.14). Fig. 5.3a presents the unstable changes in the reflected and transmitted wave amplitudes when the coupling is set for an empty waveguide (see Fig. 5.2b). Fig. 5.3b shows the discharge initiation for the same coupling, and Figs. 5.3c and 5.3d show the setting of the coupling to the critical one, in the presence of the discharge plasma (all measured amplitudes are negative).

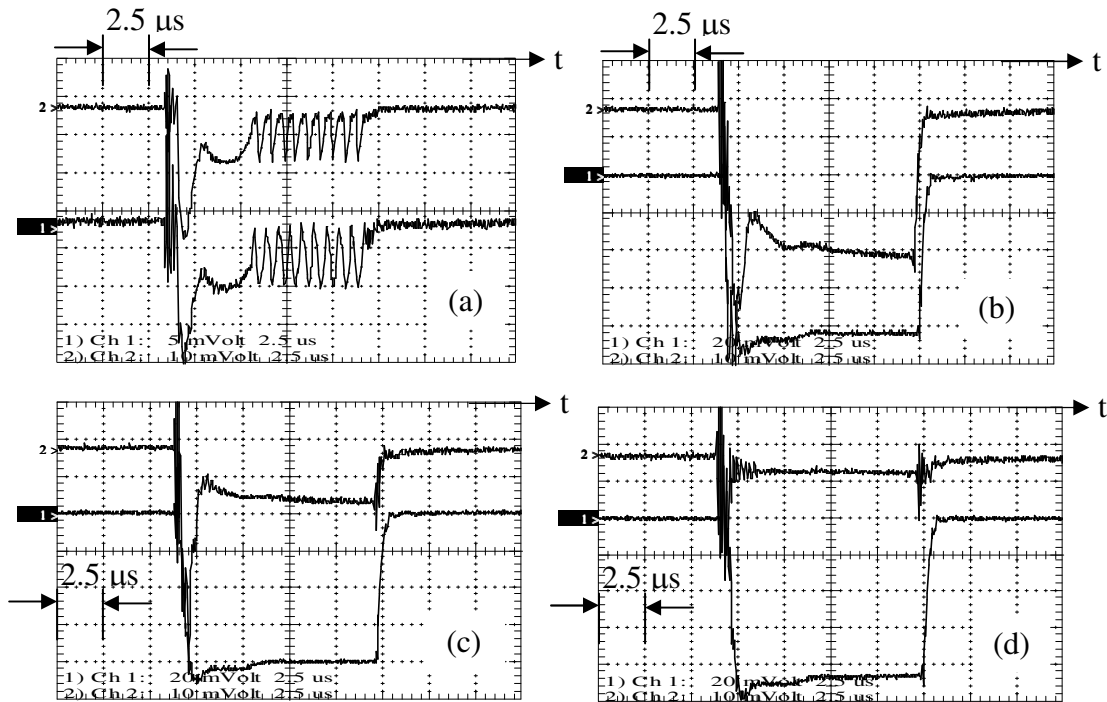


Fig. 5.3: Experimental measurements of the reflected (Channel 2) and transmitted (Channel 1) wave amplitudes for (a) empty waveguide critical coupling, (b) discharge initiation, (c,d) reaching critical coupling for the plasma loaded waveguide.

By adding the reflected and transmitted wave amplitudes inside the resonator along the microwave pulse, the resonator longitudinal-amplitude development is found. Figs. 5.4a-d show a calculation result, of the longitudinal development of the resonator's amplitude for the case of a critical matching in the presence of the plasma (Fig. 5.2c). A $5\text{ }\mu\text{s}$ microwave pulse width is considered. Fig. 5.4a demonstrates the sine form of the resonator-amplitude without a discharge, where the resonator operates slightly above cutoff conditions. Fig. 5.4b shows the amplitude longitudinal-change when the discharge is initiated. At this situation, power is longitudinally absorbed by the plasma. Therefore, the resonator amplitude decreases longitudinally. The maximal amplitude along the resonator is shown in Fig. 5.4c, and the amplitude temporal development is demonstrated in Fig. 5.4d. The dashed lines in Figs. 5.4b-d symbolize the plasma channel length inside the microwave resonator.

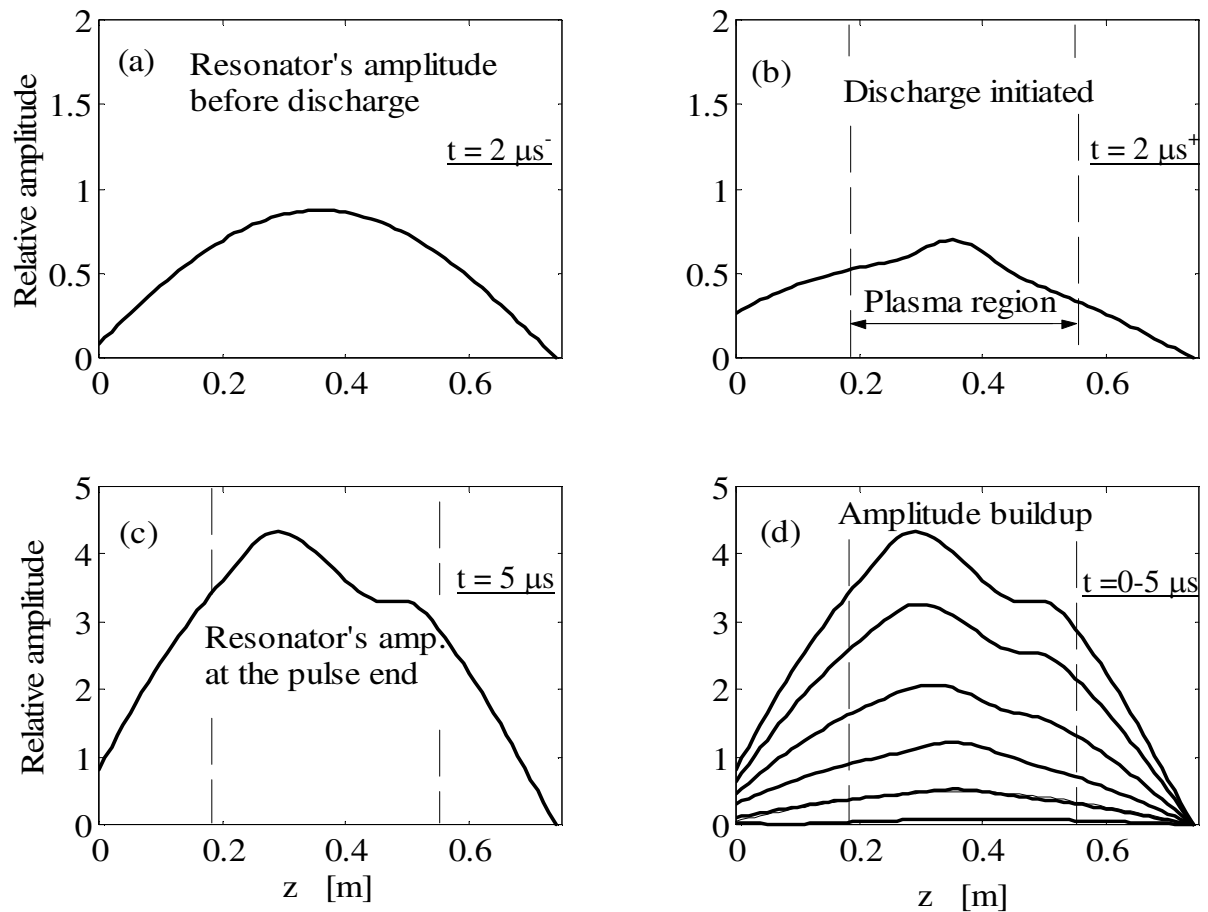


Fig. 5.4: The relative resonator's amplitude versus the z -axis calculated for a $5\text{ }\mu\text{s}$ microwave pulse (a) before the discharge, (b) when the discharge is initiated, (c) at the end of the microwave pulse, (d) amplitude buildup summary.

The transient temporal (Figs. 5.2a-c) and longitudinal (Figs. 5.4a-d) amplitude-buildup, includes only two means for enhancing the longitudinal uniformity of the amplitude, namely, (a) the formation of the resonator's fundamental longitudinal mode, and (b) setting a discharge channel shorter than the microwave resonator. A microwave simulation of the complete slab-laser structure is performed next.

The Ansoft HFSS 3D numerical microwave simulator is used to estimate the exact longitudinal homogeneity of the discharge electric field. Using a finite element method, this software allows the optimization of freedom-degrees of a setup. Since the setup contains ten interdependent degrees of freedom, the simulation time is relatively long, and proportional to the needed accuracy. Fig. 4.14 shows the laser head microwave setup in detail. Figs. 5.5a and 5.5b present the Ansoft HFSS simulation of laser's microwave-setup. Fig. 5.5a shows with real proportions the setup's components, namely, (a) the rectangular resonator, (b) the double ridge waveguide (laser head), (c) the rectangular Pyrex tube, (d) the source matching agent, and (e) the laser head coupling screws. The plasma was presented by its steady state conductivity. The source matching is achieved in the experiment by a triple stub, simulated by a one-stub matching element. Theory shows that the matching ability of both these matching networks is similar [72].

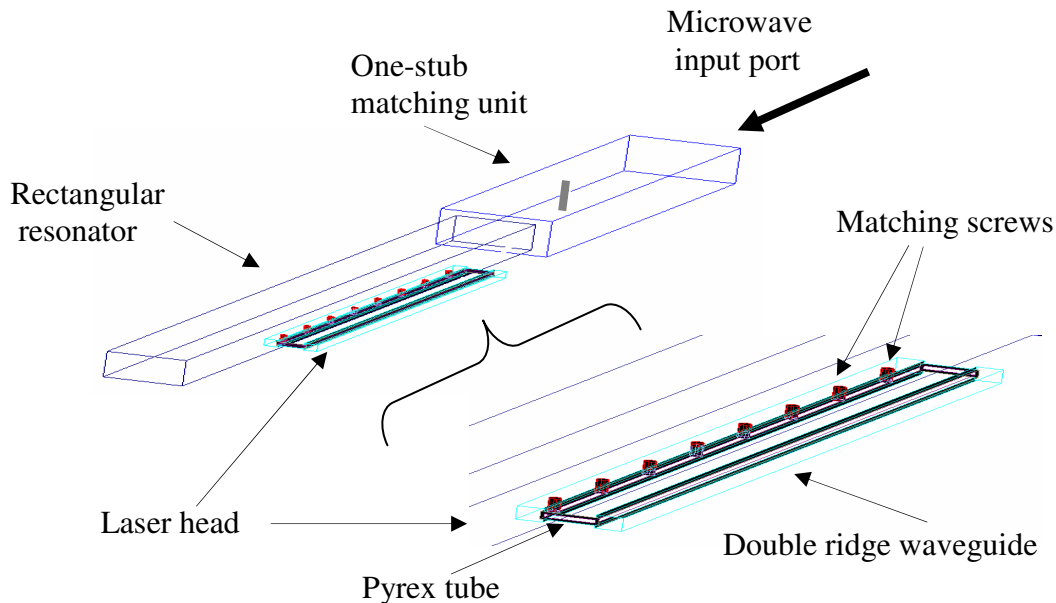


Fig. 5.5a: The ANSOFT HFSS microwave model (proportional scale).

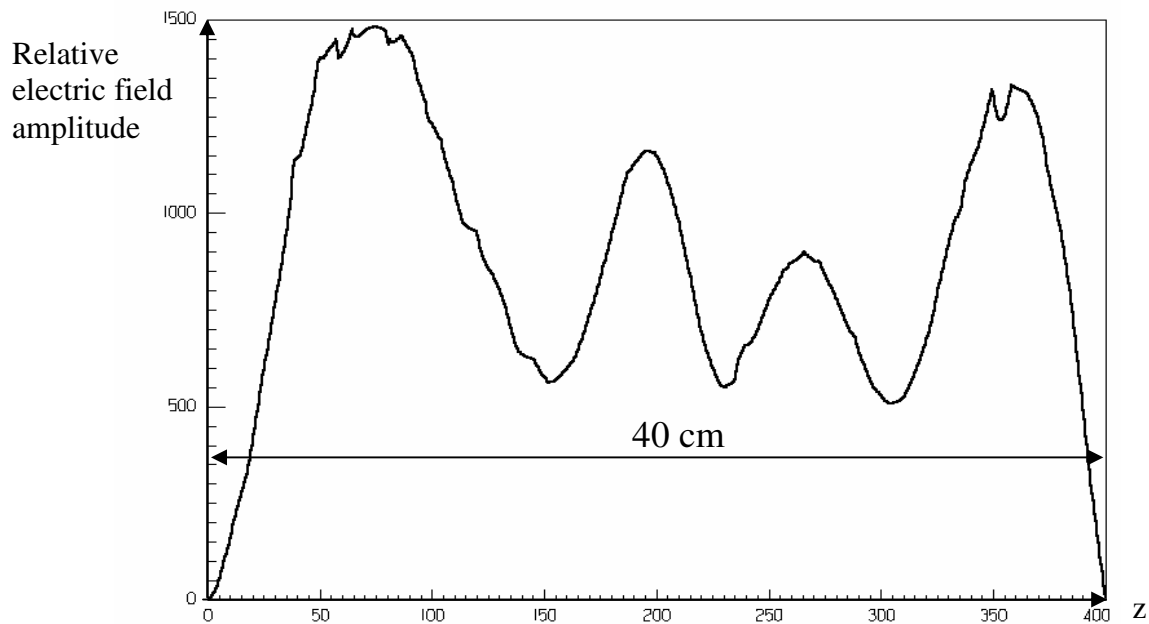


Fig. 5.5b: The discharge electric-field amplitude longitudinal-variation, calculated by the ANSOFT HFSS 3D numerical program.

As evident from Fig. 5.5b, no nulls appear across the full length of the laser head (40 cm). The measured discharge longitudinal microwave power distribution, and the discharge luminescence have shown better uniformity, compared to the simulation. This difference results from the inability of the simulation program to find the optimal solution in a limited time, optimizing all the microwave setup freedom degrees. Moreover, the experimental optimization is achieved in a few minutes, since one can observe simultaneously: the discharge luminescence, the microwave reflected-power, and the laser output power as well.

The present experimental microwave-setup design shows a simple method for a homogeneous longitudinal-discharge formation for slab laser-heads. The discharge field-formation and matching agents are divided into four sections:

1. Source matching section.
2. Rectangular resonator operating slightly above cutoff.
3. Double-ridge resonator laser-head with a constant cross-section.
4. Matching section between the two resonators.

The first stage consists of a triple stub, or one stub with full-scale matching of the magnetron to the rectangular waveguide. This section determines the critical coupling in the absence or presence of the discharge plasma. The rectangular waveguide, which

operates slightly above cutoff, allows the propagation of the fundamental longitudinal mode only, from which the homogeneous discharge-field is derived. A double-ridge resonator (which is axially shorter than the rectangular resonator) is designed to operate below cutoff (Eq. (46)). It is attached symmetrically to the rectangular resonator. The coupling agent between the two resonators is formed by an axial slit between the resonators, and eight screws placed along the coupling slit. Since the double-ridge resonator is operated below cut off, the field amplitude within it, is composed of a sum of odd decaying modes. The fields do not propagate axially in the ridged resonator, thus, no longitudinal standing wave pattern is observed (as shown in Fig. 4.18).

Measurement differences are observed when comparing the results for the two optional Pyrex-tube loading. The microwave matching was originally designed for a tube with a 2.0 mm discharge width. Therefore, the microwave-power uniformity, as measured by the network analyzer, is better comparing to the tube with 1.5 mm discharge width (Figs. 4.16a and 4.16b). Nevertheless, The reduced field deduced from the discharge luminescence is more homogeneous for the tube with a 1.5 mm discharge width (Figs. 4.17a and 4.17b). This can be attributed to the larger ratio of the ballast-strip thickness to the discharge width, for the 1.5 mm discharge width (Table 4.2). The large thickness of the Pyrex (3 mm total) for the 1.5 mm discharge width compensates for longitudinal variations in the reduced field (E/N). The resulting longitudinal discharge field is therefore more stable for this discharge width.

5.3. Slab Laser Thermal Investigation

The microwave-excited CO₂ slab-laser operation is inherently pulsed. This is due to the limited rate of heat-removal and the evolvment of thermal instabilities, as dictated by the presence of a dielectric slab. The thermal-instability considerations for these devices were discussed in detail in Chapter 3. The principle of a gas heat-conductance independent of pressure, allows raising the input power-densities and gas-pressure, while maintaining a constant effective reduced-field ($E/N \approx 2.5 \cdot 10^{-16} \text{ Vcm}^2$). Decreasing the discharge width increases the heat flow to the enclosing walls.

Fig. 5.6 shows schematically a steady-state solution for the temperature, and temperature gradient (arrows) in the slab configuration cross-section. This is a steady state solution of the heat equation by the MATLAB software PDE-toolbox.

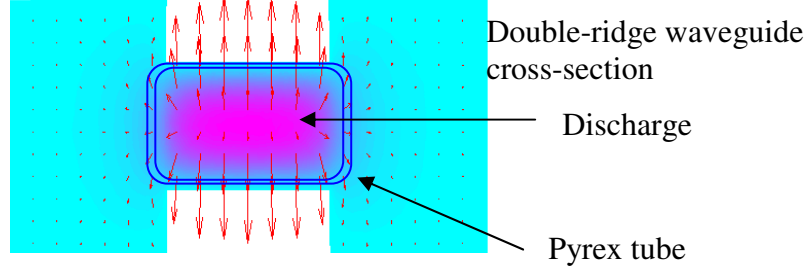


Fig. 5.6: A schematic presentation of the slab-configuration cross-section temperature and temperature gradient.

As discussed in Chapter 2, the maximal efficient operation-temperature of a CO₂-laser gas discharge is $\sim 500^\circ\text{K}$. Assuming an ignition temperature of $\sim 300^\circ\text{K}$ dictates a 200° temperature rise at the end of the discharge pulse. Thus, the microwave-excited CO₂ slab-laser mode of operation will be as follows: An intense excitation pulse elevates the gas temperature beyond the steady state temperature. Then, the temperature drops, and the initial temperature is reached at the time interval between the pulses. The pulsed mode of operation is depicted schematically in Fig. 5.7.

The gas steady-state temperature and the temperature-difference between the gas ignition and the pulse end, are mainly determined by the peak microwave power, and by the source duty-cycle. The gas heating, in turn, decreases the microwave to plasma power efficiency, decreases the laser gain, and widens the laser pulse.

Next, we try to map the maximal efficient temperature-difference as a function of the peak microwave-power, the pulse width, and the pulse repetition-frequency. The gas temperature-difference (ΔT) is determined by the heat-balance equation.

A linear approximation of the heat-balance equation for a slab laser configuration is

$$C_v \frac{d\Delta T}{dt} \cong \frac{P}{d} - \kappa \frac{4\Delta T}{d^2} \quad (57)$$

where C_v is the heat capacitance of the gas, P is the peak power-density per strip area, d is the discharge width, and $\kappa \left[\frac{W}{Kcm} \right]$ is the heat conductivity of the gas.

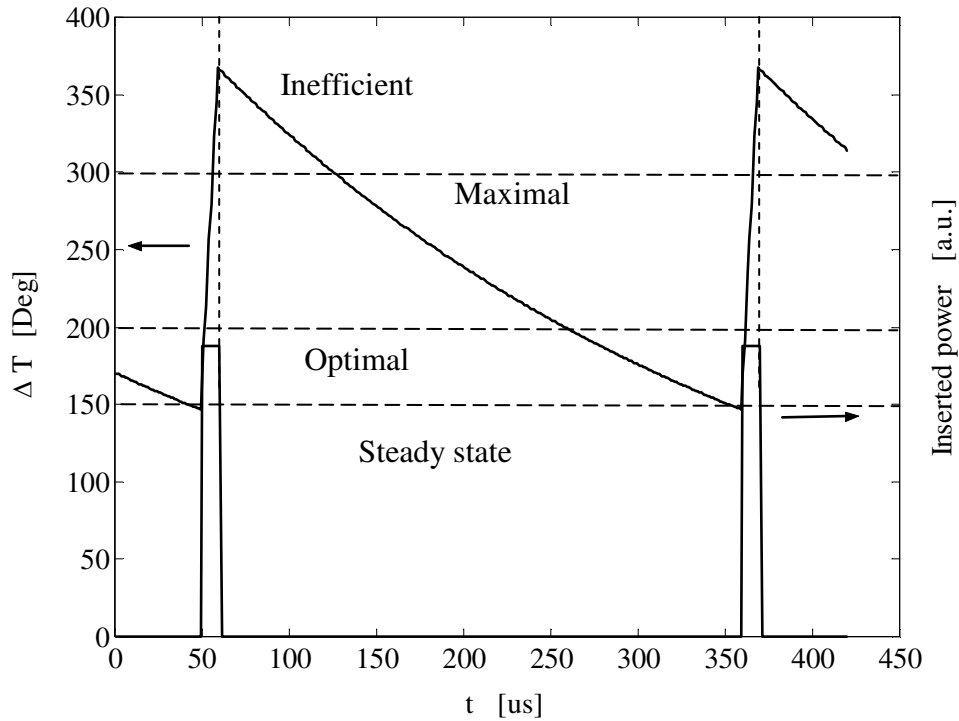


Fig. 5.7: The input power and the temperature difference between the center of the discharge and the enclosing walls, for the different regimes.

The temperature rise during the pulse is

$$\Delta T = \Delta T_0 + \frac{P}{C_v d} t, \quad (58)$$

where t is the time along the microwave pulse span (the rate of heat removal term is neglected during the microwave pulse), and ΔT_0 is the steady state temperature-increase at the beginning of a pulse. The decrease of the temperature during the time interval between the pulses is

$$\Delta T = \left(\Delta T_0 + \frac{P}{C_v d} t_p \right) \exp \left(-\frac{4\kappa t}{C_v d^2} \right) \quad (59)$$

where t_p is the pulse width. Assuming that for steady-state conditions the temperature difference decreases to ΔT_0 at the end of the time interval between the pulses, the temperatures at the pulse beginning and end are found as

$$\Delta T_0 = \frac{P}{C_v d} t_p \left[\exp\left(\frac{4\kappa t_c}{C_v d^2}\right) - 1 \right]^{-1} \quad (60a)$$

$$\Delta T(t_p) = \frac{P}{C_v d} t_p \left[1 - \exp\left(-\frac{4\kappa t_c}{C_v d^2}\right) \right]^{-1}. \quad (60b)$$

The modified discharge width d (with the dielectric strip excluded) is calculated using Equation (35c). It equals 2.07 mm and 1.56 mm for the 2.0 and 1.5 mm discharge widths, respectively (see Section 3.2.2.1).

The peak microwave power can be calculated from the data presented in the experimental-results section. Nevertheless, the resonator copper-losses should be considered for extracting the discharge peak microwave-power. The resonator wall-loss is found by [72]

$$\alpha = \frac{R_s}{b\eta\sqrt{1-(\lambda_0/2a)^2}} \left[1 + \frac{2b}{a} \left(\frac{\lambda_0}{2a} \right)^2 \right]. \quad (61)$$

$R_s = 2.61 \cdot 10^{-7} \sqrt{f}$ [Ω] for copper [72], $\eta = 377\Omega$ is the free space characteristic-impedance, a and b are the width and height of the rectangular resonator respectively (Table 4.2), f equals 2.45 GHz, and λ_0 is the corresponding wavelength. The power loss for the rectangular-waveguide's dimensions outlined in Table 4.2, is $\alpha = 0.038 [\text{m}^{-1}]$. Other loss factors are the microwave chain length, and the power that is reflected back to the source. The microwave chain length, from the power measurement point (i.e. the directional coupler) to the rectangular resonator, is ~ 0.7 m (see Fig. 4.14). Together with the reflected power, an additional maximal power loss of $\sim 10\%$ is considered. The plasma power loss is calculated by [47]

$$\mu_w[\text{m}^{-1}] = 0.106 \frac{n_e[\text{cm}^{-3}]}{v_m[\text{Hz}]}, \quad (62)$$

where n_e is the electron density, and v_m is the collision frequency. For typical experimental parameters of a 50 Torr pressure, the collision frequency is [83]

$$v_m = 1.75 \cdot 10^{12} \frac{50}{760} \cong 115 \quad [\text{GHz}].$$

The electron-density (for the optimal reduced field, at 50 Torr) is $n_e \cong 1.3 \cdot 10^{11} \quad [\text{cm}^{-3}]$ (see Chapter 3, Fig. 3.4a). Hence, the plasma power-loss (Eq. (62)) is $\mu_w \cong 0.12 \quad [\text{m}^{-1}]$. Therefore, under optimal coupling conditions, $\sim 35 \%$ of the microwave power is not transferred to the plasma. This power is dissipated in the microwave setup by heating the metal walls or reflecting back to the source.

Figures 5.8 and 5.9 present the temperature rise for the 2.0 and 1.5 mm discharge widths. Figures 5.8a-d, and 5.9a-d show the temperature differences for four pulse widths, namely, 6, 10, 20, and 30 μs . The investigation of the slab laser presented in this thesis is performed at these pulse widths. The results are derived for the gas pressures in which the optimal laser-results are measured for the two discharge widths. Each graph presents the temperature-rise traces for several peak input microwave-powers, as discussed above. The experimental optimal operation terms are indicated on each graph by a black dot. A dashed line shows the optimal and maximal temperature-differences of 200° and 300° .

The presented parametric thermal-investigation is an approximated one. Transient phenomena are not treated in a precise manner, and the purpose is to evaluate the steady state thermal-condition. The model is based upon a linear approximation of the heat equation. The only considered mechanism of gas cooling is the conductance cooling. Though negligible, other cooling mechanisms take place, such as the convection cooling. Therefore, the thermal survey of the laser head can be used as a means to compare the results of the two discharge- widths. It can be used as a first-order approximation for understanding the thermal behavior of the laser gas.

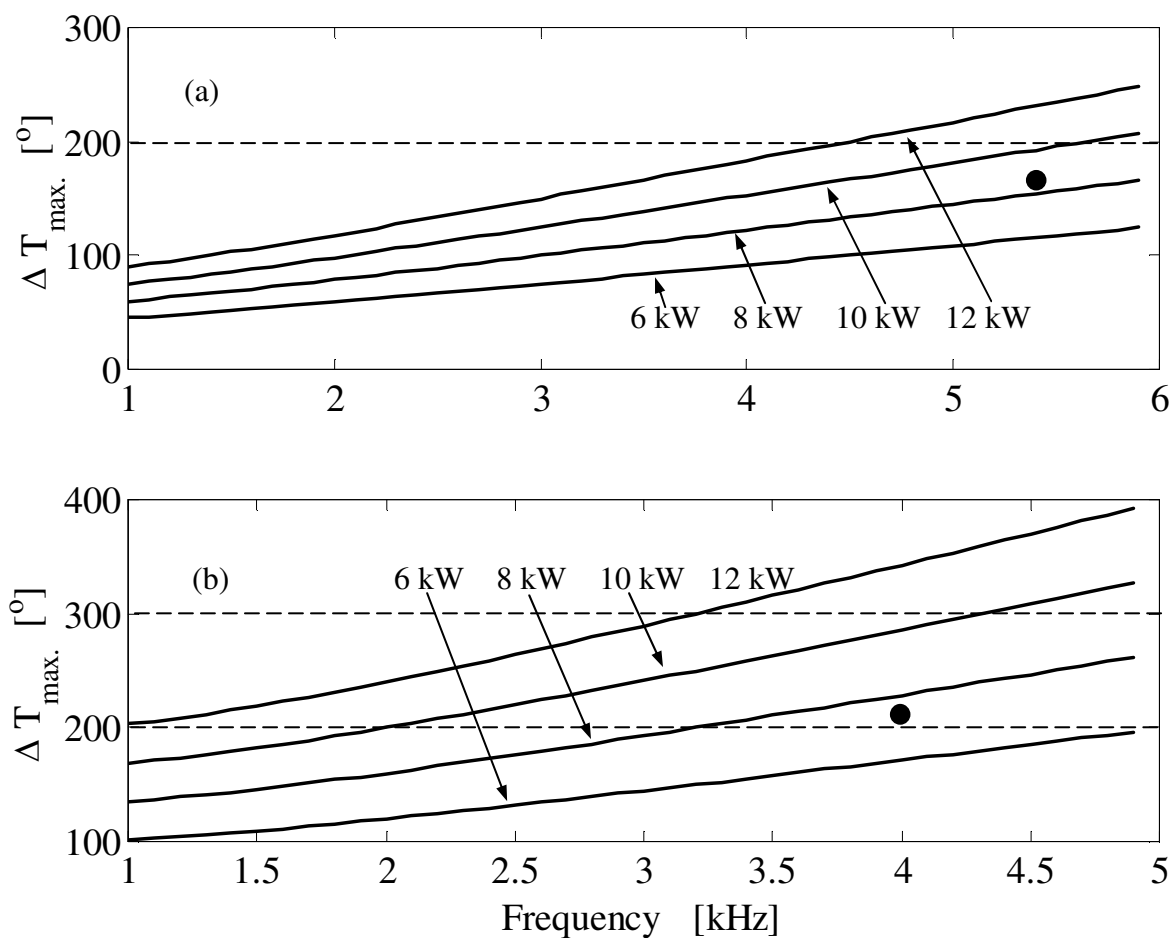


Fig. 5.8a,b: The gas temperature-rise for a 6 μs (a), and a 10 μs (b) pulse widths versus the pulse repetition frequency, for the 2.0 mm discharge width.

The peak microwave power is indicated for each trace.

The parameters for the optimal measurement points (indicated by a dot) for the 6 and 10 μs pulse widths are presented in Table 5.1 for the 2.0 mm discharge width.

Pulse width [μs]	Pulse frequency [kHz]	Gas pressure [Torr]	Peak μW power [kW]
6	5.4	65	8.65
10	4	45	7.5

Table 5.1: The measured parameters for the optimal measurement points for the 6 and 10 μs pulse widths, for the 2.0 mm discharge width.

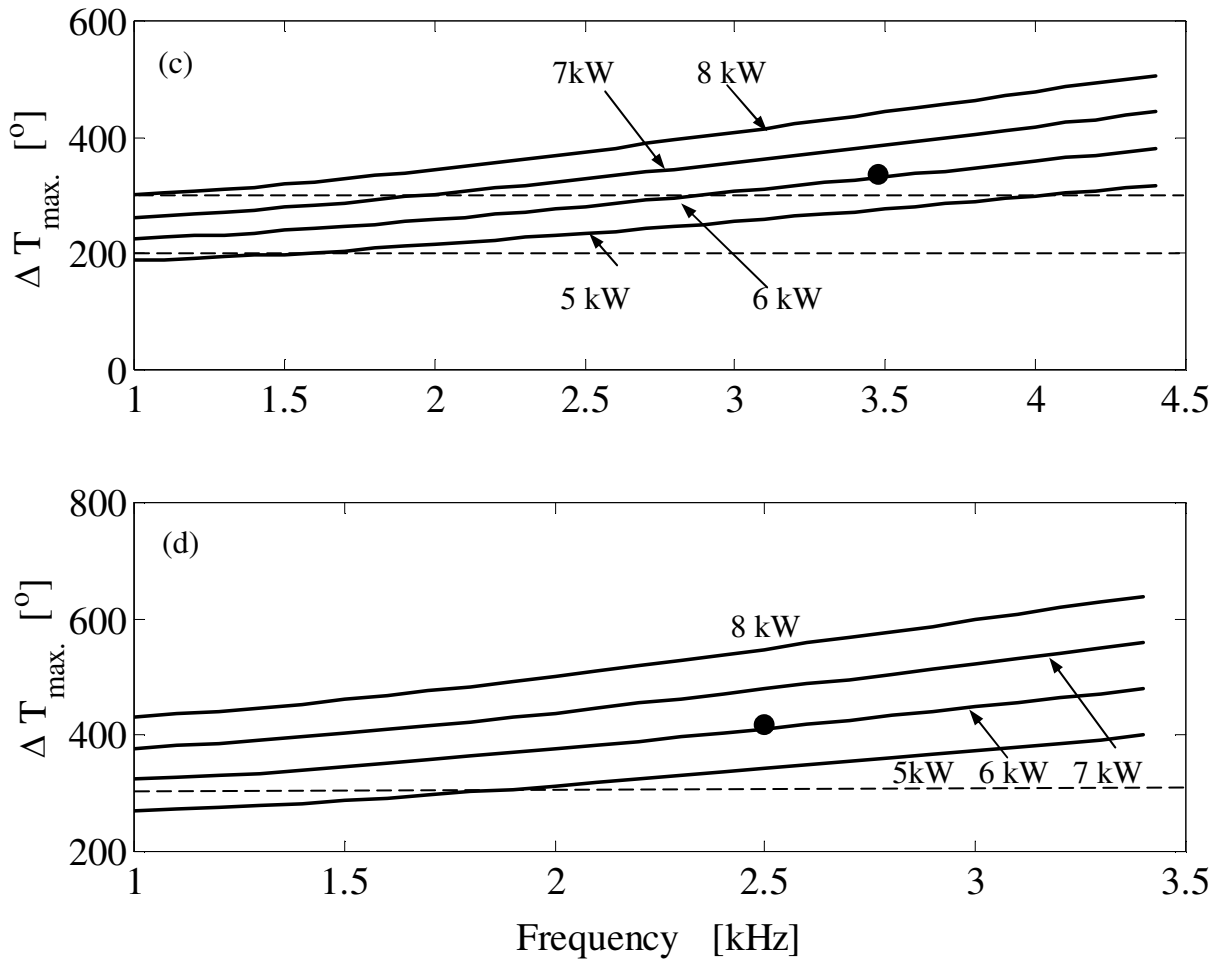


Fig. 5.8c,d: The gas temperature-rise for a 20 μs (c), and a 30 μs (d) pulse widths versus the pulse repetition frequency, for the 2.0 mm discharge width. The peak microwave power is indicated for each trace.

The parameters for the optimal measurement points at the 20 and 30 μs pulse widths are presented in Table 5.2 for the 2.0 mm discharge width.

Pulse width [μs]	Pulse frequency [kHz]	Gas pressure [Torr]	Peak μW power [kW]
20	3.5	40	6.1
30	2.5	42	9.2

Table 5.2: The measured parameters for the optimal measurement points for the 20 and 30 μs pulse widths, for the 2.0 mm discharge width.

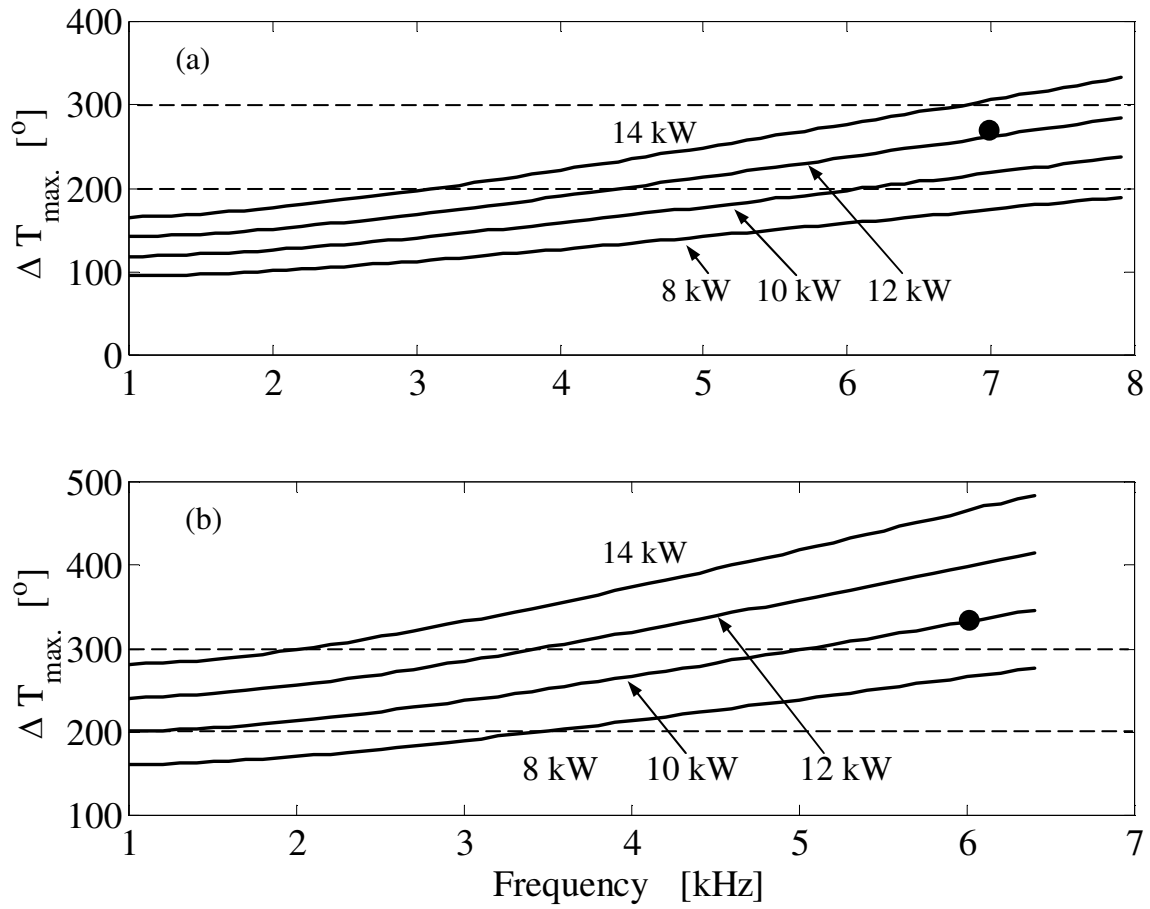


Fig. 5.9a,b: The gas temperature-rise for a 6 μs (a), and a 10 μs (b) pulse widths versus the pulse repetition frequency, for the 1.5 mm discharge width. The peak microwave power is indicated for each trace.

The parameters for the optimal measurement points at the 6 and 10 μs pulse widths are presented in Table 5.3 for the 1.5 mm discharge width.

Pulse width [μs]	Pulse frequency [kHz]	Gas pressure [Torr]	Peak μW power [kW]
6	7	50	12.35
10	6	49	10

Table 5.3: The measured parameters for the optimal measurement points for the 6 and 10 μs pulse widths, for the 1.5 mm discharge width.

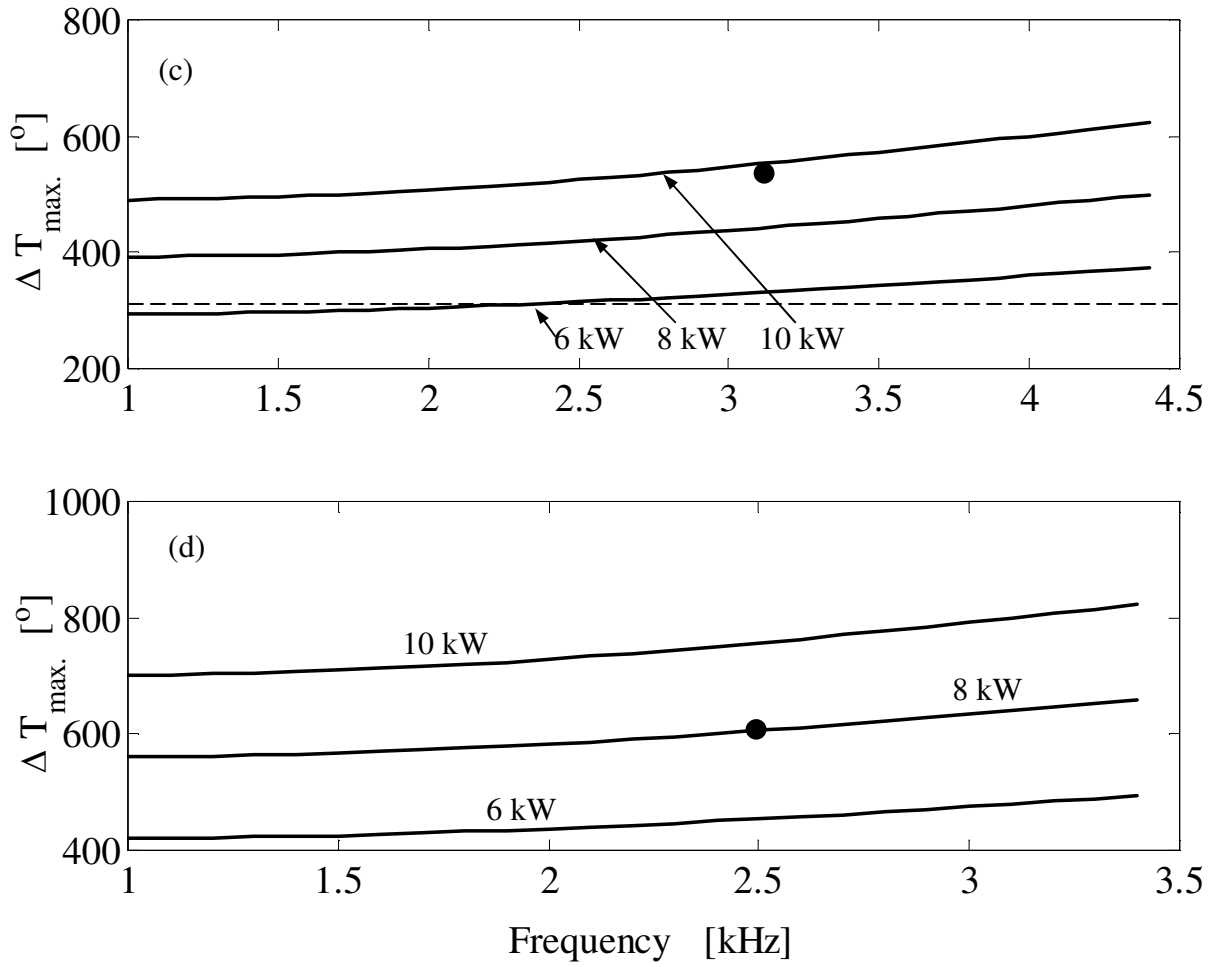


Fig. 5.9c,d: The gas temperature-rise for a 20 μs (c), and a 30 μs (d) pulse widths versus the pulse repetition frequency, for the 1.5 mm discharge width.

The peak microwave power is indicated for each trace.

The parameters for the optimal measurement points at the 20 and 30 μs pulse widths are presented in Table 5.4 for the 1.5 mm discharge width.

Pulse width [μs]	Pulse frequency [kHz]	Gas pressure [Torr]	Peak μW power [kW]
20	3.2	49	9.75
30	2.5	43	8

Table 5.4: The measured parameters for the optimal measurement points for the 20 and 30 μs pulse widths, for the 1.5 mm discharge width.

When considering the two sets of results, it is evident that the optimal temperature difference (along the microwave pulse) is larger than 200° . The thermal investigation shows that the optimal temperature difference (for the optimal laser power results) equals $\sim 320^{\circ}$. This can be attributed to additional cooling mechanisms that were not considered (convection). Moreover, it is evident that the temperature-rise during the microwave pulse, for all the measured pulse widths, is larger for the 1.5 mm discharge width, compared to the 2.0 mm discharge width. Hence, the additional cooling-mechanisms contribution increases with the discharge width.

Regarding the thermal behavior of the gas for the different pulse widths, the gas temperature-rise is lower than the optimal, for the $6\text{ }\mu\text{s}$ pulse width. On the contrary, it is much larger than the optimal, for the $30\text{ }\mu\text{s}$ pulse width, for both the discharge widths. This result is asserted by the fact that the optimal peak and average laser powers are not measured for these pulse widths (6 and $30\text{ }\mu\text{s}$). The efficiencies for the $30\text{ }\mu\text{s}$ pulse width for both the discharge widths are the lowest, as expected due to the gas overheating.

The optimal average powers for the 2.0 and 1.5 mm discharge widths are measured at 20 and $10\text{ }\mu\text{s}$ pulse widths. At these measurement points, peak microwave powers of 6.1 kW and 10 kW are measured, respectively. The optimal gas pressure for the 1.5 mm discharge width is 50 Torr, which is larger than the optimal pressure for the 2.0 mm discharge width (40 Torr). These experimental results corroborate the theoretical aspects of the rate of heat-removal considerations for the slab configuration, as presented in Chapter 1.

5.3. Slab-Laser Efficiency Assessment

In this research, an efficient design of a CO_2 -laser operating above 1 kHz pulse frequencies at tens of μs pulse widths was sought. Requirements such as tens of watts of average laser-power, and a large peak to average laser-power ratio, has led to the construction of a slab-laser excited by microwaves. The main considerations in constructing this device are

- 1) Excitation by an industrial 2.45 GHz, 2 kW magnetron.

- 2) Plain and compact configuration.
- 3) A homogeneous discharge field along the laser head.
- 4) Easy microwave impedance matching.
- 5) Large peak to average laser-power ratio at a slow gas-flow, or sealed operation.

The microwave design

The main feature of the present microwave design of the slab laser is its simplicity. By using a distributed coupling in which two microwave-resonators with unvarying cross-sections are attached, a longitudinally-uniform discharge at the laser head is attained. The constant cross-section of the microwave resonator including the laser head allows the use of a standard rectangular Pyrex-tube as the gas confinement chamber. Hence, the structure is simplified.

The discharge homogeneity

The discharge homogeneity is measured by two methods. Observing the microwave power distribution along the laser head, without the presence of the laser plasma, shows a power fluctuation of less than 0.5 dB and 3 dB for the 2.0 and 1.5 mm discharge widths, respectively. The axial deviation of the discharge reduced-field, calculated by measuring the longitudinal visible-luminescence power of the gas molecules electronic-states, yields 0.556×10^{16} , and 0.140×10^{16} for the 2.0 and 1.5 mm discharge widths. The laser head is designed for the 2.0 mm discharge width, hence, the microwave uniformity, for an empty resonator, is better for the 2.0 mm discharge width (Figs. 4.16a,b). Nevertheless, The reduced field is more homogeneous for the 1.5 mm discharge width, due to its large dielectric-loading thickness (3mm total), which compensates for changes in the discharge electric-field. This is one of the reasons for the attainment of the maximal average and peak powers in this discharge width (Figs. 4.37a,b). The enhanced homogeneity for the 1.5 mm discharge width results in a lower dissociation rate of the gas, which directly contributes to high laser powers.

The magnetron power and matching

The magnetron input power (Appendix A) determines its operation regime, which in turn influences its output impedance and its efficiency. According to the experimental

measurements, the magnetron efficiency ranges from 60-80 %, for a 1-8 kHz pulse repetition-frequency, and a 6-30 μ s pulse width. While an average power of up to 1 kW is extracted from the magnetron, the peak microwave-power ranges mostly from 10-15 kW. Raising the input power beyond a certain point causes phenomena such as longitudinal plasma-filaments in the laser head, or microwave breakdowns in the microwave resonator or the magnetron itself. The magnetron breakdowns can be partly avoided by increasing slightly the magnetron heating voltage. These phenomena decrease the laser power significantly, or cancel the microwave gas discharge.

Appendix A describes the magnetron used for the experimental device. It presents the considerations for peak and average power extraction from the magnetron. The average microwave-power delivered to the plasma, determines the maximal average laser-power. Raising the average microwave-power increases the average laser-power. Nevertheless, it increases the gas dissociation, the gas heating, and the probability of instabilities development. As summarized in Appendix A, the distributed microwave setup, which includes a few microwave power-matching elements, allows operating the magnetron in its optimal regime. This constraint, in the proposed microwave setup does not contradict the demand for a longitudinally homogeneous microwave-discharge.

The laser extracted power

At gas flow rates of several liters-per-second, the gas cooling by convection is negligible. The average power measurements for the 2.0 mm discharge width (Fig. 4.28a) show that raising the gas flow-rate up to 2 l/s, allows the attainment of an average power of 35 W. The increased gas flow-rate, partly compensates for the gas dissociation. The same trend is evident for the 1.5 mm discharge width. Raising the gas flow-rate allows to elevate the input average microwave-power, and consequently – the average laser-power. The maximal average laser-power for the 1.5 mm discharge width is \sim 40 W measured at a pressure of 50 Torr, a gas flow-rate of 1.1 l/s, and a \sim 0.9 kW of input microwave power. The microwave pulse width for this measurement is 10 μ s and the pulse repetition-frequency is 6 kHz.

The peak laser-power is mainly determined by the laser gain and by the magnetron peak microwave-power, which influences the laser gain as well. The laser

small signal gain (Figs. 4.41a,b) varies slightly versus the pulse repetition-frequency for the different pulse widths. The magnetron extracted peak-power varies, depending on the setup matching and plasma parameters, as explained in Appendix A. The magnetron peak-power does not vary significantly versus the pulse repetition-frequency, for a certain gas pressure, flow rate, and pulse width. However, it is evident for both the 2.0 and 1.5 mm discharge widths that the peak laser-power decreases with the rise of the pulse repetition frequency. Besides the gas over-heating, a probable mechanism responsible for this phenomenon is the CO₂ molecules dissociation to the CO molecule, and the O atom. It lowers significantly the average and peak laser-power. The gas dissociation and heating result in a lower microwave to plasma power conversion efficiency (Figs. 4.20b-4.27b and 4.29b-36b).

The microwave to laser efficiency

The microwave to plasma power conversion efficiency varies from 40-70 %. This can be explained by the fact that the laser head is designed for the 2.0 mm discharge width without the presence of the plasma (Fig. 4.16a). The microwave source matching changes by the presence of the laser plasma (Appendix A). The plasma characteristics set by the pulse width and frequency, and by the gas pressure and flow rate, change the microwave to plasma efficiency. A typical plasma to laser power conversion efficiency is ~ 10 %. It decreases versus the pulse frequency due to the gas heating (section 5.2.). The maximal plasma to laser power conversion efficiency is ~ 20 % measured for the 1.5 discharge width at a gas pressure and flow-rate of 50 Torr and 1.1 l/s, respectively. The microwave pulse width and repetition frequency for this measurement is 10 μ s and 2 kHz, respectively.

6. Conclusions

This thesis presents an investigation of microwave excited CO₂ lasers. It focuses on two of the main constraints of the microwave discharge and laser excitation, namely:

1. Thermal instabilities evolution.
2. Longitudinal homogeneity of microwave discharges.

The CO₂ slab laser excited by a magnetron is proposed as a favorable candidate for a sealed high-power device with a high peak to average power ratio.

CO₂ lasers with high average and peak powers, having the inherent feature of a high peak to average power-ratio, are not easily realized in the parametric regime of tens of microsecond pulse widths, and above 1 kHz pulse repetition frequencies.

In this thesis, the microwave excitation of CO₂ lasers was investigated in order to find suitable solutions for its drawbacks. The research results lead toward an extremely efficient, compact, sealed microwave-excited CO₂ slab laser. This laser operates in a pulsed regime of above 1 kHz pulse repetition frequency, with pulse widths of tens of microseconds. Thus, it fills the gap that exists in this parametric regime.

The difficulty of thermal-instabilities development in microwave discharges was addressed by using a simple discharge model for the optimization of the discharge, regarding its thermal-instabilities development. Although the unwanted γ to α discharge transitions are cancelled in a microwave discharge, it does not benefit the stabilizing effect of the ion depletion layers (as happens in RF discharges). Hence, a dielectric strip (Quartz, Alumina or Pyrex, for example) must be implemented in series to the discharge, as a ballast. This dielectric strip increased-thickness stabilizes the discharge, on one hand, but on the other – obstructs the heat flow to the enclosing metal walls. These two opposing demands, namely, a thick strip for the discharge stabilization, and a thin strip for improved heat flow were optimized in this thesis. A minimal ballast strip thickness was found for sustaining a thermally stable discharge. This ballast strip thickness was found to be independent of the gas mixture type (rich or poor helium mixture).

The slab laser configuration presented in this thesis is easily optimized regarding the rate of heat removal considerations. Throughout the experimental investigation, no

thermal instabilities were observed, as expected according to the thermal optimization carried out in this research.

The second difficulty addressed in this thesis was the formation of a longitudinally homogeneous microwave discharge. A preliminary device (scheme #1), in which this subject was studied in this thesis, was the cylindrical parallel-plate CO₂ laser. This device used a single parallel-plate resonator to which a magnetron antenna was coupled, and the laser discharge tube was inserted. A homogeneous discharge was observed in this device. Nevertheless, the lack of microwave-tuning degrees of freedom caused a poor matching of the magnetron power to the laser plasma. The basic mismatch between the magnetron and the laser head could not be overcome in this configuration. The resulting total efficiency of this device was ~1 % for an average laser-power of ~ 2 W, and a peak laser-power of 40 W.

Considering the microwave matching difficulties of the cylindrical parallel-plate configuration, a second higher-power device was designed and built (scheme #2). A distributed coupling of a magnetron source to a laser head, by means of two side-attached resonators was investigated. A rectangular waveguide operating slightly above a cutoff frequency of 2.45 GHz was attached in the H-plane to a double-ridged waveguide operated below cutoff. A longitudinal-slit coupled the two resonators. The constant cross-section, the double-ridged waveguide allowed the use of a standard rectangular Pyrex tube as the gas confinement chamber. This tube served as a dielectric load for the double-ridged waveguide. A graded coupling method allowed a proper matching of the magnetron to the rectangular resonator serving as an energy bank. It enabled the longitudinal tuning of a homogeneous discharge along the laser head as well.

A practical method is presented in this thesis for a longitudinal-discharge formation in slab laser heads with a longitudinally constant cross-section. This method is implemented in an experimental device, and reinforced by an analytical as well as a 3D numerical mathematical models. The results of both models coincide.

The slow gas-flow slab laser, was operated optimally at a pressure of ~ 50 Torr, and generated a maximal peak laser-power of ~ 575 W with an overall efficiency of 6 % in a duty cycle of 2 %. The maximal average-laser-power detected was ~ 40 W. An overall efficiency of 9 % in a duty cycle of 5 % was attained, corresponding to 22 % plasma-to-laser power efficiency.

A sealed laser structure based on the investigated CO₂ slab-laser design yields an average laser power of 13 W, which corresponds to a peak laser power of 210 W, with a microwave to laser-power efficiency of 4 %. A 5 % decrease in the peak laser power is observed after a two-hour operation.

The microwave-excited CO₂ slab-laser investigated in this thesis may prove to be a device overcoming the basic limitations of CO₂ lasers microwave-discharges. It proves the possibility of constructing a sealed, compact, high average and peak power CO₂ laser with the feature of a high peak to average laser-power ratio. The combination of an optimized rate of heat removal from the laser head, together with a longitudinally homogeneous discharge formation may result in a considerably high-efficiency device.

Appendices

Appendix A: The Magnetron to Laser Head Coupling

The microwave excitation-source chosen for the present CO₂ slab-laser is a Hitachi 2M130 magnetron. Fig. A1 shows the magnetron and specifies its external configuration.



Fig. A1: The Hitachi 2M130 magnetron.

The magnetron dipole antenna, coupling the energy from one of its resonators by a current loop, is inserted into a rectangular waveguide. The dipole antenna is coated with a ceramic cover serving as a vacuum seal, isolating material, and a mechanical support. The matching of the magnetron to the waveguide is achieved in the same manner as for a coax-to-waveguide coupler [72], considering the magnetron impedance.

A Rieke diagram specifies the magnetron operation regime. Fig. A2 presents a qualitative presentation of this diagram. A Rieke diagram uses a Smith chart to map the magnetron output-power changes due to variations in the output magnetron impedance and frequency. It specifies contours on which the output power does not change, as well as restricted operation and arcing regions. The center point of the

chart specifies the perfect matching of the magnetron, an operation point in which the maximal average power can be extracted from it.

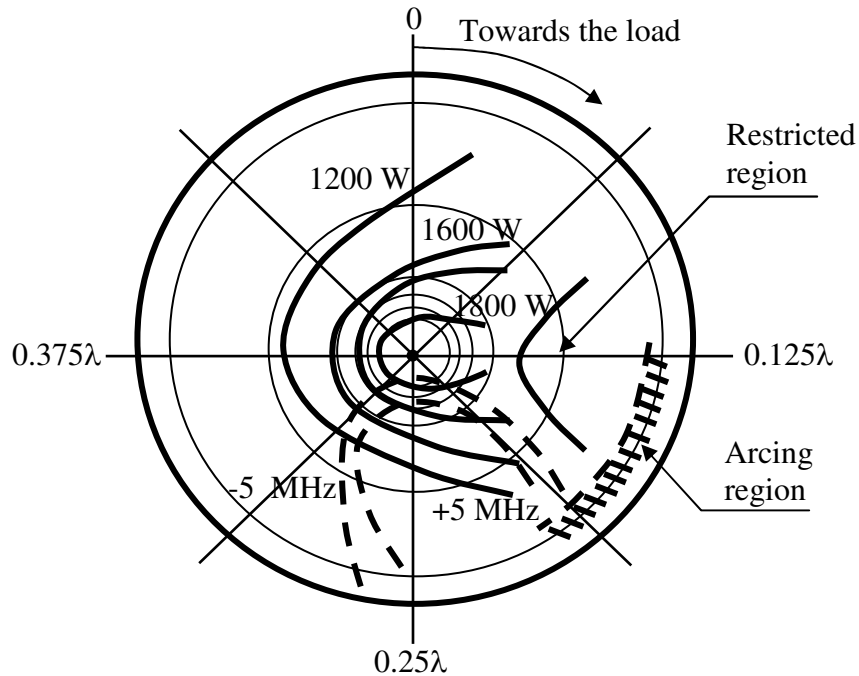


Fig. A2: A qualitative presentation of a Rieke diagram.

The maximal extracted average-power for the 2M130 magnetron, according to the manufacturer specifications, is ~ 1.8 kW. The maximal peak power indicated is ~ 9 kW (a peak to average power-ratio of 5). In our experiment (as demonstrated in other works [29]) a peak power of above 15 kW is measured for a peak to average power-ratios of ~ 20 . Raising the power delivered by the power supply changes slightly the magnetron high-voltage. It varies between 4-4.3 kV. The magnetron peak current reached is 6 A, exceeding the nominal current of 2.1 A indicated by the manufacturer. Other than this, we do not formulate any mechanism explaining the high peak to average microwave-power extraction.

Figure A3 describes a simplified transmission-line circuit demonstrating the coupling of a magnetron to a variable load through a coupling agent.

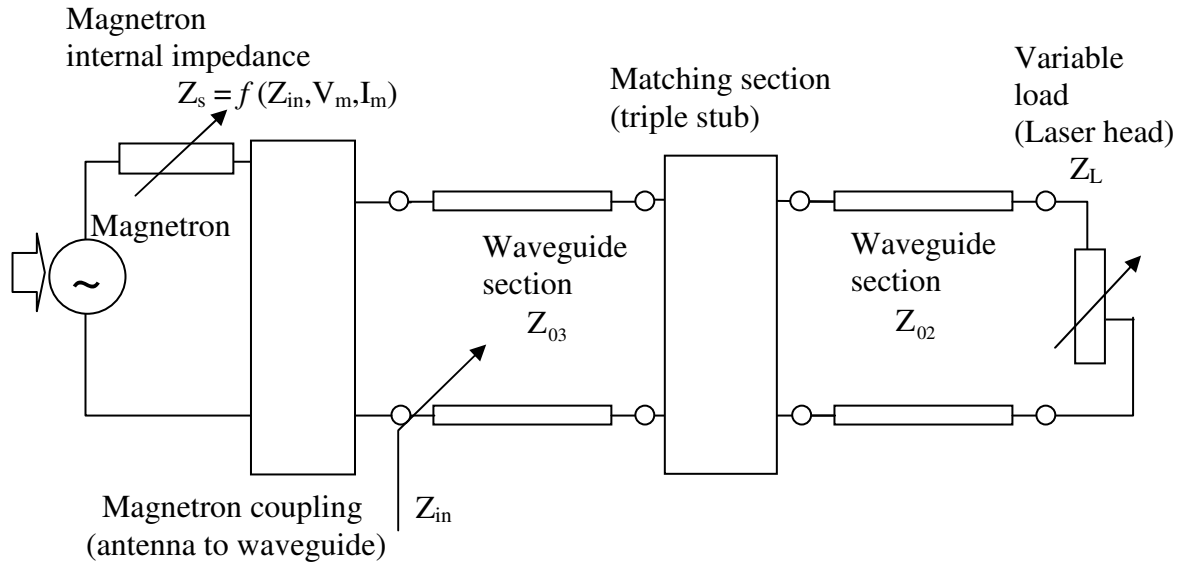


Fig. A3: The magnetron coupling to a variable load (laser head).

The magnetron impedance is variable, depending on its input high-voltage, heating voltage, and input impedance (Z_{in}) as well. The input impedance depends on the plasma characteristics, which in turn, are varied by the gas pressure and flow rate, and the pulse width and repetition frequency. Observing the reflected-wave amplitude and decreasing it by the use of a triple-stub section (see Chapter 4) performs the matching of the experimental setup. When the microwave channel is matched, the whole magnetron power reaches the laser head. Nevertheless, the input impedance seen by the magnetron might be different from its own impedance. This is why it is possible to increase the average microwave power by raising the pulse repetition-frequency. However, the maximal peak power is limited by the basic mismatch of the source and line impedance. This phenomenon is partly overcome by applying additional means for matching (i.e. screws along the laser head, or a variable stub at the rectangular-waveguide end).

Appendix B: High Voltage Switching

Two methods of switching were explored for the experimental setup, namely, electronic-tube switching, and solid state switching. The electronic tubes used for switching are:

1. Eimac 4PR60C.
2. Eimac 4CPL1000C.

Two tubes of the first kind, connected in parallel, allowed the switching of ~ 500 W of DC power (about 400 W of microwave power). This arrangement shown in Fig. B1 is reliable, and not sensitive to current sparks and voltage breakdowns. This switch demands considerable overhead in the form of several high-voltage power-supplies supplying the electronic tubes anode, grid, and heating voltages.

The second electronic tube, shown in Fig. B2, can switch up to 600 W when cooled by forced air or up to 1 kW when cooled by streaming oil. The supply voltages of this tube are lower than for the previous one, and more easily implemented. However, the tube cooling design is complicated.

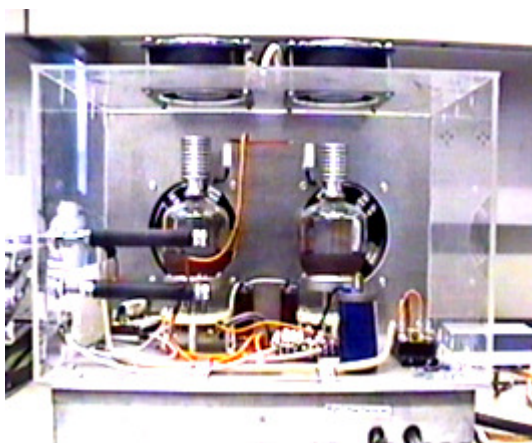


Fig. B1: The 4PR60C tube as a high voltage switch.

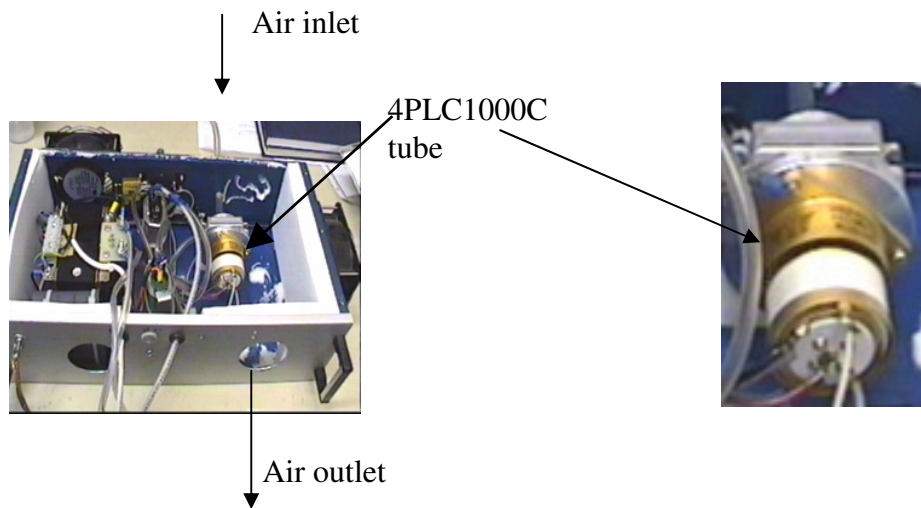


Fig. B2: The air-cooled 4CPL1000C tube as a high voltage switch.

A Behlke HTS81-03 solid-state switch was used for the high voltage switching. The main advantages of this switch is that it demands no overhead, besides an external TTL pulser, and it is extremely compact. This switch contains no means of protection against voltage or current spikes. Exceeding its power dissipation (15 W) instantly destroys it. Using this switch or one of its high power variations needs to be implemented by a breakdown protection and power dissipation monitoring.

A solution for the high-voltage switching for the lasers presented, was found in the form of a costume-built solid state switch made by Rotem Industries LTD (Fig. B3). This MOSFET switch is composed of a large number of low-voltage MOSFETs connected in series and parallel connections to increase its voltage and current capabilities. A Transorb protects every parallel MOSFET unit, and a Rogowski coil monitors the total switch-current. The unit is shut down in the case of a current spark. A thermocouple monitors the heating of the unit and shuts the unit down in the case of exceeding the maximal power dissipation. The unit, cooled by air convection, is able to switch an average DC power of 1.5 kW, at a maximal voltage and current of 10 kV and 100 A, respectively.

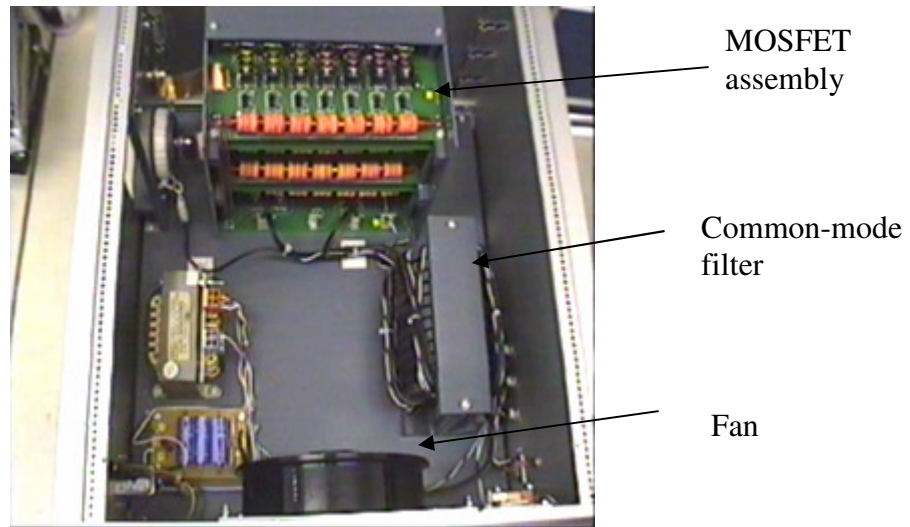


Fig. B3: The Rotem MOSFET switch.

A common-mode filter is used in this switch as in the laser experimental setup (Fig. 5.3) to cancel common mode noise. Common mode noise is formed by the high-voltage switching, and by an inductive nature of a load wiring to the switch (i.e. long wires). The common mode switch is composed of a ferrite cylinder or a few ferrite rings on which the entire signal wires (control, as well as high voltage) are wrapped around. When both wire conductors are wrapped upon the ferrite, a transformer is formed which cancels signals that are identical (regarding phase and amplitude) on both the conductors of the wire (i.e. noise).

Appendix C: Rectangular Pyrex Tubes for Gas-Confinement

A microwave-excited CO₂ laser uses a dielectric ballast-strip for stabilizing the microwave discharge. In the slab laser investigated in this thesis, a rectangular Pyrex-tube serves as the discharge ballast. It is fitted between the ridges of a double-ridge waveguide, and serves as the laser gas chamber as well. Using the tube as the gas chamber simplifies the vacuum considerations of the setup. The slab laser presented in this thesis demonstrates the characteristic of a uniform longitudinal microwave-discharge in a laser head with a longitudinally constant cross-section. This allows the use of a standard Pyrex tube instead of quartz or alumina strips. The rectangular Pyrex-tube is cheap (comparing to quartz or alumina), and widely available. Nevertheless, its heat conductivity is lower than the one for quartz and alumina. The lowered heat-conductivity limits the maximal laser pulse-width. However, due to discharge stability considerations, the microwave excited slab-laser operation is inherently pulsed, as discussed before.

Using a rectangular graphite-insert with accurate tolerances and pulling a melted standard cylindrical Pyrex-tube over it forms a rectangular Pyrex-tube. This method's limitations are: inaccurate tolerances, longitudinal grooves, and a limited aspect ratio of the tube cross-section. A tube processed by that method retains material strains as depicted in Fig. C1. These stresses can be alleviated by annealing (heating it to ~ 560 °C).

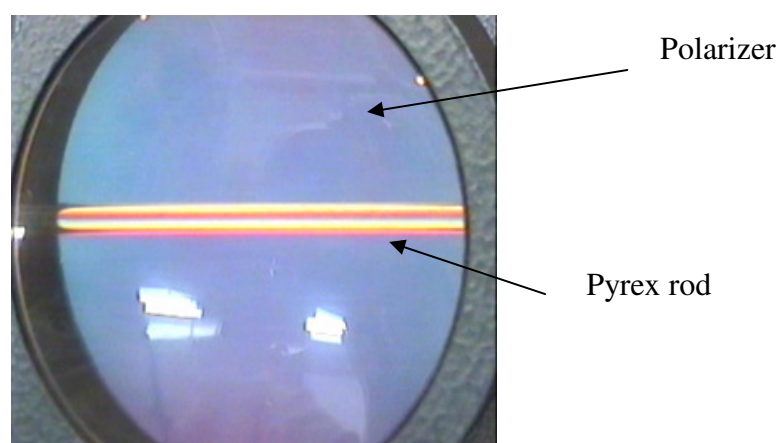


Fig. C1: A Pyrex rod which was not annealed.

Fig. C1 shows the light reflected from a Pyrex rod through a polarizer. The different colors indicate differences in the material stress in different regions of the Pyrex rod.

Figure C2 shows rectangular Pyrex-tube as received from the factory (without annealing) and an annealed tube.

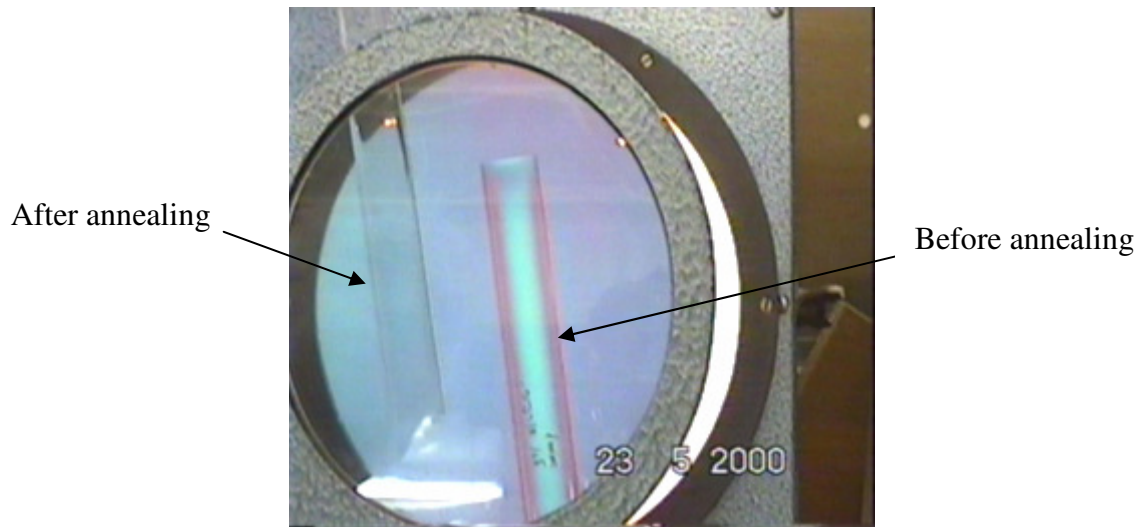


Fig. C2: A rectangular Pyrex tube before and after annealing.

Since the tube is heated in the laser head, and pressed by the ridges of the double-ridge waveguide, using it without annealing can cause the immediate cracking of the glass.

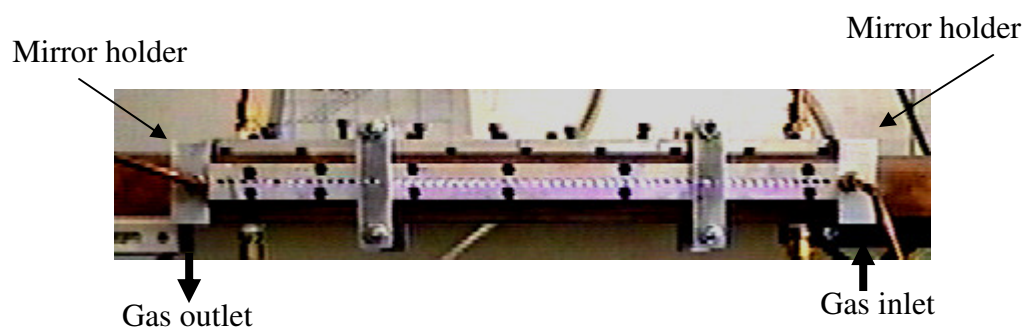


Fig. C3: The slab laser-head using mirror holders.

Two configurations were used to adjoin the rectangular Pyrex-tube to the optical resonator and laser gas-flow system. One configuration used mirror holders that were placed on the edges of the double ridge waveguide using O-rings (Fig. C3). In this configuration the mirrors were put on O-rings as well. Optical alignment was achieved in the following way: Screws were pressing a frame holding the mirror in the mirror holder, against the O-rings. The same method was implemented in the second version of the parallel-plate cylindrical laser (Fig. 5.2). The laser gas was circulated through holes in the mirror holders. Thus, no changes were made in the standard tubes. The main disadvantage of this method was the possibility of breaking the Pyrex tube when the mirror holders were attached to the laser head, due to the height tolerances of the tube. Another disadvantage of this design was the unstable alignment of the laser mirrors.

A different approach was to simplify the laser head and not use mirror holders at all. Since the laser is a waveguide laser, the mirrors were glued to the edge surfaces of the Pyrex tube, using Torr seal. This demanded that the tube edges were perfectly perpendicular to the tube axis. Operating the laser in this configuration proved successful regarding the alignment of the optical resonator. A more difficult consideration in this configuration was the inlet and outlet of the laser gas. Since the tube internal height was 2.0, or 1.5 mm, welding a side nipple could deform it.

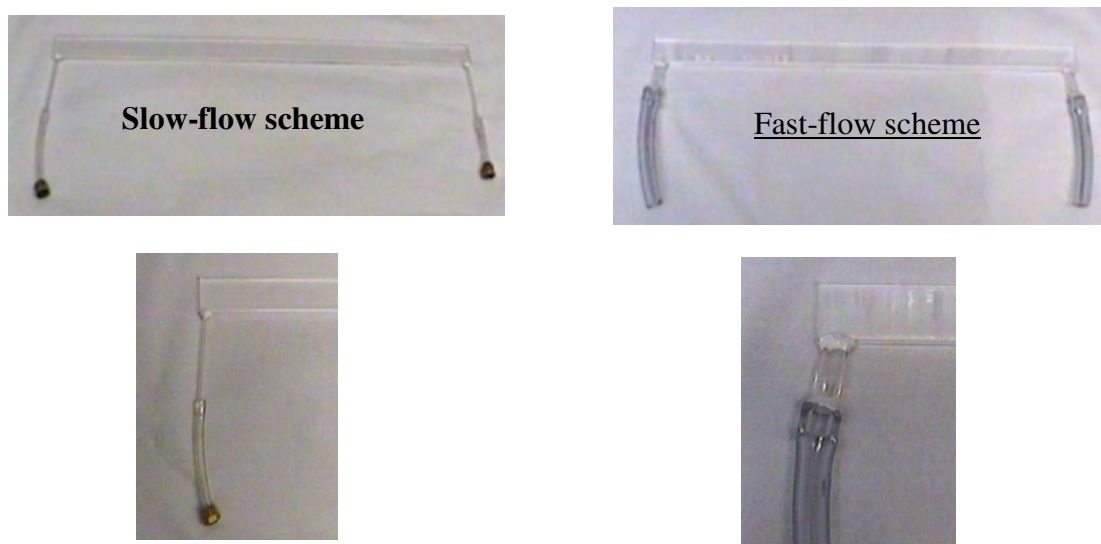


Fig. C4: Fast and slow gas flow-rate inlet and outlets for the rectangular Pyrex-tube.

A large outlet was even more difficult to form. The inlet and outlets were designed as follows: a miniature drilling machine (Dremel multipro) using diamond drills, drilled side holes in the tube. Side nipples were then glued to the holes by application of Torr seal. The nipples were attached to Tygon tubes to avoid stress (Fig. C4).

Two means were used to thermally attach the Pyrex tube to the ridges of the double-ridge waveguide. A standard silicon heat-conducting paste (i.e. Thermalcote, Thermalloy Inc.) was spread equally on the ridges and the tube itself. Since the tolerances of the tube height were up to 0.3 mm, the paste filled the gaps between the tube and the metallic ridges. Once a tube was attached to the metal by the silicon paste, it was impractical to remove it without breaking it. A solution to this difficulty was found in the form of using indium thin films (0.375 mm). The indium has a high heat-conductivity and it is extremely soft. The combination of indium strips and silicon paste allowed reopening the laser head several times without damaging the Pyrex tube.

Figure C5 shows the configuration of the tube used for the sealed CO₂ slab-laser.

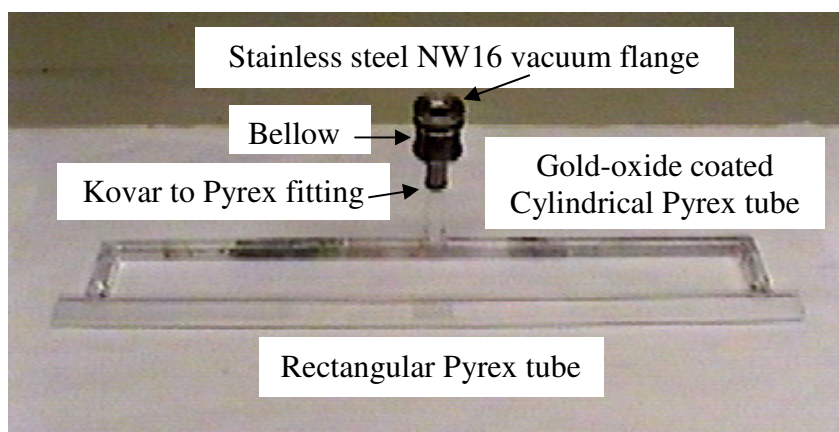


Fig. C5: The sealed CO₂ slab-laser Pyrex tube.

This tube includes the following components:

1. 485 mm long rectangular Pyrex-tube with inner dimensions of 2.0 mm x 20 mm and wall thickness of 1.3 mm.

2. 460 mm long, gold-oxide coated cylindrical tube, with 12 mm internal diameter, and wall thickness of 1 mm (The gold-oxide coating is used for enhanced recombination of the CO₂ dissociated molecules [81,82]).
3. 12 mm Kovar to Pyrex fitting.
4. 25 mm long stainless-steel bellow section, with external and internal diameters of 26 and 13 mm, respectively.
5. NW16 vacuum flange.

The crucial requirement in forming this tube is the welding of side nipples between the rectangular and cylindrical tubes. In order to achieve a welding which does not deform the rectangular Pyrex tube, serving as an optical waveguide, the following steps are taken:

1. The Pyrex tube is drilled by a diamond drill, in its narrow side (10 mm-wide opening). A wide path is needed for an increased diffusion between the two tubes in a sealed operation. Nevertheless, the wider the opening in the rectangular Pyrex-tube is, the harder it is to weld it to the side nipples without deforming it.
2. By the use of a rectangular graphite strip (1.2 mm x 20 mm cross-section) inserted into the rectangular Pyrex tube while welding, the Rectangular tube, serving as the optical waveguide, is not deformed. A delicate glass blowing work is needed in order to allow a minimal deformation of the rectangular Pyrex tube.

The use of Tygon tubes is avoided in this configuration because their out-gassing is detrimental for the laser sealed-operation. Minimal application of Torr seal is used for attaching widows to the tube edges. However, future setups can include appropriate mirror holders, which will annul the need of glue of any kind, for the preparation of the sealed tube.

References

1. C. H. Townes, "How the laser happened," *Oxford University Press*, New York, USA, 1999.
2. J. F. Ready, "Industrial applications of lasers," *Academic press*, New York, USA, 1997.
3. A. L. Schawlow and C. H. Townes, "Infrared and optical masers," *Physical Review*, Vol. 112, pp. 1940-1949, 1958.
4. R. V. Steele, "The laser market place 2000-part II: Diode lasers," *Laser focus world*, pp. 70-88, February 2000.
5. S. G. Anderson, "The laser market place 2000-part I: Non diode lasers," *Laser focus world*, pp. 92-112, January 2000.
6. C. K. N. Patel, "Interpretations of CO₂ optical maser experiments," *Physical Review Letters*, Vol. 12, pp. 588-590, 1964.
7. J. D. Evans and E. V. Locke (Eds.), "CO₂ lasers and their applications," *SPIE*, Vol. 1042, 1989, and articles therein.
8. C. K. N. Patel, "Carbon dioxide laser, a journey from milliwatts to megawatts," *SPIE, CO₂ lasers and their applications*, Vol. 1042, pp. 112-137, 1989.
9. P. B. Corcum, "Amplification of picosecond 10 μ m pulses in multiatmosphere CO₂ lasers," *IEEE Journal of Quantum Electronics*, Vol. QE-21, pp. 216-232, 1985.
10. G. B. Altshuler (Ed.), "Laser applications in medicine and dentistry," *SPIE*, Vol. 2922, 1996, and articles therein.
11. L. J. Miserendino, R. M. Pick, "Lasers in dentistry," *Quintessence Publishing Inc*, Chicago, USA, 1995.
12. W. J. Witteman, "The CO₂ laser," *Springer-Verlag*, Berlin, Germany, 1987.
13. E. V. Karulina and Y. A. Lebedev, "Relationship between the electron energy distributions in a microwave discharge and in a dc discharge in CO₂," *Soviet Journal of Plasma Physics*, Vol. 14, pp. 725-726, 1988.
14. V. A. Svich, V. M. Tkachenco, and A. N. Topkov, "Waveguide coaxial rf-excited CO₂ laser," *Soviet Journal of Quantum Electronics*, Vol. 20, pp. 612-614, 1990.

15. A. C. Eckbreth and J. W. Davis, "RF augmentation in CO₂ closed-cycle dc electric-discharge convection lasers," *Applied Physics Letters*, Vol. 21, pp. 25-27, 1972.
16. N. Ben Yosef, E. Bin Nun, F. Dotan-Deutsch, and S. Yatsiv, "Electrode configuration and power output for a transverse flow CO₂ laser," *Journal of Physics E*, Vol. 4, pp. 708-709, 1971.
17. W. B. Tiffany, R. Targ, and J. D. Foster, "Kilowatt CO₂ gas-transport laser," *Applied Physics Letters*, Vol. 15, pp. 91-93, 1969.
18. V. K. Kunyukhov, I. V. Matrosov, A. M. Prokhorov, D. T. Shalunov, and N. N. Shirokov, "Vibrational relaxation of CO₂ and N₂ molecules in an expanding supersonic gas jet," *JETP Letters*, Vol. 10, pp. 53-55, 1969.
19. O. S. Vasyutinskii, V. A. Kruzhalov, T. M. Perchanok, D. K. Terekhin, and S. A. Fridrikhov, "Pulsed microwave discharge as a pump for the CO₂ laser," *Soviet Physics, Technological Physics*, Vol. 23, pp. 189-194, 1978.
20. M. P. Vaisfeld and Y. E. Polskii, "Thermal regime in a coaxial low pressure CO₂ laser," *Soviet Journal of Quantum Electronics*, Vol. 11, pp. 1360-1362, 1981.
21. V. I. Mishenkov and N. A. Yatsenco, "Prospects for using high frequency capacitive discharges in lasers," *Soviet Journal of Quantum Electronics*, Vol. 11, pp. 1297-1301, 1981.
22. S. Yatsiv, "Conductively cooled capacitively coupled RF excited CO₂ lasers," *Gas Flow and Chemical Lasers, Proceeding of the 6th International Symposium*, pp. 252-257, 1986.
23. K. M. Abramski, A. D. Colley, H. J. Baker, and D. R. Hall, "Power scaling of large-area transverse radio frequency discharge CO₂ lasers," *Applied Physics Letters*, Vol. 54, pp. 1833-1835, 1989.
24. R. Nowak, H. Opower, K. Wessel, H. Krüger, W. Hass, and N. Wenzel, "Diffusions-gekulte CO₂-hochleistungslaser in kompaktbauweise," *Laser und Optoelectronik*, Vol. 23, pp. 68-81, 1991.
25. B. Freisinger, H. Frowein, M. Pauls, G. Pot, J. H. Schafer, J. Uhlenbush, "Excitation of a CO₂ laser by microwave discharges," *SPIE, CO₂ Lasers and Applications 2*, Vol. 1276, pp. 29-40, 1990.

26. R. Wester and S. Seiwert, "Investigation of microwave excited CO₂ discharge," *Journal of Physics D: Applied Physics*, Vol. 24, pp. 1102-1107, 1991.
27. T. Ikeda, M. Danno, H. Shimazutsu, T. Abe, and J. Tanaka, "TM₀₁₀-mode microwave excited high power CO₂ laser using a cylindrical resonant cavity," *IEEE Journal of Quantum Electronics*, Vol. 30, pp. 2657-2662, 1994.
28. T. Ikeda, M. Danno, T. Monaka, M. Noda, and J. Tanaka, "A new helical coupling microwave antenna excited high power CO₂ laser using a cylindrical resonant cavity," *IEEE Journal of Quantum Electronics*, Vol. 35, pp. 721-729, 1999.
29. J. Nishimae and K. Yoshizawa, "Development of CO₂ laser excited by 2.45 GHz microwave discharge," *SPIE, High Power Gas Lasers*, Vol. 1225, pp. 340-348, 1990.
30. M. März and W. Oestreicher, "Microwave excitation of a diffusion-cooled CO₂ laser," *Journal of Physics D: Applied Physics*, Vol. 27, pp. 470-474, 1994.
31. M. März and W. Oestreicher, "A versatile microwave plasma source and its application for a CO₂ laser," *Review of Scientific Instruments*, Vol. 65, pp. 2980-2983, 1994.
32. I. Dutov, I. Y. Evstratov, A. A. Kuleshov, S. A. Motovilov, N. A. Novoselov, V. E. Semenov, V. N. Sokolov, M. S. Yur'ev, "Experimental investigation and numerical simulation of a slab waveguide CO₂ laser with rf pumping," *Kvantovaya Elektronika*, Vol. 23, pp. 499-503, 1996.
33. Y. Sintov, A. Gabay, S. Yatsiv, "Self-activated, forced convective cooling in a pulse slab CO₂ laser," *Journal of physics D: Applied Physics*, Vol. 30, pp. 2530-2535, 1997.
34. G. Lan, D. Jiang, T. Hou, G. Zhao, X. Wang, and Q. Qu, "Experimental study of gain-guided waveguide-array (1 × 10) CO₂ laser," *IEEE Journal of Quantum Electronics*, Vol. 29, pp. 2722-2723, 1993.
35. A. Lapucci and G. Cangioli, "Triple slab radio-frequency discharged CO₂ laser," *Applied Physics Letters*, Vol. 62, pp. 7-9, 1993.

36. W. D. Bilida, H. J. J. Seguin, and C. E. Capjack, "Resonant cavity excitation system for radial array slab CO₂ lasers," *Journal of Applied Physics*, Vol. 78, pp. 4319-4322, 1995.
37. D. J. Hidson, V. Makios, R. W. Morrison, "Transverse CO₂ laser action at several atmospheres," *Physics Letters*, Vol. 40A, pp. 413-414, 1972.
38. G. J. Schulz, "Cross sections and electron affinity for O⁻ ions from O₂, CO, and CO₂ by electron impact," *Physical review*, Vol. 128, pp. 178-186, 1962.
39. M. J. W. Boness and G. J. Schulz, "Vibrational excitation of CO₂ by electron impact," *Physical Review Letters*, Vol. 21, pp. 1031-1034, 1968.
40. O. Judd, "Fundamental kinetic processes in the CO₂ laser," *Institute of Physics Conference, Ser. No. 29, High-power gas lasers*, E. R. Pike (Ed.), pp. 29-57, 1976.
41. T. Ledig and B. Schröder, "Electron energy distribution functions and power transfer data for radio-frequency discharges in CO₂ laser gas mixtures," *Journal of Physics D: Applied Physics*, Vol. 23, pp. 1624-1632, 1990.
42. D. He and D. R. Hall, "Influence of xenon on sealed-off operation of rf-excited CO₂ waveguide lasers," *Journal of Applied Physics*, Vol. 56, pp. 856-857, 1984.
43. S. Grudszus and M. März, "Influence of gas dissociation and xenon addition on steady-state microwave-excited CO₂ laser discharges," *Journal of Physics D: Applied Physics*, Vol. 26, pp. 1980-1986, 1993.
44. A. J. Landerman and S. R. Byron, "Temperature rise and radial profiles in CO₂ lasers," *Journal of Applied Physics*, Vol. 42, pp. 3138-3144, 1971.
45. R. A. Hass, "Plasma stability of electric discharges in molecular gasses," *Physical Review*, Vol. 8, pp. 1017-1043, 1973.
46. G. Ecker, W. Kroll, and O. Zoller, "Thermal instability of the plasma column," *Physics of Fluids*, Vol. 7, 2001-2006, 1964.
47. Y. P. Raizer, "Gas Discharge Physics," *Fizika gazovogo razryada*, Nauka, Moscow, 1987.
48. W. L. Nighan, "Electron energy distributions and collision rates in electrically excited N₂, CO, and CO₂," *Physical Review A*, Vol. 2, pp. 1989-2000, 1970.

49. J. J. Lowke, A. V. Phelps, B. W. Irwin, "Predicted electron transport coefficients and operating characteristics of CO₂:N₂:He laser mixtures," *Journal of Applied Physics*, Vol. 44, pp. 4664-4671, 1973.
50. A. L. S. Smith, "Gas laser discharges," *Physics Systems and Techniques (Proc. 23rd. Scottish Universities Summer School in Physics)* ed. W. J. Firth and R. G. Harrison (Edinburgh: SUSSP), pp. 235-69, 1983.
51. Y. P. Raizer, G. I. Shapiro, "Ionization-superheating instability of a glow discharge in time-varying fields and stabilizing effect of a train of high-voltage pulses," *Soviet Journal of Plasma Physics*, Vol. 4, pp. 477-481, 1978.
52. C. J. Buczek, R. J. Wayne, P. Chenausky, and R. J. Freiberg, "Magnetically stabilized cross-field CO₂ laser," *Applied physics letters*, Vol. 16, pp. 321-323, 1970.
53. V. I. Myshenkov, N. A. Yatsenko, "Stability of composite discharge sustained by static and rf electric fields. 1. Structure of a high-current rf capacitive discharge," *Soviet Journal Plasma Physics*, Vol. 8, pp. 306-309, 1982.
54. I. L. Koroleva, A. P. Napartovich, and A. N. Starostin, "Spatial and temporal evolution of thermal-ionizational instability," *Soviet Journal of Plasma Physics*, Vol. 8, pp. 317-319, 1982.
55. A. Lapucci, F. Rossetti, M. Ciofini, and G. Orlando, "On the longitudinal voltage distribution in radio-frequency-discharged CO₂ lasers with large-area electrodes," *IEEE Journal of Quantum Electronics*, Vol. 31, 1995, pp. 1537-1542, 1995.
56. Y. P. Raizer, M. N. Shneider, N. A. Yatsenko, "Radio-frequency capacitive discharges," *CRC Press Inc.* Florida, USA, 1995.
57. Y. P. Raizer and M. N. Shneider, "Longitudinal structure of capacitive radiofrequency γ discharge and its analogy with a direct current glow discharge," *Journal of Physics D: Applied Physics*, Vol. 27, pp. 1457-1464, 1994.
58. A. G. Akimov, A. V. Koba, N. I. Lipatov, A. P. Mineev, P. P. Pashinin, and A. M. Prokhorov, "Influence of the excitation field frequency on the operation of an rf-pumped waveguide CO₂ laser," *Soviet Journal of Quantum Electronics*, Vol. 19, pp. 610-613, 1989.

59. R. Wester, "Frequency dependence of thermal volume instabilities in high-frequency CO₂ laser discharge," *Journal of Applied Physics*, Vol. 70, pp. 3449-3454, 1991.
60. P. P. Vitruk, H. J. Baker, and D. R. Hall, "The characteristic and stability of high power transverse radio frequency discharge for waveguide CO₂ slab laser excitation," *Journal of Physics D: Applied Physics*, Vol. 25, pp. 1767-1776, 1992.
61. P. P. Vitruk, H. J. Baker, and D. R. Hall, "Similarity and scaling in diffusion-cooled rf-excited carbon dioxide lasers," *IEEE Journal of Quantum Electronics*, Vol. 30, pp. 1623-1634, 1994.
62. D. R. Hall and H. J. Baker, "RF excitation of diffusion cooled and fast axial flow lasers," *SPIE 7th Annual Symposium on Gas Flow and Chemical Lasers*, Austria, Vol. 1031, pp. 60-67, 1998.
63. R. O. Miles, "Propagation losses at 10.6 μm in hollow-core rectangular waveguide for distributed feedback applications," *IEEE Journal of Quantum electronics*, Vol. QE-15, pp. 1396-1401, 1979.
64. C. A. Hill and D. R. Hall, "Coupling loss theory of single-mode waveguide resonators," *Applied Optics*, Vol. 24, pp. 1283-1290, 1985.
65. C. J. Shackelton, K. M. Abramski, H. J. Baker and D. R. Hall, "Lateral and transverse mode properties of CO₂ slab waveguide lasers," *Optics Communications*, Vol. 89, pp. 423-428, 1992.
66. B. V. Kuteev, A. S. Smirnov, "Stabilization of the superheat-ionization instability by an rf electric field," *Soviet Technical Physics Letters*, Vol. 4, pp. 46-47, 1978.
67. Y. F. Kolesnyshenko, V. D. Matyukhin, V. F. Murav'ev, and S. I. Smaznov, *Dokl. Akad. Nauk. SSSR*, Vol. 246, p. 1091, 1979.
68. R. Wester, S. Seiwert, and R. Wagner, "Theoretical and experimental investigations of the filamentations of high-frequency excited CO₂ laser discharges," *Journal of Physics D: Applied Physics*, Vol. 24, pp. 1796-1802, 1991.
69. Y. Sintov and A. Shahadi, "Thermal-instability considerations for pulsed microwave-excited CO₂ slab-lasers," *Journal of Physics D: Applied Physics*, Vol. 33, pp. 2125-2132, 2000.

70. J. J. Degnan, "The waveguide laser: a review," *Applied Physics*, Vol. 11, pp. 1-33, 1976.
71. L. J. Denes and J. J. Lowke, "V-I characteristics of pulsed CO₂ laser discharges," *Applied Physics Letters*, Vol. 23, pp. 130-132, 1973.
72. R. E. Collin, "Foundations for microwave engineering," *McGraw-Hill, Inc.*, New York, USA, 1992.
73. S. Hopfer, "The design of ridged waveguides," *IRE Transactions - Microwave Theory and Techniques*, Vol. MTT-3, pp. 20-29, 1955.
74. J. R. Pyle, "The cutoff wavelength of the TE₁₀ modern ridged rectangular waveguide of any aspect ratio," *IEEE Transactions on Microwave Theory and Techniques*, Vol. MTT-14, pp. 175-183, 1966.
75. G. Magerl, "Ridged waveguides with inhomogeneous dielectric-slab loading," *IEEE Transactions on Microwave Theory and Techniques*, Vol. MTT-26, pp. 413-416, 1978.
76. W. J. R. Hoefer, "Closed-form expressions of the parameters of finned and ridged waveguides," *IEEE Transactions on Microwave Theory and Techniques*, Vol. MTT-30, pp. 2190-2194, 1982.
77. J. L. Altman, "Microwave circuits," *D. Van Nostrand Company*, New York, USA, 1964.
78. J. T. Verdeyen, "Laser electronics," *Prentice Hall, Inc.*, New Jersey, USA, 1995.
79. A. L. S. Smith and P. G. Browne, "Catalysis in CO₂ lasers," *Journal of Physics D: Applied Physics*, Vol. 7, pp. 1652-1659, 1974.
80. G. C. R. Williams and A. L. S. Smith, "Plasma chemistry of RF discharges in CO₂ laser gas mixtures," *Journal of Physics D: Applied Physics*, Vol. 18, pp. 335-346, 1985.
81. J. A. Macken, S. K. Yagnik, and M. A. Samis, "CO₂ laser performance with distributed gold catalyst," *IEEE Journal of Quantum Electronics*, Vol. 25, pp. 1695-1703, 1989.
82. E. Tsuchida and H. Sato, "Recovery of transient gain in an open-cycle FAF CO₂ laser amplifier using gold catalyst," *Japanese Journal of Applied Physics*, Vol. 29, pp. 964-966, 1990.
83. B. E. Cherrington, "Gaseous electronics and gas lasers," *Holt Rinehart and Winston*, New York, USA, 1976.

אוניברסיטת תל - אביב
הפקולטה להנדסה ע"ש איבי ואלדר פליישמן
המחלקה לאלקטרוניקה פיסיקלית

מעוררי מיקרוגלים CO₂ לייזרי

חיבור לשם קבלת התואר "דוקטור לפילוסופיה"

מוגש על-ידי
אבי שהדי

אדר תשס"א

אוניברסיטת תל - אביב
הפקולטה להנדסה ע"ש איבי ואלדר פליישמן
המחלקה לאלקטרוניקה פיסיקלית

מעוררי מיקרוגלים CO₂ לייזרי

חיבור לשם קבלת התואר "דוקטור לפילוסופיה"

מוגש על-ידי
אבי שהדי

בהנחיית
פרופ' אליהו ג'רבי

יועץ: ד"ר יואב סינטוב

הוגש לסנאט של אוניברסיטת תל-אביב
אדר תשס"א

תקציר

בעבודה זאת נחקר עירור מיקרוגל של לייזרי CO_2 בקונפיגורציה חדשה של לייזר פס-סרט. ראש לייזר מסוג פס-סרט הוכח כמתאים ביותר לעירור בתדר רדיו או בתדרי מיקרוגל של לייזרי CO_2 חתומים, או בזרימה איטית, כפי שפורסם על ידי Yatsiv ואחרים. לייזרים אלו מאופיינים על ידי הספקים ממוצעים ושיאיים גבוהים. בשילוב עם עירור מיקרוגל, הם היעילים ביותר מבחינת היחס הגבוה של הספק הלייזר השיאי למוצע, בפעולה בפולסים, בתחום של רוחבי פולס של עשרות מיקרו-שניה ותדר פולסים של מעל קילו-הרץ אחד. באופן פעולה זה, לייזרי פס-סרט המעוררים על ידי מיקרוגל הוכחו כעדיפים על אלו המעוררים על ידי תדר רדיו או על לייזרים המיישמים עירור משולב של תדר רדיו ומתח ישר.

שני מנגנונים המשבשים את פעולתם של לייזרי CO_2 מסוג פס-סרט נחקרים בעבודה זאת:

- אי יציבויות טרמיות המתפתחות כתוצאה מתדר העירור הגבוה.
- שדה התפרקות שאינו אחיד אורכית, בגלל אורך הגל הקצר יחסית של מקור המיקרוגל המשמש לעירור.

במחקר זה נמצאו פתרונות מספקים לשיפור הפעולה של לייזרי CO_2 מסוג פס-סרט באשר לאי היציבויות הטרמיות וכן לעירור המיקרוגל האחיד. פתרונות אלו נתמכים על ידי תיאוריה ותוצאות ניסיוניות. כמו כן, מוצגות תוצאות ראשוניות של לייזר CO_2 חתום, המבוסס על תכנוני הלייזרים שנחקרו בעבודה זאת, ומשמר את תכונותיהם המועילות.

בעבודה זאת אנו חוקרים את עירור המיקרוגל של לייזרי CO_2 בשני התקנים שתוכנו ונבנו לפי הדרישות של (א) מגנטרון כמקור אנרגיה, (ב) התפרקות מיקרוגל אחידה אורכית, ו- (ג) התקן פשוט וקומפקטי.

הלייזר הראשון שנבנה במחקר זה הוא לייזר גלילי המעורר על ידי מהוד לוחות-מקבילים. התקן זה סיפק 2 W של הספק לייזר ממוצע, ו- 40 W של הספק שיאי. התפרקות מיקרוגל אחידה-אורכית נצפתה בלייזר זה, כפי שתואר על ידי מודל מתמטי. נצילותו של התקן זה לא עלתה על 1% בגלל אי תיאום בעכבות של המגנטרון ומהוד הלוחות המקבילים. למרות זאת, התקן זה הוא קומפקטי ופשוט ביותר לבניה, ועשוי לשמש למחקר של תיאום מקור המיקרוגל לראש הלייזר, וכן לבחינתן של אי יציבויות של התפרקות המיקרוגל בלייזרי CO_2 . הוא מאפשר את בדיקת השפעתם של פרמטרים שונים כגון סוג תערובת הגז, לחץ הגז וספיקתו, ונתוני מקור המיקרוגל על פעולת הלייזר.

בהתקן ניסיוני מתקדם יותר, יישמנו את המסקנות בנושא תיאום ההספק שהתקבלו בהתקן הראשון, וכן השתמשנו במודלים מתמטיים לפעולתו של לייזר CO_2 מסוג פס-סרט המעורר על ידי

אנרגיית מיקרוגל. שתיים ממגרעות התפרקות המיקרוגל בלייזר זה – אי היציבות הטרימית, וכן האחידות האורכית של ההתפרקות – נחקרו בעזרת מודלים מתמטיים. מודל להתפתחות אי יציבויות טרמיות בעירור מיקרוגל פולסי ללייזרי פס-סרט פותח במחקר זה. במודל מבוצעת אופטימיזציה לעובי הפיסה הדיאלקטרית המוכנסת לאזור התפרקות המיקרוגל למניעת אי יציבויות טרמיות. על ידי אופטימיזציה זאת, ניתן לשפר את פינוי החום מאזור ההתפרקות בנקודת עבודה נתונה, ובכך לשפר את נצילות ההתקן.

מודל מתמטי נוסף פותח כדי להדגים התפרקות מיקרוגל אחידה בעירור מיקרוגל ללייזר CO_2 מסוג פס סרט. מודל זה מתחשב בהעמסת מהוד המיקרוגל על ידי פלסמה, ומדגים מיקרים של צימוד אופטימלי, תת צימוד וצימוד יתר בנוכחות הפלסמה ובלעדיה. מודל נומרי (Ansoft HFSS) משמש לסימולציה נומרית מדויקת של לייזר פס הסרט, ומתחשב בעשר דרגות חופש של תיאום מיקרוגל הקיימות בו. תוצאות מודל זה דומות לתוצאות הניתוח האנליטי. התוצאות המתמטיות מאומתות על ידי תוצאות ניסיוניות של (א) התפלגות הספק המיקרוגל לאורך ראש הלייזר, (ב) התפלגות עצמת ההארה לאורך ראש הלייזר.

תכנון לייזר זה מיועד להשיג (א) תחום פעולה מיטבי של המגנטרון (המאפשר את נצילותו הגבוהה), (ב) יצירת שדה התפרקות אחיד אורכית. שני מהודי מיקרוגל מצומדים ב-H-plane, כאשר אחד המהודים קצר מהשני. אחד המהודים משמש לאגירת אנרגיה והשני משמש כראש הלייזר. על ידי כך, מתקבלת התפרקות מיקרוגל אחידה אורכית. תכנון ראש הלייזר כמבנה אחיד רוחבית מאפשר הרכבה פשוטה. הספקי הלייזר הממוצעים והשיאיים נבדקו בעובי התפרקות של 2.0 ו-1.5 מ"מ. השפעת גורמים כגון הספק המיקרוגל ולחץ הגז וספיקתו נחקרו. הנצילות של הדרגות השונות בהתקן – הספק הרשת להספק המיקרוגל, הספק המיקרוגל להספק הפלסמה, והספק הפלסמה להספק הלייזר נבדקה. נבדק הגבר האות הקטן של הלייזר וכן הוערכה איכות הקרן לשני גובהי ההתפרקות.

ראש הלייזר מסוג פס-הסרט צומד למגנטרון בעל הספק ממוצע של 2 kW ותדר של 2.45 GHz על ידי מהוד מלבני. לייזר זה הפועל בזרימת גז איטית הופעל בצורה מיטבית בלחץ גז של 50 Torr, וסיפק 575 W של הספק שיאי בנצילות של 6 % ו-duty cycle של 2 %. הספק ממוצע מקסימלי של 40 W נמדד בהתקן זה, בנצילות המרת-הספק פלסמה ללייזר של 11 % ו-duty cycle של 6 %. הנצילות הכוללת המרבית שנמדדה היא 9 % ב-duty cycle של 5 %, המתאימה לנצילות מיקרוגל-לייזר של 22 %.

לייזר חתום במבנה המתבסס על לייזר פס הסרט שנחקר בעבודה זאת מפיק הספק ממוצע של 13 W, המתאים להספק שיאי של 210 W, בנצילות הספק מיקרוגל ללייזר של 4 %. ירידה של 5 % בהספק השיאי נצפתה לאחר שעתיים רצופות של הפעלה.

לייזר ה- CO_2 מסוג פס הסרט שתוכנן נבנה ונחקר במסגרת עבודה זאת מציג פתרונות לשתי מגבלות עיקריות בעירור מיקרוגלים של התקנים מסוג זה (אי היציבויות הטרמיות, וכן האחידות האורכית של התפרקות המיקרוגל). בעזרת מודל אנליטי מצאנו את העובי המינימלי של פס דיאלקטרי המוכנס לאזור ההתפרקות כדי לייצבה מבחינה טרמית. עקב כך, גדל פינוי החום מאזור ההתפרקות, ונצילות הלייזר משתפרת בהתאם. צימוד המיקרוגל המפולג בין מגנטרון לראש לייזר מסוג פס סרט בחתך קבוע המוצג במחקר זה, אפשר את השגתה של התפרקות מיקרוגל אחידה אורכית. תכונה זאת של ההתפרקות לא סתרה את בחירתו של תחום עבודה מיטבי למגנטרון, וכך התאפשרה הפקת הספקי מיקרוגל ממוצעים ושיאיים גבוהים. החתך הקבוע של ראש הלייזר אפשר שימוש בצינור פיירקס מלבני סטנדרטי כמיכל הגז.

התכנון והמימוש של ההתקן הקומפקטי והרב-תכליתי המוצג בעבודה זאת, מבחינת תיאום הספק המיקרוגל וסילוק החום, מאפשרים את בנייתו של התקן בעל נצילות גבוהה ביותר. התקן זה משלב מאפיינים כגון הספק ממוצע גבוה, הספק שיאי גבוה וכן יחס גבוה בין ההספק השיאי לממוצע. תוצאות ראשוניות מצביעות על פעולה יעילה של לייזר זה כמכשיר חתום, המשמר את תכונות לייזר פס-הסרט שפותח במחקר זה. נתונים אלו עשויים להימצא עדיפים בהשוואה ללייזרים אחרים הפועלים בתחום פרמטרים דומה. לייזר ה- CO_2 מסוג פס הסרט שפותח בעבודה זאת עשוי להיות מועדף ליישומים שונים, לאור הדרישה הגדלה לו בתחומים רבים.

עבודה זאת מוקדשת להורי

שרה ונתן שהדי

תוכן עניינים

5	תקציר
9	הבעת תודה
10	רשימת סימנים
14	1. מבוא
15	1.1. סיווג לייזרים
18	1.2. לייזר ה- CO_2
20	1.2.1. שיטות שאיבה ללייזר ה- CO_2
22	1.2.2. תהליכים קינטיים של מעברי אנרגיה בלייזר CO_2
26	1.2.3. לייזר CO_2 מסוג פס סרט
27	1.2.3.1. שיקולי מעבר חום
31	2. ההתפרקות החשמלית בלייזר פס סרט
31	2.1. תהליכי התפרקות בגז
34	2.2. התפרקות מיקרוגל ו-RF
36	2.2.1. אופני התפרקות יציבה בלייזר פס-סרט מעוררי RF:
36	2.2.1.1. התפרקות מסוג α
39	2.2.1.2. התפרקות מסוג γ
41	2.2.2. השוואת התפרקות RF ומיקרוגלים
44	3. שיקולי אי-יציבות טרמית ללייזרים פולסיים מסוג פס-סרט המעוררים ע"י מיקרוגלים
44	3.1. אפיון אי יציבות ההתפרקות
46	3.2. אי-יציבויות טרמיות
48	3.2.1. מודל ההתפרקות
53	3.2.2. התפתחות אי היציבות
54	3.2.2.1. עובי חריץ אפקטיבי למעבר חום בנוכחות פס דיאלקטרי
57	3.2.3. מהלך התפתחות אי-יציבויות טרמיות
60	3.2.4. התפתחות אי-יציבויות טרמיות בנוכחות שכבת ייצוב דיאלקטרית
65	3.2.5. אופטימיזציה טרמית להתפרקות מיקרוגלים
67	4. לייזרים מעוררי מיקרוגל
68	4.1. לייזר CO_2 צילינדרי מסוג לוחות מקבילים (סכמה #1)
69	4.1.1. מערך הניסוי
72	4.1.2. שיקולי תכנון מערך המיקרוגל
75	4.1.3. תוצאות ניסיוניות (סכמה #1)
78	4.1.4. דיון
79	4.2. לייזר CO_2 מסוג פס סרט (סכמה #2)
80	4.2.1. מערך הניסוי

83	4.2.2. מערך המיקרוגל ושיקולי תכנונו
85	4.2.3. מערך המדידות הניסיוניות
86	4.2.4. תוצאות ניסיוניות (סכמה #2)
86	4.2.4.1. האחידות האורכית של ההתפרקות
88	4.2.4.2. לייזר בעל עובי התפרקות של 2.0 מ"מ
99	4.2.4.3. לייזר בעל עובי התפרקות של 1.5 מ"מ
109	4.2.4.4. מדידות פולס המוצא של הלייזר
112	4.2.4.5. מדידות הגבר אות-קטן
114	4.2.4.6. אופטימיזציה לחלון המוצא
116	4.2.4.7. מדידות איכות הקרן
117	4.2.5. לייזר CO ₂ חתום מסוג פס סרט
118	4.2.5.1. מדידות ניסיוניות
119	5. אנליזה
120	5.1. הערכה זמנית ומקומית של בניית האמפליטודה
129	5.2. ניתוח טרמי ללייזר פס הסרט
138	5.3. נצילות לייזר פס הסרט
142	6. סיכום
	נספחים
145	A צימוד המגנטרון לראש הלייזר
148	B מיתוג המתח הגבוה
151	C שפופרות פיירקס מלבניות בלייזר גזי
156	מקורות